A Thesis for the Degree of Ph.D. in Science

Strong-coupling Properties of an Ultracold Bose-Fermi Mixture with a Hetero-nuclear Feshbach Resonance

July 2017

Graduate School of Science and Technology
Keio University

Digvijay Kharga

Abstract

In this thesis, I theoretically investigate normal-state properties of a gas mixture of single-component Bose and Fermi atoms, with a tunable inter-species pairing interaction associated with a hetero-nuclear Feshbach resonance. Including Bose-Fermi hetero-pairing fluctuations associated with the inter-species interaction, I clarify single-particle properties of the system above the Bose-Einstein condensation temperature $T_{\rm BEC}$, from the weak-coupling regime to the strong-coupling regime. I also examine strong-coupling effects on thermodynamic quantities.

After an overview of cold atom physics, I present my formulation. I point out that the ordinary non-self-consistent T-matrix approximation (TMA), which has extensively been used for the study of strongly interacting ultracold Fermi gases, has room for improvement, when applied to a Bose-Fermi mixture. This is because TMA uses the bare Bose Green's function that does not satisfy the required gapless Bose excitations at the $T_{\rm BEC}$, in evaluating self-energy corrections. To overcome this, I improve TMA so that the gapless condition can be satisfied.

Using this improved T-matrix approximation (iTMA), I study single-particle excitations near $T_{\rm BEC}$. Hetero-pairing fluctuations are shown to couple Fermi atomic excitations with Bose atomic and Fermi molecular excitations. Although a similar coupling phenomenon is known in the unitary regime of an ultracold Fermi gas, while it causes the pseudo-gapped density of states in the latter Fermi system, such a phenomenon is found to be absent in a Bose-Fermi mixture even at the unitarity. A shallow pseudo-gapped density of state is only obtained in the strong-coupling regime.

I also examine strong-coupling effects on thermodynamic properties of a unitary Bose-Fermi mixture. To minimize ambiguity coming from approximate treatment of hetero-pairing fluctuations, I employ a combined iTMA with exact thermodynamic relations, where complicated iTMA calculations are only done to calculate Fermi and Bose chemical potential. Various thermodynamic quantities are then evaluated from the calculated chemical potential by using exact thermodynamic identities. I find that the specific heat at constant volume is a useful quantity for the study of strong-coupling properties of the system, because it is sensitive to hetero-pairing fluctuations, to exhibit anomalous non-monotonic temperature dependence.

Finally I will summarize this thesis.

Keywords : Bose-Einstein Condensation (BEC), ultracold Bose-Fermi mixture, hetero-nuclear Feshbach resonance, pseudogap, universal thermodynamics.

Contents

Chapter 1

Introduction

In this Chapter we introduce a Bose-Fermi mixture with a hetero-nuclear Feshbach resonance. After a brief review of this system, we explain a tunable Bose-Fermi inter-species attractive interaction associated with a hetero-nuclear Feshbach resonance. In cold Fermi gas physics, a Feshbach-induced tunable pairing interaction between Fermi atoms has enabled us to study system properties, from the weak-coupling regime to the strong-coupling limit in a systematic manner. In particular the so-called BCS (Bardeen-Cooper-Schrieffer)-BEC (Bose-Einstein condensation) crossover phenomenon has attracted much attention both experimentally and theoretically, where the character of the Fermi superfluid continuously changes from the weak-coupling BCS type discussed in metallic superconductivity to the BEC of tightly bound molecules, as one increases the strength of the Fermi-Fermi attractive interaction by adjusting the threshold energy of a Feshbach resonance. We briefly review this BCS-BEC crossover, and then discuss what is expected when an inter-species pairing interaction is tuned by a hetero-nuclear Feshbach resonance in a Bose-Fermi mixture. We also explain the universal thermodynamics, which is valid for the system with diverging s-wave scattering length. At the end of this Chapter, we present the purpose of this doctor thesis.

1.1 Bose-Fermi Mixture

In cold atom physics, a gas mixture of single-component bosons and single-component fermions (Bose-Fermi mixture) [1–15] has attracted much attention as a counterpart of two-component Fermi gases [16–22]. These quantum gases are experimentally realized by trapping atoms (Fig. 1.1), such as ^{40}K, ^{6}Li, ^{7}Li and ^{87}Rb, by magnetic and optical method, to cool down to ultracold low temperature region ($T \lesssim O(\mu\mathrm{K})$) where quantum effects are important. While they have no impurity as well as background lattice, we can experimentally tune their various physical parameters, such as temperature, number of atoms in the trap potential, and the strength of interaction. In particular a tunable pairing interaction, associated with the Feshbach resonance [23] has extensively been used in two-component ^{6}Li Fermi gases and ^{40}K Fermi gases for the study of Fermi superfluid properties, from the weak-coupling regime to the strong-coupling limit in a unified manner. This so-called BCS (Bardeen-Cooper-Schrieffer)-BEC (Bose-Einstein condensation) crossover physics is

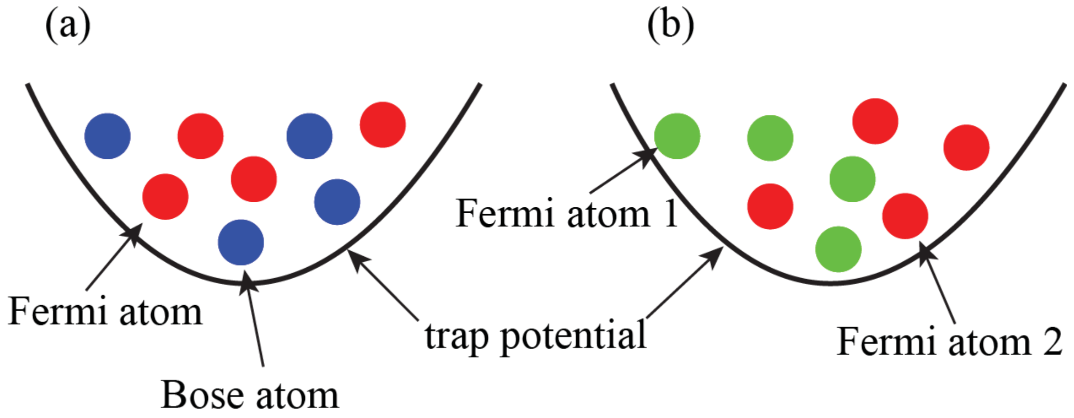

Figure 1.1: Schematic picture of (a) Bose-Fermi mixture, and (b) two-component Fermi gas, in a harmonic trap potential produced optically and/or magnetically. For the study of BCS-BEC crossover the same kind of (^{40}K or ^{6}Li) Fermi atoms in two different atomic hyperfine states are trapped.

one of the central topics in cold Fermi gas physics [16–19]. The intermediate coupling regime, which is also referred to as BCS-BEC crossover region, has particularly attracted much attention because strong-pairing fluctuations dominate over the system properties. Since such tuning of a pairing interaction is also possible in a Bose-Fermi mixture by using a hetero-nuclear Feshbach resonance [7–10, 12–15, 23, 24], comparative study of Fermi-Fermi and Bose-Fermi gases would be useful for studying how the particle statistics (boson and fermion) affects strong-coupling properties of quantum many-body systems.

Although a Bose-Fermi mixture has been studied from the viewpoint of physical properties, this hetero-system has also been used to cool down a Fermi gas. To explain this, we first briefly review the standard cooling method in cold atom physics. As schematically shown in Fig. 1.2, we prepare beam of atoms by vaporizing metal atoms in an oven. This beam is decelerated in a Zeeman slower, when atoms absorb counter-propagating laser photons (radiation pressure). Then atoms are captured in a magneto-optical trap (MOT), where atoms experience laser cooling as in the Zeeman slower. However this cooling alone is not sufficient to achieve the quantum degenerate regime, so that the so-called evaporative cooling is further imposed after the laser cooling [25–27], where atoms with high kinetic energy is selectively removed from the trap. Indeed this hybrid cooling method (laser and evaporative cooling) succeeded in realizing the Bose-Einstein condensation (BEC) of dilute Bose gases [28–30].

However, in contrast to the boson case, the naive evaporatively cooling does not effectively work well for the (single-component) fermion case, because the s-wave interaction, which is usually determined in a dilute gas, is forbidden between identical fermions due to Pauli's exclusion principle, which is also referred as the Pauli blocking effect. In this case, the Pauli blocking suppresses the re-thermalization of the system by collision with the other atoms, during evaporative cooling which remarkably decreases cooling efficiency.

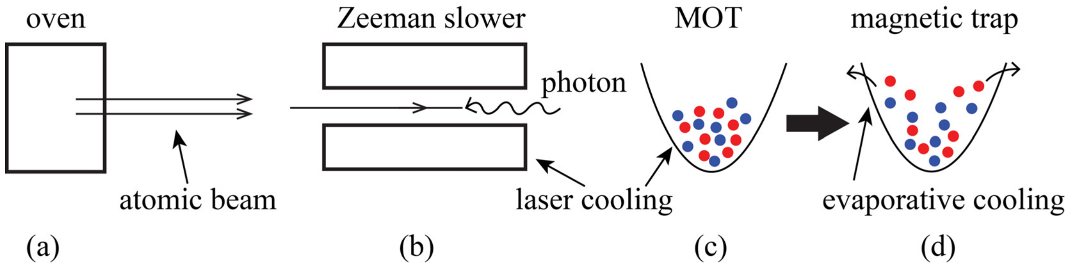

Figure 1.2: Schematic picture of standard cooling process used in cold atom physics. (a) Metal is vaporized by an oven to produce atomic beam. (b) The beam passes through a Zeeman slower, where atoms are decelerated by absorbing counter-propagating laser photons. (Note that atoms again emit photons in random directions, so that this emission process does not accelerate atomic motion on an average.) (c) The atomic gas is then trapped by a magneto-optical trap (MOT), where atoms are further cooled down by laser cooling (The basic cooling mechanism is the same as that in a Zeeman slower.) (d) Evaporative cooling, where atoms with high energy are selectively removed from the trap, to lower the temperature.

Thus, to effectively cool in Fermi gas keeping rapid re-thermalization, bosons are added to the system, so as to produce collisions between fermions and bosons. (Note that the Pauli blocking effect does not work between different species.) This cooling method is sometimes referred to as the sympathetic cooling in literature [25, 26].

Figure 1.3 shows the observed density profiles of a ^{7}Li (Bose)-^{6}Li (Fermi) mixture in a harmonic trap. Using sympathetic cooling technique this experiment [1] had succeeded in achieving the Fermi degeneracy for the first time. At $T = 810$ nK ($T/T_{\rm F} = 1.0$), both the Bose (^{7}Li) and Fermi (^{6}Li) gas clouds spread out, indicating that the Pauli blocking effect does not work. However, as one enters the Fermi degenerate regime ($T < T_{\rm F}$), while the Bose gas cloud shrinks reflecting that the system approaches Bose-Einstein condensation temperature ($T_{\rm BEC} = 240$ nK), the Fermi gas cloud still spreads out even at $T/T_{\rm F} = 0.25$ because the Fermi statistics effectively works like a pressure. Since this success, sympathetic cooling has also contributed to further realization of simultaneous quantum degeneracy in a mixture of bosons and fermions, as well as quantum degeneracy of atomic gases with unfavorable collisional properties [2–5].

The above mentioned sympathetic cooling is an example of the application of an interaction between bosons and fermions to research for a degenerate quantum Fermi gas. On the other hand, such an inter-species interaction has also been studied from the viewpoint of the stability of a Bose-Fermi mixture both experimentally [6] and theoretically [31–34]. Figure 1.4 shows the density profiles of fermionic ^{40}K and bosonic ^{87}Rb in quantum degenerate regime. Initially the BEC of ^{87}Rb Bose atoms coexists with a large amount of ^{40}K Fermi atoms (left panel); however as the BEC grows the Fermi density profile remarkably decreases, implying the collapse of this component. This experimental result indicates the induction of an effective interaction between the Fermi atoms via Bose-Fermi interaction [35, 36], leading to drastic effects on the fermion component. The authors of this paper [6] also report

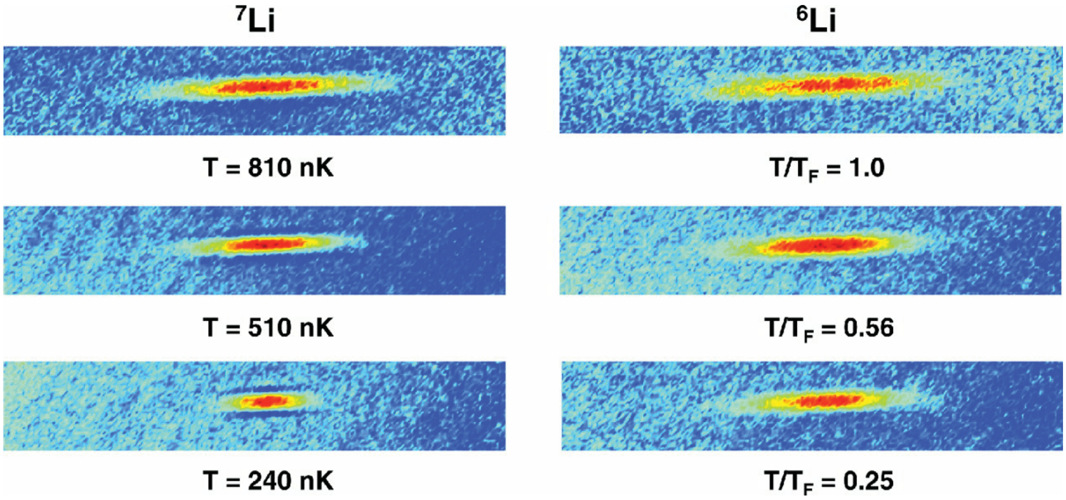

Figure 1.3: Sympathetic cooling experiment on a mixture of bosons (^{7}Li) and fermions (^{6}Li) [1]. Two-dimensional false color images of bosonic ^{7}Li and fermionic ^{6}Li clouds. The figures show spatial variation of atomic density, where the highest density region is shown by red color. Both the clouds are simultaneously cooled from $T/T_{\rm F}$ = 1.0 (top) down to $T/T_{\rm F}$ = 0.25 (down). The Bose gas component (^{7}Li) shrinks at T = 240 nK because the gas is close to Bose-Einstein condensation temperature. On the other hand, the Fermi gas component (^{6}Li) spreads out as compared to the Bose condensed ^{7}Li gas, because of the Pauli blocking associated with Fermi-Dirac statistics. The number $N_{^6{\rm Li}}$ of ^{6}Li atoms and the number $N_{^7{\rm Li}}$ of ^{7} Li atoms in the trap are $(N_{^6{\rm Li}}, N_{^7{\rm Li}}) = (8.7\times10^4, 2.4\times10^5)$ (T = 810 nK), $(1.3\times10^5, 1.7\times10^5)$ (T = 510 nK), and $(1.4\times10^5, 2.2\times10^4)$ (T = 240 nK). [From A. G. Truscott, K. E. Strecker, W. I. McAlexander, G.B. Partridge, and R. G. Hulet, “Observation of Fermi Pressure in a Gas of Trapped Atoms,” Science **291**, 2570, (2001). Reprinted with permission from AAAS. http://dx.doi.org/10.1126/science.1059318.]

that such a collapse does not occur when the number $N_{^{40}{\rm K}}$ of ^{40}K Bose atoms is smaller than 1.8×10^4 in the harmonic potential.

We briefly note that effects of inter-species interaction have also been studied from various viewpoints, such as chemical equilibrium among Bose atoms, Fermi atoms and quasi-molecular fermions [37,38] discussing the phase-diagram of a Bose-Fermi mixture, the formation of hetero-nuclear Feshbach molecules [11], and simultaneous Bose and Fermi superfluid in a gas mixture of one-component bosons and two-component fermions [39–41]. Also, strong-coupling *ordinary* T-matrix approximation (TMA) has been applied to a Bose-Fermi mixture [42–46] to deal with hetero-pairing fluctuations, as well as single-particle spectra in the strong-coupling regime at T=0 [46].

Although this thesis deals with a Bose-Fermi mixture consisting of one-component bosons and one-component fermions, we briefly note that, recently, a double condensate has been observed, in another kind of Bose-Fermi mixture, that is, one-component ^{7}Li bosons and two-component ^{6}Li fermions as shown in Fig. 1.5. In this experiment [39], Bose and Fermi superfluidity simultaneously occur in the same

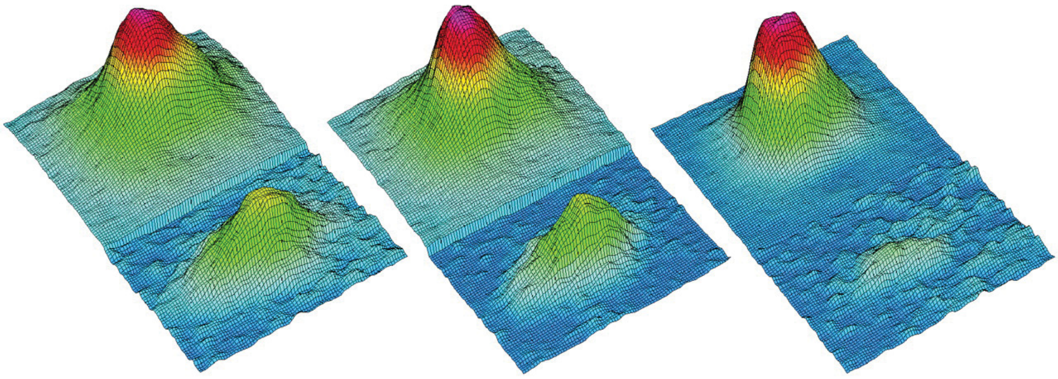

Figure 1.4: Density profile of a Bose (^{87}Rb: back figures)- Fermi (^{40}K: front figures) mixture, showing collapse of Fermi gas [6]. The quantum degeneracy of the mixture is reached by evaporative cooling process. Initially (left) the BEC coexists with a large Fermi gas cloud. As the BEC grows at lower temperature, the Fermi gas is moderately depleted (middle) due to inelastic collisions. Although the BEC continues to exist (right), Fermi gas is almost collapsed. In this experiment, he number of ^{40}K and ^{87}Rb are $\mathcal{O}(10^4 - 10^5)$. The inter-species s-wave scattering length ($a_{\rm BF}$) is estimated as $a_{\rm BF} = -21.7$ nm. Although the magnitude of the temperature is not mentioned in this paper, it states that ^{87}Rb gas is in the BEC phase. [From G. Modugno, G. Roati, F. Roboli, F. Ferlaino, R. J. Brecha, and M. Inguscio, "Collapse of a Degenerate Fermi Gas," Science **297**, 2240 (2002). Reprinted with permission from AAAS. http://dx.doi.org/10.1126/science.1077386.]

trap potential, that are, respectively, confirmed with the shrinkage of bosonic density profile shown in Fig. 1.5, and the plateau structure of the density difference of the two fermion components shown in the inset of this figure.

1.2 Hetero-nuclear Feshbach Resonance

An advantage of cold atom physics is that one can experimentally tune the strength of interaction between atoms by using a Feshbach resonance. In particular, this novel technique has extensively been used in a two-component Fermi gas consisting of Fermi atoms, in different atomic hyperfine states (that are conveniently described by pseudospin $\sigma =\uparrow,\downarrow$), for the study of the so-called BCS-BEC crossover phenomenon (which we will explain in Sec. 2.3). In this thesis, we deal with a Bose-Fermi mixture with a tunable interaction between Bose and Fermi atom, keeping the existence of the technique in mind.

Feshbach resonance is a kind of resonance scattering, where two atoms form a quasi-molecule in the intermediate state and it dissociates into two atoms again. In the case of two-component Fermi gas, (Fig. 1.6(a)), the so-called Feshbach (quasi) molecule is bosonic in character because it is composed of two Fermi atoms. On the other hand, in case of a Bose-Fermi mixture (Fig. 1.6(b)) which we consider in the thesis, a fermionic molecule appears in the intermediate state. Conventionally,

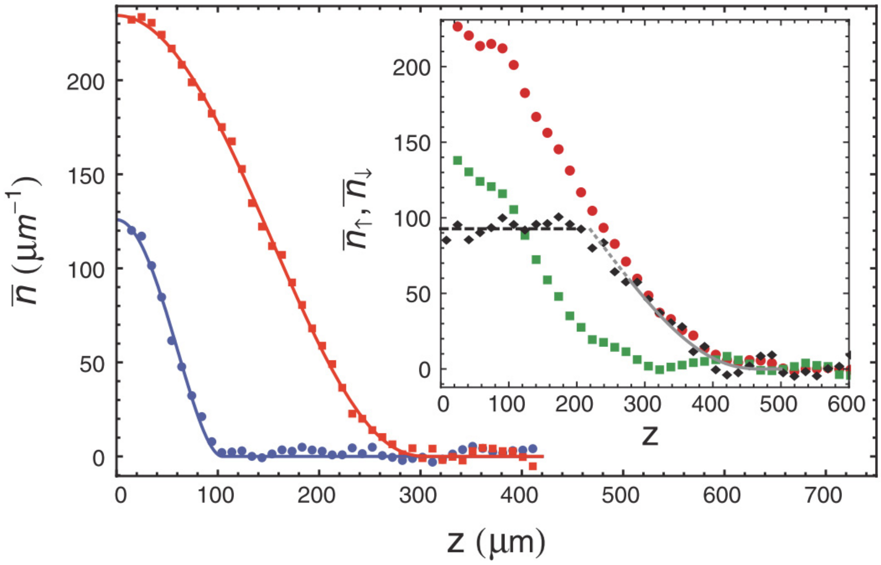

Figure 1.5: Density profile of fermionic ^{6}Li (two-component Fermi gas) and bosonic ^{7}Li component at 130 nK [39]. The bosonic component shows a sharp peak near the trap center indicating the Bose-Einstein condensation phase. The inset shows the ^{6}Li fermion density profile in the presence of population imbalance. The density difference (solid diamonds) between the two exhibits a plateau near the trap center indicates superfluid pairing there, while a fully spin-polarized Fermi gas in the outer regime. [From I. Ferrier-Barbut, M. Delehaye, S. Laurent, A. T. Grier, M. Pierce, B. S. Rem, F. Chevy, and S. Salomon, “A mixture of Bose and Fermi superfluids,” Science **345**, 1035 (2014). Reprinted with permission from AAAS. http://dx.doi.org/10.1126/science.1255380.]

the initial (dissociated) states and the intermediate (paired) atomic states are called open and closed channel, respectively.

In a Feshbach resonance, a crucial key is that the hyperfine interaction between the electron and the nuclear spin also works in the scattering process, so that atomic hyperfine states of atoms in the closed channel become different from those in the open channel. This leads to difference of Zeeman energy between the open and closed channel in the presence of an external magnetic field B, so that the resonance level 2ν shown in Fig. 1.6(c) also depends on B.

Keeping this in mind, evaluating the scattering process shown in Fig. 1.6(a) and (b) within the second order perturbation, we obtain a Feshbach induced effective interaction $U_{\rm eff}$ between the atoms in the open channel as

$$U_{\rm eff} = -g^2 \frac{1}{2\nu}, \tag{1.1}$$

where g is a Feshbach coupling constant, describing transfer matrix element between atoms in the open channel and a Feshbach molecule. In obtaining Eq. (1.1) we have assumed the low energy limit of initial atomic states. Equation (1.1) is valid for both the Fermi-Fermi and Bose-Fermi cases. Near a Feshbach resonance field B_0,

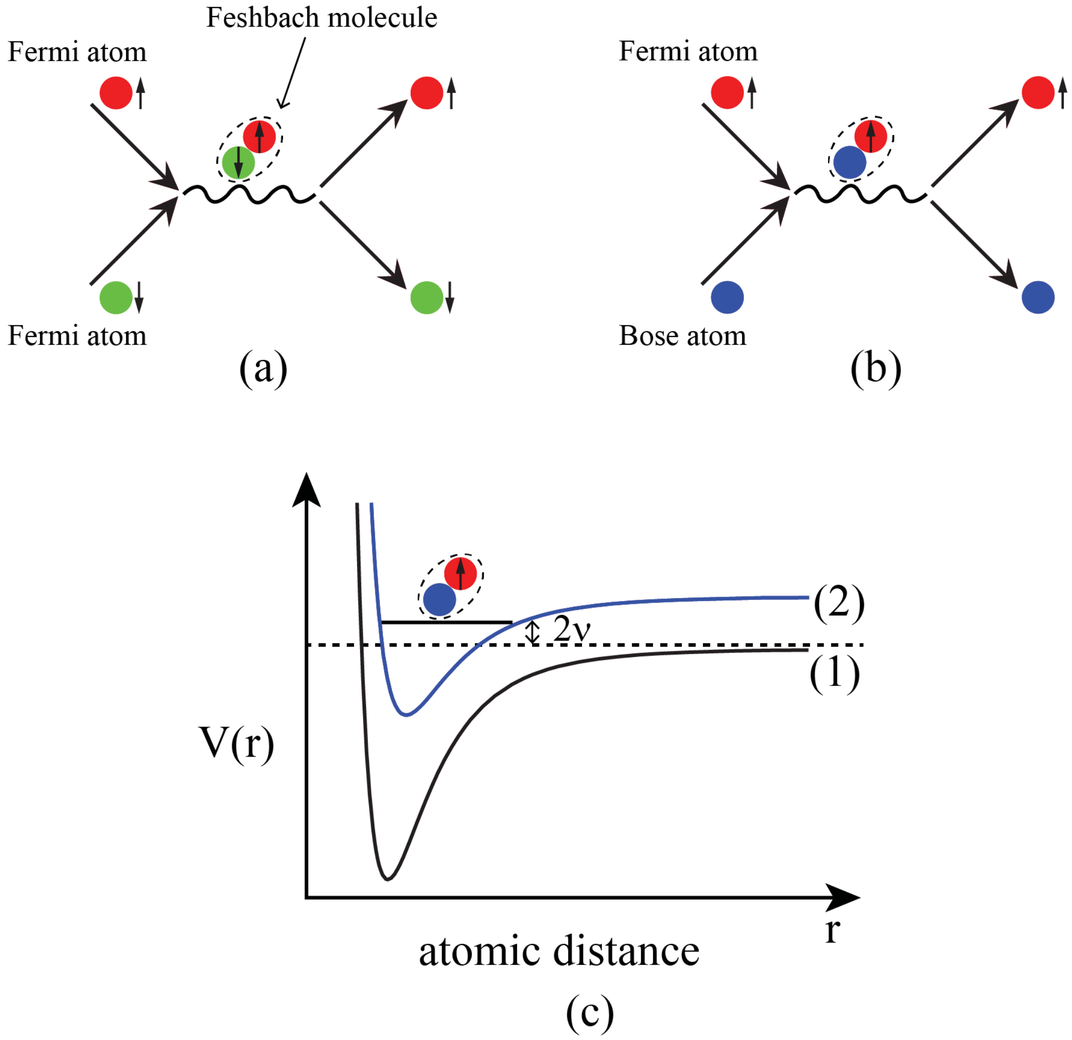

Figure 1.6: Schematic picture of Feshbach resonance (a) Fermi-Fermi case. (b) Bose-Fermi case. (c) Interaction potential $V(r)$ with respect to the magnitude r of relative co-ordinate of two atoms. In this panel, (1) and (2) shows $V(r)$ that atoms in the open-channel and closed-channel feel, respectively. 2ν shows the energy of a Feshbach-resonance state, which is referred to as the threshold energy of a Feshbach resonance.

one may write

$$2\nu = \alpha(B - B_0). \tag{1.2}$$

We also include a weak background residual interaction $U_{\rm bg}$, then the effective interaction near a Feshbach resonance field is expressed as

$$U_{\rm eff} = U_{\rm bg} - g^2 \frac{1}{\alpha(B - B_0)}. \tag{1.3}$$

The tunability of this Feshbach-induced effective interaction has been confirmed by measuring the scattering length a_s, as well as the scattering cross-section $\sigma = 4\pi a_s^2$ [23, 47]. Here, the scattering length corresponding to the effective interaction in Eq.

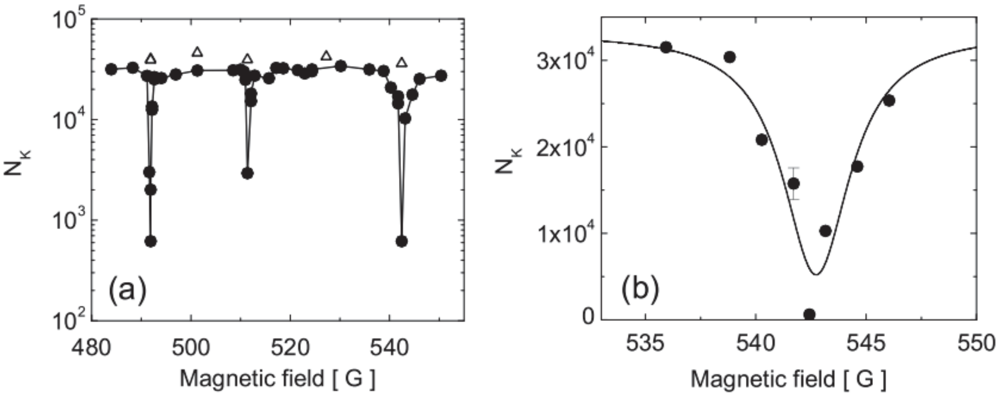

Figure 1.7: Observation of three hetero-nuclear Feshbach Resonances in a Bose (^{87}Rb)- Fermi (^{40}K) mixture [8]. (a) The number $N_{\rm K}$ of ^{40}K atoms in a trap after holding the mixture in a dipole trap for 1.08 s (filled circles). The peaks are due to inelastic losses by an interaction with ^{87}Rb. The open triangles shows the results when ^{87}Rb is absent. (b) The same as panel (a) where the result is magnified around the magnetic field $\sim$ 545 G. [Reprinted figure with the permission from S. Inouye, J. Goldwin, M. L. Olsen, C. Ticknor, J. L. Bohn, and D. S. Jin, "Observation of Heteronuclear Feshbach Resonances in a Mixture of Bosons and Fermions," Phys. Rev. Lett. **93**, 183201 (2004). Copyright (2004) by the American Physical Society. https://doi.org/10.1103/PhysRevLett.93.183201.]

(1.3) has the form

$$a_s(B) = a_s^{\rm bg}\left(1 - \frac{\Delta}{B - B_0}\right), \tag{1.4}$$

where Δ gives the width of the resonance and $a_s^{\rm bg}$ is a background scattering length. A Feshbach resonance with large (small) Δ is frequently called a broad (narrow) Feshbach resonance, although there is no clear boundary between the two cases.

We briefly note that the quantum statistics of atom is not important in a Feshbach resonance. (A Feshbach resonance occurs also between two Bose atoms.) Usually in the case of fermion-fermion, as well as boson-boson, we simply use the term "Feshbach resonance." In the case of boson-fermion, we frequently use the term "hetero-nuclear Feshbach resonance," which we also use in this thesis.

Figure 1.7 shows the observation of three heteronuclear Feshbach resonances in a ^{87}Rb-^{40}K Bose-Fermi mixture [8]. Near a Feshbach resonance ($2\nu \simeq 0$), the effective interaction in Eq. (1.3) becomes very strong, leading to the particle loss from the trap. Thus, magnetic fields where sharp decrease of the number $N_{\rm K}$ of ^{40}K atoms that occur in this figure are Feshbach resonance magnetic fields B_0.

Figure 1.8 shows rf-tunneling current spectrum in a ^{40}K-^{87}Rb Bose-Fermi mixture loaded in a 3D optical lattice [11]. The rf-spectroscopy can observe single-particle excitations in a cold atomic gas. In this experiment, while the lower peak comes from the ordinary single-particle excitations of unpaired ^{40}K atoms, the upper peak corresponds to ^{40}K excitations being accompanied by dissociation of ^{40}K-^{87}Rb molecules

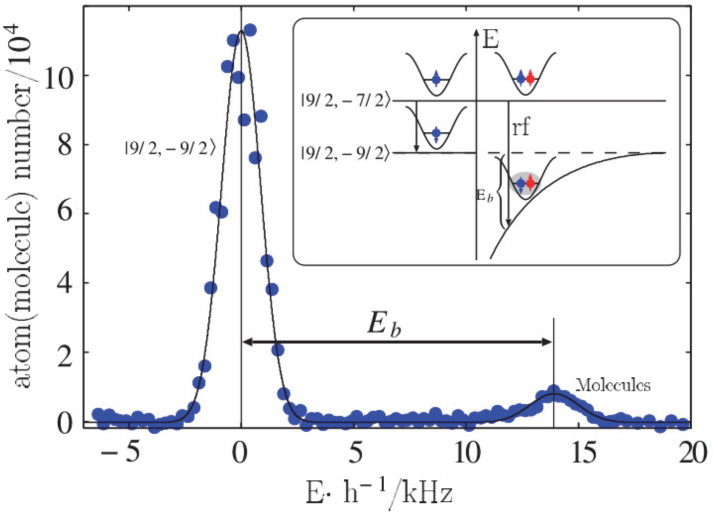

Figure 1.8: Observed rf-spectroscopy in a ^{40}K-^{87}Rb mixture loaded on a 3D optical lattice [11]. The inset schematically shows the transition process used in this experiment. The double peak structure indicates the presence of a ^{40}K-^{87}Rb bound molecule, with a binding energy $E_{\rm b}$. [Reprinted figure with the permission from C. Ospelkaus, S. Ospelkaus, L. Humbert, P. Ernst, K. Sengstock, and K. Bongs, "Ultracold Heteronuclear Molecules in a 3D Optical Lattice," Phys. Rev. Lett. **97**, 120402 (2006). Copyright (2006) by the American Physical Society. https://doi.org/10.1103/PhysRevLett.97.120402.]

that are turned by strong attractive interaction associated with a hetero-nuclear Feshbach resonance.

1.3 BCS-BEC Crossover Physics and Expected Analogous Phenomenon in a Bose-Fermi Mixture with a Hetero-nuclear Feshbach Resonance

One of the most important achievements by using Feshbach resonance is the realization of the BCS-BEC crossover phenomenon in a two-component Fermi gas. In this section, we overview of this many-body quantum phenomenon, to see what sort of similar phenomenon are expected when one tunes the strength of an inter-species pairing interaction associated with a hetero-nuclear Feshbach resonance in a Bose-Fermi mixture which we deal within the thesis.

In the BCS-BEC crossover, the character of a Fermi superfluid continuously changes from the weak-coupling BCS-type discussed in metallic superconductivity, to the Bose-Einstein condensation (BEC) of tightly bound molecular bosons that have clearly been formed above the superfluid transition temperature $T_{\rm c}$, with increasing the strength of the pairing interaction [48–56]. In the weak-coupling regime,

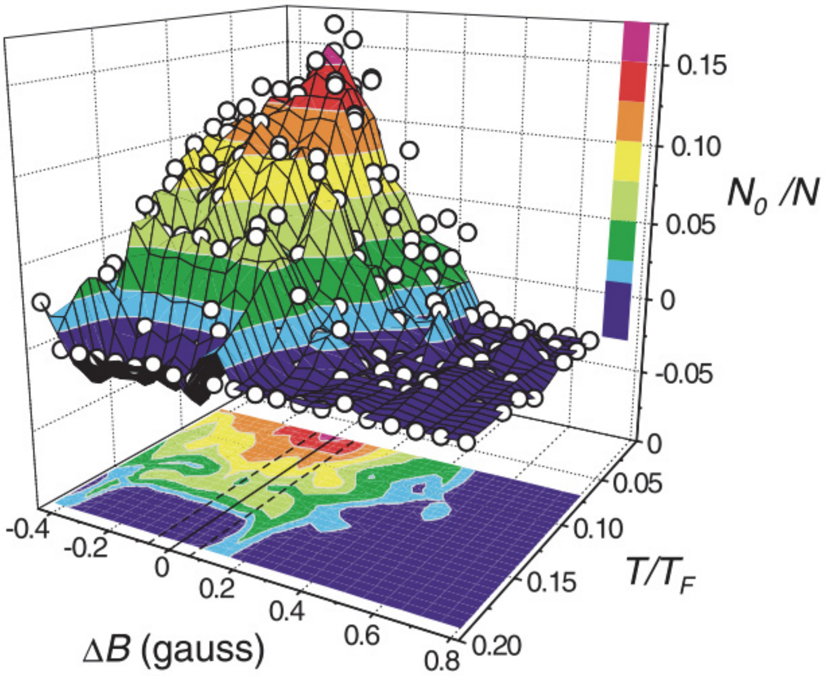

Figure 1.9: Condensate fraction N_0 in a two-component ^{40}K Fermi gas [16]. $T_{\rm F} = 0.35$ μK is the Fermi temperature. $\Delta B = B - B_0$ is the external magnetic field, measured from a Feshbach resonance $B_0 = 202$ G. In this experiment, the system is regarded as a Fermi superfluid, when $N_0 \neq 0$. N is the number of atoms in the trap. [Reprinted figure with the permission from C. A. Regal, M. Greiner, and D. S. Jin, "Observation of Resonance Condensation of Fermionic Atom Pairs," Phys. Rev. Lett. **92**, 040403 (2004). Copyright (2004) by the American Physical Society. https://doi.org/10.1103/PhysRevLett.92.040403.]

thus $T_{\rm c}$ monotonically increases as one approaches the intermediate coupling regime (which is referred to as crossover regime or unitary regime in the literature), reflecting the increase of the binding energy of Cooper pairs [57]. On the other hand, the superfluid phase transition temperature in the strong-coupling BEC regime is dominated by BEC of tightly bound molecular bosons. Deep inside the BEC regime, noting that the number $N_{\rm B}$ of such molecular molecular bosons, equals half the number $N_{\rm F}$ of Fermi atoms, $T_{\rm c}$ in this regime can be evaluated from $T_{\rm c}$ of an ideal gas of $N_{\rm B} = N_{\rm F}/2$ bosons with the molecular mass $M = 2m$ (where m is the Fermi atomic mass) as

$$T_{\rm BEC}^0 = \frac{2\pi\hbar^2}{2mk_{\rm B}} \left[\frac{N/2}{V\zeta(3/2)}\right] = 0.218T_{\rm F}, \tag{1.5}$$

where $\zeta(3/2) \simeq 2.612$ is the zeta function, $\hbar$ and $k_{\rm B}$ are the Planck and Boltzmann's constant, respectively. Equation (1.5) is independent of the interaction strength between Fermi atoms. As a result, when the interaction strength is increased from the weak-coupling BCS side, $T_{\rm c}$ first increases and then, approaches the constant value in Eq. (1.5) in the strong-coupling regime. Although the physical situations in the weak- and strong-coupling regimes are very different from each other, they continuously change from one to the other as one varies the strength of a pairing interaction; thus this phenomenon is termed "crossover".

Figure 1.9 shows the observation of a ^{40}K superfluid Fermi gas in the BCS-BEC crossover region. In this experiment [16], the strength of interaction between ^{40}K Fermi atoms in different atomic hyperfine states are tuned by adjusting the threshold energy of a Feshbach resonance at $B_0 = 202$ G, by tuning an external magnetic field $\Delta B = B - B_0$. Thus $\Delta B > 0$ and $\Delta B < 0$ correspond to, respectively, the weak-coupling BCS-side and strong-coupling BEC-side. The z-axis in Fig. 1.9 shows the number N_0 of Bose condensed Cooper pairs (with zero center of mass momentum), and non-zero N_0 is judged as the superfluid state in this experiment. Thus, the sky-blue area in the $T/T_{\rm F} - \Delta B$ plane is regarded as $T_{\rm c}$. Then, with decreasing the external magnetic field ΔB or increasing the strength of the pairing interaction, $T_{\rm c}$ is found to increase to become constant in the strong-coupling regime. The value of $T_{\rm c}/T_{\rm F} = 0.17$ is close to the predicted "BEC value" in Eq. (1.5). We briefly note that the superfluid phase transition, as well as the BCS-BEC crossover phenomenon has also been realized in a ^{6}Li Fermi gas [17].

Since a crucial key of the BCS-BEC crossover phenomenon is the pair formation by a tunable pairing interaction associated with a Feshbach resonance, a similar many-body quantum phenomenon is also expected in case of a Bose-Fermi mixture, when a Bose-Fermi inter-species attractive interaction is tuned by a hetero-nuclear Feshbach resonance. To see this, we schematically show in Fig. 1.10 that pair formation affects system properties in the Fermi-Fermi case (a), as well as the Bose-Fermi case (b). In this figure, we find that, although the "molecular character" becomes more remarkable in the strong-coupling regime in both the cases, "the superfluid phase transition" is expected to exhibit opposite tendency between the two. That is, the number of bosons that can contribute to the superfluid phase transition gradually increases with increasing the interaction strength, to become a maximum in the strong-coupling regime of the Fermi-Fermi case, the maximum number of bosons (that can contribute to the phase transition) is obtained in the weak-coupling limit in the Bose-Fermi case. Thus, in the latter case the superfluid phase transition is expected to decrease as one approaches the strong-coupling regime, which is in contrast to the former. Indeed Ref. [44] theoretically predicts that the superfluid phase transition temperature vanishes in a Bose-Fermi mixture when the interaction strength exceeds a certain value (which we will also discuss in Chap. 2).

On the other hand, the situation in the intermediate coupling coupling regime looks somehow similar to each other (see the middle pictures of Fig. 1.10(a) and (b)). That is, in both the cases, the system may be viewed as a mixture of two kinds of fermions and one-component bosons. However, while the mixture consists of two kinds of Fermi "atoms" and one-component Bose "molecules" in the Fermi-Fermi case, a Bose-Fermi mixture in the intermediate coupling regime is composed of one-component Fermi "atoms", one-component Fermi "molecules", and one component Bose "atoms". Thus, it is an interesting problem, how this similarity and difference affect the physical properties of a Bose-Fermi mixture in this regime, compared to the properties of a two-component Fermi gas in the BCS-BEC crossover region. In this thesis, we theoretically tackle this problem.

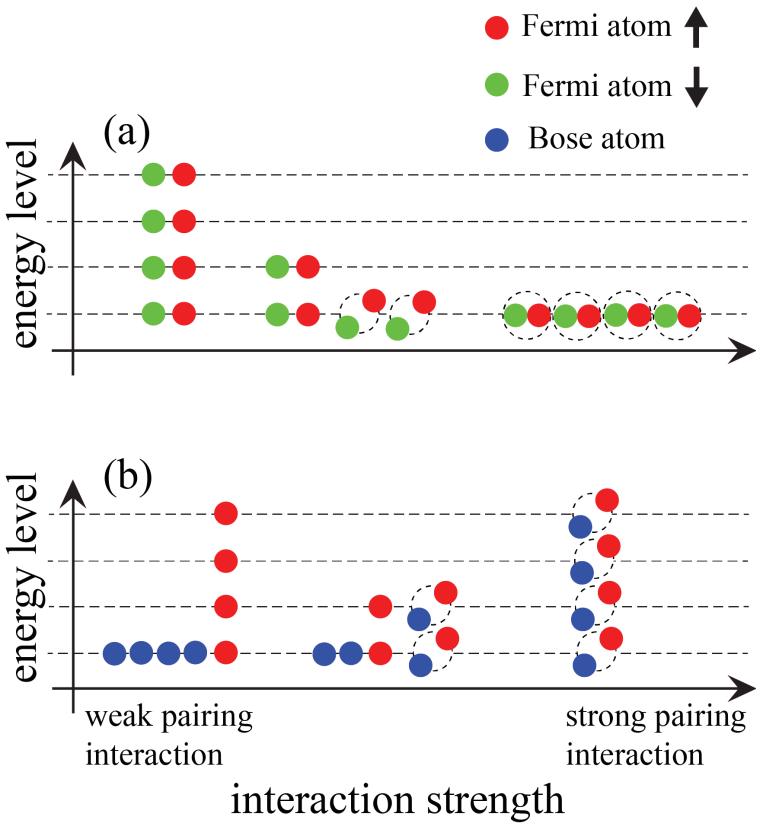

Figure 1.10: Schematic picture of effects of tunable pairing interaction on (a) a two-component Fermi gas, and (b) a Bose-Fermi mixture. While strong-coupling regime is dominated by Cooper-pair bosons in (a), the strong-coupling regime in (b) may be regarded as a gas of tightly bound molecular fermions.

1.4 Pseudogap Phenomenon: A Typical Many-body Phenomenon in the BCS-BEC Crossover Region

In the previous section, we presented Fig. 1.10 to simply grasp the similarity and difference between a two-component Fermi gas and a Bose-Fermi mixture, in the presence of a tunable pairing interaction associated with a (hetero-nuclear) Feshbach resonance. However, this schematic picture is, strictly speaking, only valid for our intuitive understandings, and we need to actually treat the meaning of "molecules" in the intermediate coupling regime (middle pictures in Fig. 1.10(a) and (b)) more carefully. Actually molecules in this regime are not stable, but fluctuating, that is, pair formation and its dissociation repeatedly occur there. This so-called pairing fluctuations is known to dominate over the normal-state properties near $T_{\rm c}$ in the BCS-BEC crossover regime of an ultracold Fermi gas, and has attracted much attention both theoretically [58–66], and experimentally [67–69].

The pseudogap is one of the characteristic phenomenon predicted in the BCS-BEC crossover region of an ultracold Fermi gas. This many-body phenomenon is

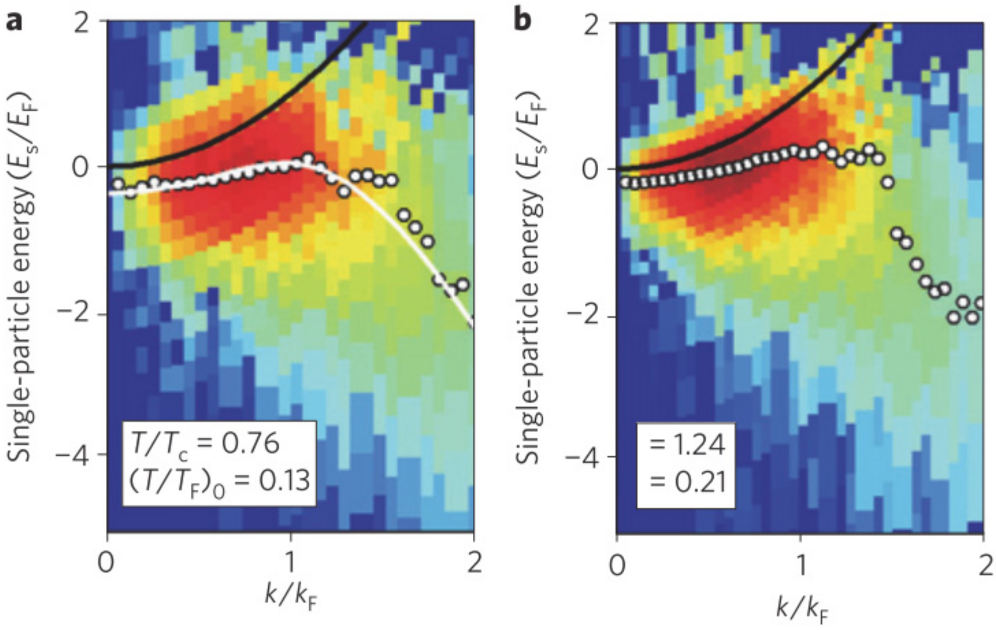

Figure 1.11: Intensity of photoemission spectra in a two-component Fermi gas when $(k_{\rm F}a_s)^{-1} = 0.15$ (BCS-BEC crossover regime) [68]. Panel (a) shows the result in the superfluid phase, below superfluid transition temperature $T_{\rm c}$, where a free particle dispersion (black solid line), as well as a characteristic back-bending curve (white solid line) are seen. Panel (b) shows the result in the normal state, where the back-bending curve still remains in spite of the vanishing superfluid order parameter. [Reprinted by permission from Macmillan Publishers Ltd: Nature Physics, J. P. Gaebler, J. T. Stewart, T. E. Drake, D. S. Jin, A. Perali, P. Pieri, and G. C. Strinati, "Observation of pseudogap behavior in a strongly interacting Fermi gas," **6**, 569 (2010), copyright (2010). https://doi.org/10.1038/nphys1709.]

characterized by the appearance of a dip (pseudogap) structure in the single-particle density of states around the Fermi surface, even in the normal state above $T_{\rm c}$, in spite of the vanishing superfluid order parameter there. According to the preformed pair scenario, the pseudogap is related to fluctuating (preformed) Cooper pairs that are formed in the normal state near $T_{\rm c}$ by strong pairing interaction [58–65]. The pseudogap has been observed in the underdoped regime of the high-$T_{\rm c}$ cuprates [70–72], however the origin in this case is still unclear because of the complexity of this strongly correlated electron system. In contrast, an ultracold Fermi gas in the BCS-BEC crossover region is dominated by pairing fluctuations, so that this dilute gap would be useful for the assessment of the preformed pair scenario in terms of the pseudogap phenomenon.

In the current stage of cold Fermi gas physics, although it is still difficult to directly observe the density of states, as well as the pseudogap structure in it, a phenomenon which is consistent with the existence of the pseudogap phenomenon has been reported by a photoemission-type experiment on a ^{40}K Fermi gas (Fig.

1.11) [68].

In this spectral experiment, Fermi atoms in one of the two hyperfine states (that are strongly interacting with each other in the crossover region) are excited to the third atomic hyperfine state by radiating photons, from which we obtain information about single-particle excitations in a Fermi gas. In the superfluid state shown in Fig. 1.11(a) the observed spectral peaks (open circles) are well explained by the lower branch of the well-known Bogoliubov single-particle dispersion

$$\omega_- = -\sqrt{(\xi^{\rm F}_{\boldsymbol{p}})^2 + \Delta^2}, \tag{1.6}$$

where $\xi^{\rm F}_{\boldsymbol{p}} = \varepsilon_{\boldsymbol{p}} - \mu_{\rm F} = p^2/(2m) - \mu_{\rm F}$ is the kinetic energy measured from the Fermi chemical potential $\mu_{\rm F}$ and Δ is the ordinary BCS superfluid order parameter. (We briefly note that the upper Bogoliubov branch $\omega_+ = +\sqrt{(\xi^{\rm F}_{\boldsymbol{p}})^2 + \Delta^2}$ is strongly suppressed to be invisible in this experiment.) The spectral peak structure, which is frequently referred to as the back-bending behavior of the spectral peak line in this field, is still seen in the normal state above $T_{\rm c}$ as shown Fig. 1.11(b). This implies that, although the superfluid order parameter no longer exists above $T_{\rm c}$, the single-particle dispersion still has a (pseudo) gapped structure,

$$\omega_\pm = \pm\sqrt{(\xi^{\rm F}_{\boldsymbol{p}})^2 + \Delta^2_{\rm pg}}, \tag{1.7}$$

as predicted in the preformed pair scenario [58–66]. When the single-particle excitations are given by Eq. (1.7), the corresponding single-particle density of states in the normal state has a finite excitation gap

$$\Delta E_{\rm g} = 2\Delta_{\rm pg}, \tag{1.8}$$

around $\omega = 0$, as expected from the standard BCS theory. ($\Delta_{\rm pg}$ is sometimes called the pseudogap parameter [58–60, 62].)

Since the pseudogap in BCS-BEC crossover regime of an ultracold Fermi gas originates from the formation of (fluctuating) preformed Cooper pairs, it is interesting to explore a similar phenomenon caused by hetero-pairing fluctuations in a Bose-Fermi mixture. In addition, while preformed Cooper pairs (or pairing fluctuations) in a two-component Fermi gas are bosonic, hetero-pairing fluctuations in a Bose-Fermi mixture are fermionic, in the sense that they eventually change to molecular fermions in the strong-coupling limit. Thus, it is also an interesting problem how this quantum-statistical difference is reflected in strong-coupling properties of a Bose-Fermi mixture, especially in the intermediate coupling regime.

1.5 Universal Thermodynamics in Unitary Gas

While the high-tunability of various physical parameters, such as the interaction strength, is an advantage of cold atom physics, the difficulty in measuring physical quantities compared with the field of condensed matter physics was a weak part in th early stage of this field. However, great experimental efforts have gradually overcome this difficulty, and various thermodynamic quantities have become

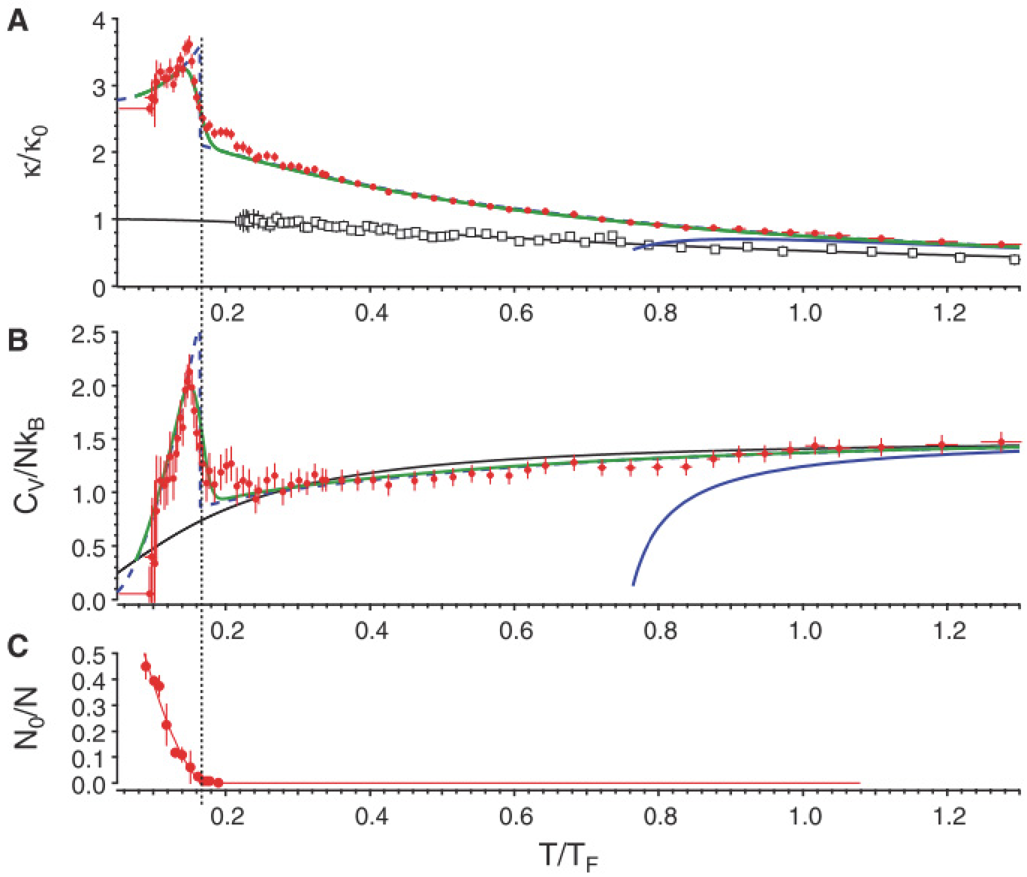

Figure 1.12: Observed thermodynamic quantities in a unitary Fermi gas (filled circles) [78]. A: Compressibility κ. B: Specific heat at constant volume C_V. C: Condensate fraction N_0 (the number of Bose-condensed Cooper pairs). The figure also shows theoretical results for a non-interacting Fermi gas (black solid line), as well as results by the third-order virial expansion (blue solid line). The vertical dotted line shows T_c. [From M. J. H. Ku, A. T. Sommer, L. W. Cheuk, and M. W. Zwierlein, "Revealing the Superfluid Lambda Transition in the Universal Thermodynamics of a Unitary Fermi Gas," Science **335**, 563 (2012). Reprinted with permission from AAAS. http://dx.doi.org/10.1126/science.1214987.]

observable under various conditions [73–80], for example, the BCS-BEC crossover region [75, 80]. Figure 1.12 shows example of such experimental development [78], that is, the observed compressibility, specific heat at constant volume, as well as the condensate fraction (the number of Bose-condensed Cooper pairs), in an ultracold Fermi gas in the unitarity limit (which is just in the middle of the BCS-BEC crossover region).

On the theoretical side, Ho [81] has pointed out that we can greatly simplify thermodynamic analysis on an atomic gas with a contact-type interaction in the unitarity limit. In this special case, because the s-wave scattering length a_s diverges, the interaction parameter formally disappears. The resulting so-called universal thermodynamics has a similar theoretical structure to the thermodynamics in the non-interacting case, in spite of the fact that a unitary gas is actually affected by a strong pairing interaction.

Recently Ref. [82] proposed to combine a strong-coupling theory with the exact thermodynamic identities, in order to calculate ground-state quantities of an ultracold Fermi gas in the BCS-unitary regime. In this approach, complicated strong-coupling calculations are only done to evaluate the Fermi chemical potential $\mu_{\rm F}$. Other thermodynamic quantities, such as the internal energy, compressibility, as well as Tan's contact [83–85], are calculated from the calculated $\mu_{\rm F}$, by using exact thermodynamic relations without carrying out further strong-coupling calculations. The advantage of this approach is that, since the calculated quantities are all related to exact identities, when one of them is experimentally confirmed, the correctness of the others are also immediately verified, even if some of them are still experimentally inaccessible in the current state of cold atom physics. Indeed using this hybrid approach, Ref. [82] succeeds in explaining various experimental results on ultracold Fermi gases in a unified manner.

In Ref. [82], thermodynamics is simplified by considering the zero-temperature limit. Regarding this as mentioned in the above, thermodynamics can also be simplified in the unitarity limit. Thus, extending the approach in Ref. [82] to the unitarity limit at finite temperature is promising for the study of strong-coupling effects on thermodynamic properties of a unitary Bose-Fermi mixture. In this thesis, we employ this idea, to explore characteristic phenomenon associated with hetero-pairing fluctuations in the limiting case.

1.6 Purpose and Outline of this Thesis

In this thesis, we theoretically investigate strong-coupling properties of a Bose-Fermi mixture with a hetero-nuclear Feshbach resonance in the normal state above the Bose-Einstein condensation temperature $T_{\rm BEC}$. In this thesis we deal with the system, being composed of one-component Fermi atoms and one-component Bose atoms, as the simplest Bose-Fermi mixture. With the accessibility of hetero-nuclear Feshbach resonance [7–10, 12–15, 24] as well as the observation of hetero-nuclear Feshbach molecules [11], study of this system has become absolutely necessary because Bose-Fermi mixtures also appears in various systems, such as of nucleons, neutron stars, and Quantum Chromodynamics (QCD). Study of Bose-Fermi mixture in cold atom physics could help in understanding such systems.

For our purpose, we first construct a strong-coupling theory which enables us to examine normal state properties of a Bose-Fermi mixture, from the weak-coupling to the strong-coupling regime. As we will point out in Chap. 2 the ordinary non-self-consistent strong-coupling T-matrix approximation (TMA), which has been extensively used in an ultracold Fermi gas to successfully explain various strong-coupling phenomenon in the BCS-BEC crossover region, does not work well when applied to a Bose-Fermi mixture. Thus, in Chap. 2 we improve TMA so that this difficulty is overcome.

Using this improved TMA (iTMA), we examine strong-coupling corrections to single-particle properties of a Bose-Fermi mixture in Chap. 3, by explicitly evaluating single-particle density of states, as well as the single-particle spectral weight, in both the Bose and Fermi components, to clarify how strong hetero-pairing fluctuations affect these quantities. We also compare our results on a Bose-Fermi mixture with the case of a two-component Fermi gas, to clarify the origin of the difference between the two.

In Chap. 4, we combine the above mentioned iTMA with universal thermodynamics to study the normal-state thermodynamic properties of a Bose-Fermi mixture in the unitarity limit (unitary Bose-Fermi mixture). We show that the specific heat at constant volume C_V exhibits an anomalous non-monotonic behavior near $T_{\rm BEC}$, as a result of existing strong hetero-pairing fluctuations in a unitary Bose-Fermi mixture.

We summarize this thesis in Chap. 5, where we also present future problems.

Throughout this thesis, we take $\hbar = k_{\rm B} = 1$, and the system volume to be unity (unless any confusion may occur), for simplicity.

Chapter 2

Non-self-consistent T-matrix Approximation (TMA) and Need for Improved TMA

In this chapter, we explain our theoretical formulation to deal with strong-coupling properties of a Bose-Fermi mixture, consisting of single-component bosons and single-component fermions. After presenting our model Hamiltonian, we review the ordinary non-self-consistent T-matrix approximation (TMA), which has been extensively used to investigate effects of pairing fluctuations in a strongly-interacting two-component Fermi gas [58–61]. TMA has also been recently applied to a Bose-Fermi mixture [44–46]. We explain how TMA can describe the so-called pseudogap phenomenon in the BCS (Bardeen-Cooper-Schrieffer)- BEC (Bose-Einstein condensation) crossover regime of an ultracold Fermi gas. We then point out that TMA gives *unphysical* results when applied to a Bose-Fermi mixture. To cure this we present an improved version of this strong-coupling theory, to show that it can indeed eliminate this problem in the strong coupling regime which one encounters while using ordinary TMA. We use this improved T-matrix approximation (iTMA) in considering the strong-coupling properties of a Bose-Fermi mixture in Chap. 3 and 4.

2.1 Model Hamiltonian and Single-particle Thermal Green's Function

We consider an attractively interacting gas mixture of single-component fermions and single-component bosons described by the model Hamiltonian [44, 86],

$$H = \sum_{\boldsymbol{p},\mathrm{s}=\mathrm{B},\mathrm{F}} \xi^{\mathrm{s}}_{\boldsymbol{p}} c^{\dagger}_{\mathrm{s},\boldsymbol{p}} c_{\mathrm{s},\boldsymbol{p}} - U_{\mathrm{BF}} \sum_{\boldsymbol{p},\boldsymbol{p}',\boldsymbol{q}} c^{\dagger}_{\mathrm{B},\boldsymbol{p}+\boldsymbol{q}/2} c^{\dagger}_{\mathrm{F},-\boldsymbol{p}+\boldsymbol{q}/2} c_{\mathrm{F},-\boldsymbol{p}'+\boldsymbol{q}/2} c_{\mathrm{B},\boldsymbol{p}'+\boldsymbol{q}/2}. \tag{2.1}$$

Here, $c_{\mathrm{s},\boldsymbol{p}}$ is the annihilation operator of a Bose ($\mathrm{s} = \mathrm{B}$) and Fermi ($\mathrm{s} = \mathrm{F}$) atom, with momentum $\boldsymbol{p}$ and atomic masses m_{B} and m_{F}, respectively. The kinetic energies of the atoms are given by,

$$\xi^{\mathrm{s}=\mathrm{B},\mathrm{F}}_{\boldsymbol{p}} = \varepsilon^{\mathrm{s}}_{\boldsymbol{p}} - \mu_{\mathrm{s}} = \frac{\boldsymbol{p}^2}{2m_{\mathrm{s}}} - \mu_{\mathrm{s}}, \tag{2.2}$$

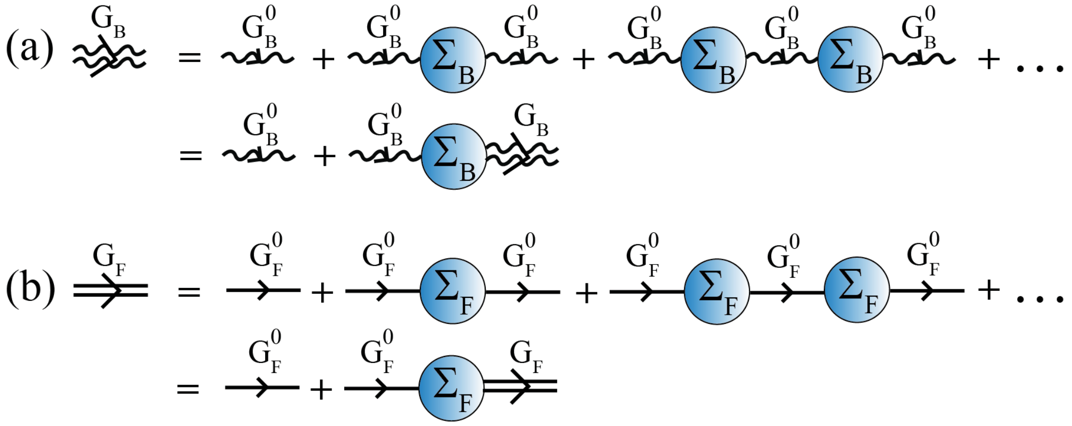

Figure 2.1: Diagrammatic representation of Dyson's equation for single-particle thermal Green's function. (a) Bose component, (b) Fermi component. Double wavy line and double solid line represent the dressed Bose Green's function $G_{\rm B}(\boldsymbol{p}, i\omega_n^{\rm B})$ and the dressed Fermi Green's function $G_{\rm F}(\boldsymbol{p}, i\omega_n^{\rm F})$, respectively. $\Sigma_{\rm s=B,F}(\boldsymbol{p}, i\omega_n^{\rm s})$ are Fermi (s = F) and Bose (s = B) self-energies. The wavy line and solid line describe the bare Bose Green's function $G^0_{\rm B}(\boldsymbol{p}, i\omega_n^{\rm B})$ and the bare Fermi Green's function $G^0_{\rm F}(\boldsymbol{p}, i\omega_n^{\rm F})$, respectively.

measured from the Bose (Fermi) chemical potential $\mu_{\rm B}$ ($\mu_{\rm F}$). The second term denotes a contact-type attractive inter-species interaction $-U_{\rm BF}$ (< 0), which is assumed to be tunable by adjusting the threshold energy of a hetero-nuclear Feshbach resonance [23]. In this thesis, we ignore any other interactions such as Bose-Bose interaction, (non-s-wave) Fermi-Fermi interaction, for simplicity. (Note, that an s-wave interaction does not exist between fermions because of Pauli's exclusion principle.) Although a real Bose-Fermi mixture is experimentally prepared in a harmonic trap [11], effects of this spatial inhomogeneity is not considered as we take the simplest uniform case. In addition to those, although we explain our formulation in the case of $m_{\rm B} \neq m_{\rm F}$, we will take $m_{\rm B} = m_{\rm F} (= m)$ in our strong-coupling theory. Improving these simplifications remain as our future challenges.

As usual, our model Bose-Fermi mixture described by the Hamiltonian in Eq. (2.1) involves the ultraviolet divergence associated with the contact-type interaction $-U_{\rm BF}$. This singularity is conveniently eliminated by measuring the interaction strength in terms of the inverse Bose-Fermi s-wave scattering length $a_{\rm BF}^{-1}$. The scattering length $a_{\rm BF}$ is related to the bare interaction $U_{\rm BF}$ as [56],

$$\frac{2\pi a_{\rm BF}}{m_{\rm r}} = -\frac{U_{\rm BF}}{1 - U_{\rm BF}\sum_{\boldsymbol{p}}^{p_{\rm c}} \frac{2m_{\rm r}}{\boldsymbol{p}^2}}, \tag{2.3}$$

where,

$$m_{\rm r} = \frac{m_{\rm B} m_{\rm F}}{m_{\rm B} + m_{\rm F}}, \tag{2.4}$$

is the reduced mass and $p_{\rm c}$ is a high-momentum cutoff.

To examine the single-particle properties of a Bose-Fermi mixture and effects of strong inter-species interaction $-U_{\rm BF}$, it is convenient to consider the single-particle thermal Green's function ($\mathrm{s} = \mathrm{B}, \mathrm{F}$),

$$G_{\mathrm{s}}(\boldsymbol{p}, \tau) = -\langle T_\tau [c_{\mathrm{s},\boldsymbol{p}}(\tau) c^\dagger_{\mathrm{s},\boldsymbol{p}}(0)] \rangle. \tag{2.5}$$

Here, T_τ is the time ordering operator in terms of the imaginary time τ, and

$$c_{\mathrm{s},\boldsymbol{p}}(\tau) = e^{H\tau} c_{\mathrm{s},\boldsymbol{p}}(0) e^{-H\tau}. \tag{2.6}$$

In Eq. (2.5) $\langle \hat{O} \rangle$ denotes the ordinary statistical average,

$$\langle \hat{O} \rangle = \frac{1}{Z} \mathrm{Tr}[e^{-\beta H} \hat{O}], \tag{2.7}$$

where $Z = \mathrm{Tr}(e^{-\beta H})$ is the partition function. The single-particle thermal Green's function in the Matsubara-frequency representation is obtained from the Fourier transformation [87–90],

$$G_{\mathrm{s}}(\boldsymbol{p}, i\omega_n^{\mathrm{s}}) = \int_0^\beta d\tau e^{i\omega_n^{\mathrm{s}}\tau} G_{\mathrm{s}}(\boldsymbol{p}, \tau), \tag{2.8}$$

where $\beta = 1/T$ is the inverse of temperature T. $\omega_n^{\mathrm{B}} = 2n\pi T$ and $\omega_n^{\mathrm{F}} = (2n+1)\pi T$ $(n = 0, \pm 1, \pm 2, \pm 3, \cdots)$ represent the boson and fermion Matsubara frequencies, respectively.

In the non-interacting case ($U_{\mathrm{BF}} = 0$) the single-particle Green's function ($\equiv G_{\mathrm{s}}^0$) has the form [87–90],

$$G_{\mathrm{s}}^0(\boldsymbol{p}, i\omega_n^{\mathrm{s}}) = \frac{1}{i\omega_n^{\mathrm{s}} - \xi_{\boldsymbol{p}}^{\mathrm{s}}}. \tag{2.9}$$

Using this bare Green's function G_{s}^0, we can diagrammatically construct the dressed Green's function G_{s}, as shown in Fig. 2.1, which gives the Dyson equation,

$$G_{\mathrm{s}}(\boldsymbol{p}, i\omega_n^{\mathrm{s}}) = G_{\mathrm{s}}^0(\boldsymbol{p}, i\omega_n^{\mathrm{s}}) + G_{\mathrm{s}}^0(\boldsymbol{p}, i\omega_n^{\mathrm{s}}) \Sigma_{\mathrm{s}}(\boldsymbol{p}, i\omega_n^{\mathrm{s}}) G_{\mathrm{s}}(\boldsymbol{p}, i\omega_n^{\mathrm{s}}). \tag{2.10}$$

Here, the self-energy $\Sigma_{\mathrm{s}}(\boldsymbol{p}, i\omega_n^{\mathrm{s}})$ conveniently describes interaction effects on single-particle properties of the system. Equation (2.10) can be written as,

$$\begin{aligned} G_{\mathrm{s}}(\boldsymbol{p}, i\omega_n^{\mathrm{s}}) &= \frac{1}{[G_{\mathrm{s}}^0(\boldsymbol{p}, i\omega_n^{\mathrm{s}})]^{-1} - \Sigma_{\mathrm{s}}(\boldsymbol{p}, i\omega_n^{\mathrm{s}})} \\ &= \frac{1}{i\omega_n^{\mathrm{s}} - \xi_{\boldsymbol{p}}^{\mathrm{s}} - \Sigma_{\mathrm{s}}(\boldsymbol{p}, i\omega_n^{\mathrm{s}})}, \end{aligned} \tag{2.11}$$

2.2 Non-self-consistent T-matrix Approximation (TMA) : Bose-Fermi Mixture

In this section, we explain the theoretical framework of the ordinary non-self-consistent T-matrix approximation (TMA) in case of a Bose-Fermi mixture. We will extend this strong-coupling theory in Sec. 2.5.

In ordinary TMA, effects of strong-coupling corrections are conveniently incorporated into the theory via Bose ($\mathrm{s} = \mathrm{B}$) and Fermi ($\mathrm{s} = \mathrm{F}$) self-energies $\Sigma_{\mathrm{s}}(\boldsymbol{p}, i\omega_n^{\mathrm{s}})$

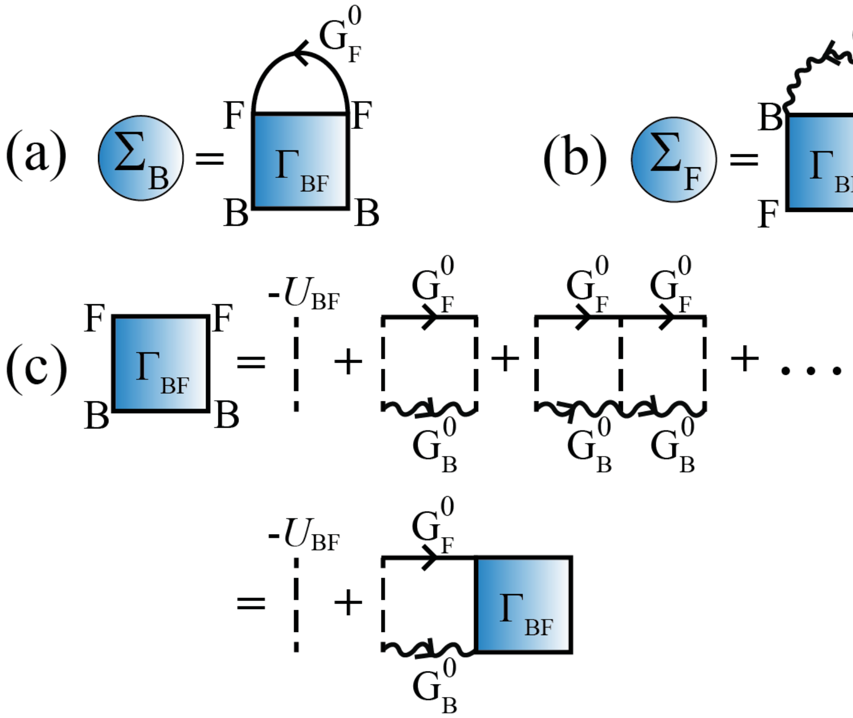

Figure 2.2: Self-energy corrections in the ordinary TMA [44]. (a) Bose self-energy $\Sigma_{\rm B}(\boldsymbol{p}, i\omega_n^{\rm B})$, (b) Fermi self-energy $\Sigma_{\rm F}(\boldsymbol{p}, i\omega_n^{\rm F})$. (c) Bose-Fermi scattering matrix $\Gamma_{\rm BF}$ in TMA. The wavy line and solid line are the bare Bose Green's function ($G^0_{\rm B}$) and the bare Fermi Green's function ($G^0_{\rm F}$), respectively. The dashed line is the attractive inter-species interaction $-U_{\rm BF}$ (< 0).

that are diagrammatically given in the Fig. 2.2 [44]. Summing up these diagrams, we obtain

$$\Sigma_{\rm B}(\boldsymbol{p}, i\omega_n^{\rm B}) = T \sum_{\boldsymbol{q},\omega_m^{\rm F}} \Gamma_{\rm BF}(\boldsymbol{q}, i\omega_m^{\rm F}) G^0_{\rm F}(\boldsymbol{q}-\boldsymbol{p}, i\omega_m^{\rm F} - i\omega_n^{\rm B}) e^{(i\omega_m^{\rm F} - i\omega_n^{\rm B})\delta}, \tag{2.12}$$

$$\Sigma_{\rm F}(\boldsymbol{p}, i\omega_n^{\rm F}) = -T \sum_{\boldsymbol{q},\omega_m^{\rm F}} \Gamma_{\rm BF}(\boldsymbol{q}, i\omega_m^{\rm F}) G^0_{\rm B}(\boldsymbol{q}-\boldsymbol{p}, i\omega_m^{\rm F} - i\omega_n^{\rm F}) e^{(i\omega_m^{\rm F} - i\omega_n^{\rm F})\delta}, \tag{2.13}$$

where δ is a small positive number. $\Gamma_{\rm BF}(\boldsymbol{q}, i\omega_m^{\rm F})$ is the Bose-Fermi particle-particle scattering matrix, describing Bose-Fermi hetero-nuclear pairing fluctuations given by the ladder-type diagrams in Fig. 2.2(c). The TMA expression for $\Gamma_{\rm BF}(\boldsymbol{q}, i\omega_m^{\rm F})$ is given by

$$\begin{aligned} \Gamma_{\rm BF}(\boldsymbol{q}, i\omega_m^{\rm F}) &= -\frac{U_{\rm BF}}{1 - U_{\rm BF}\Pi_{\rm BF}(\boldsymbol{q}, i\omega_m^{\rm F})} \\ &= \frac{\frac{2\pi a_{\rm BF}}{m_{\rm r}}}{1 + \frac{2\pi a_{\rm BF}}{m_{\rm r}} \left[\Pi_{\rm BF}(\boldsymbol{q}, i\omega_m^{\rm F}) - \sum_{\boldsymbol{p}}^{p_{\rm c}} \frac{2m_{\rm r}}{\boldsymbol{p}^2} \right]}, \end{aligned} \tag{2.14}$$

where we have replaced the bare interaction $-U_{\rm BF}$ by the s-wave scattering length

$a_{\rm BF}$ using Eq. (2.3) in obtaining the second line in Eq. (2.14).

$$\begin{aligned}\Pi_{\rm BF}(\boldsymbol{q}, i\omega_m^{\rm F}) &= T\sum_{\boldsymbol{k},\omega_n^{\rm B}} G_{\rm F}^0(-\boldsymbol{k}+\frac{\boldsymbol{q}}{2}, i\omega_m^{\rm F}-i\omega_n^{\rm B})G_{\rm B}^0(\boldsymbol{k}+\frac{\boldsymbol{q}}{2}, i\omega_n^{\rm B}) \\ &= -\sum_{\boldsymbol{k}} \frac{1-n_{\rm F}(\xi^{\rm F}_{\boldsymbol{k}+\boldsymbol{q}/2})+n_{\rm B}(\xi^{\rm B}_{-\boldsymbol{k}+\boldsymbol{q}/2})}{i\omega_m^{\rm F}-\xi^{\rm F}_{\boldsymbol{k}+\boldsymbol{q}/2}-\xi^{\rm B}_{-\boldsymbol{k}+\boldsymbol{q}/2}}, \qquad (2.15)\end{aligned}$$

is the lowest order hetero-nuclear pair correlation function with

$$n_{\rm s=B,F}(\xi^{\rm s}_{\boldsymbol{p}}) = \frac{1}{e^{\beta\xi^{\rm s}_{\boldsymbol{p}}}\pm 1}, \qquad (2.16)$$

being the Fermi (s = F, upper sign) and Bose (s = B, lower sign) distribution functions, respectively. In obtaining the second line of Eq. (2.15) we have summed up the Matsubara frequency ($\omega_n^{\rm B}$) summation, by using the complex integration method explained in Appendix A.

We briefly note that the fact that particle-particle scattering matrix $\Gamma_{\rm BF}(\boldsymbol{q}, i\omega_m^{\rm F})$ in Eq. (2.14) is a function of fermion Matsubara frequency $\omega_m^{\rm F}$, reflecting the fermionic character of Bose-Fermi hetero-pairing fluctuations.

We also note that the pair-correlation function $\Pi_{\rm BF}(\boldsymbol{q}, i\omega_m^{\rm F})$ in Eq. (2.15) involves the ultraviolet divergence, which is however canceled out by the last term $\sum_{\boldsymbol{p}}^{p_c} 2m_{\rm r}/\boldsymbol{p}^2$, in the denominator in Eq. (2.14). Thus, using the second line in Eq. (2.14), one actually does not meet this singularity in this theory.

In TMA, the Bose-Einstein condensation (BEC) transition temperature $T_{\rm BEC}$ is determined from the gapless condition for Bose excitations [44–46]. This condition is achieved when the dressed Bose Green's function $G_{\rm B}(\boldsymbol{p}, i\omega_n^{\rm B})$ in Eq. (2.11) has a pole at $\boldsymbol{p} = \omega_n^{\rm B} = 0$, which gives

$$\mu_{\rm B} = \Sigma_{\rm B}(\boldsymbol{q}=0, i\omega_n^{\rm B}=0). \qquad (2.17)$$

Equation (2.17) may be viewed as an extension of the Hugenholtz-Pines condition [91] for interacting bosons to the case of a Bose-Fermi mixture. (We explain this extension in Appendix B.) We actually solve $T_{\rm BEC}$-equation in Eq. (2.17), together with the equation for the number $N_{\rm B}$ of Bose atoms,

$$N_{\rm B} = -T\sum_{\boldsymbol{p},\omega_n^{\rm B}} G_{\rm B}(\boldsymbol{p}, i\omega_n^{\rm B})e^{i\omega_n^{\rm B}\delta}, \qquad (2.18)$$

as well as the equation for the number $N_{\rm F}$ of Fermi atoms,

$$N_{\rm F} = T\sum_{\boldsymbol{p},\omega_n^{\rm F}} G_{\rm F}(\boldsymbol{p}, i\omega_n^{\rm F})e^{i\omega_n^{\rm F}\delta}, \qquad (2.19)$$

to determine $T_{\rm BEC}$, $\mu_{\rm B}(T_{\rm BEC})$, and $\mu_{\rm F}(T_{\rm BEC})$ self-consistently. In the normal phase above $T_{\rm BEC}$, we only deal with the number equations (2.18) and (2.19), to obtain $\mu_{\rm B}(T)$ and $\mu_{\rm F}(T)$.

Before ending this section, we briefly note that a crucial character of TMA is that bare Green's functions $G_{\rm B}^0$ and $G_{\rm F}^0$ are used everywhere in the TMA diagrams, shown in Fig. 2.2. Because of this, even when the TMA dressed Bose Green's function satisfies the required gapless condition in Eq. (2.17) at $T_{\rm BEC}$, Bose excitations are inconsistently treated as gapped one in the self-energies $\Sigma_{\rm s=B,F}$, leading to the underestimation of effects of Bose fluctuations on the single-particle excitations near $T_{\rm BEC}$. In Sec. 2.4 we will find that this is the origin of the unphysical behavior of the Fermi chemical potential in the intermediate coupling regime obtained in Ref. [44]. In Sec. 2.5 we will also explain how to overcome this weak point existing in TMA.

2.3 TMA analysis on Pseudogap Phenomenon in an Ultracold Fermi Gas

In cold atom physics, TMA was first applied to an attractively interacting two-component Fermi gas, to study strong-coupling properties in the BCS-BEC crossover region [58–60, 66]. Although what we are dealing within this thesis is a Bose-Fermi mixture, since we will compare our results with the "Fermi-Fermi" case in Chap. 3, we review TMA analysis on an ultracold Fermi gas in the BCS-BEC crossover region.

A two-component Fermi gas is known to be well described by the BCS-type Hamiltonian,

$$H_{\rm F} = \sum_{\boldsymbol{p},\sigma=\uparrow,\downarrow} \xi^{\rm F}_{\boldsymbol{p}} c^\dagger_{\boldsymbol{p},\sigma} c_{\boldsymbol{p},\sigma} - U_{\rm FF} \sum_{\boldsymbol{p},\boldsymbol{p}',\boldsymbol{q}} c^\dagger_{\boldsymbol{p}+\boldsymbol{q}/2,\uparrow} c^\dagger_{-\boldsymbol{p}+\boldsymbol{q}/2,\downarrow} c_{-\boldsymbol{p}'+\boldsymbol{q}/2\downarrow} c_{\boldsymbol{p}'+\boldsymbol{q}/2,\uparrow}, \tag{2.20}$$

where $c_{\boldsymbol{p},\sigma}$ is the annihilation operator of a Fermi atom with pseudospin $\sigma =\uparrow,\downarrow$, describing the two atomic hyperfine states. $-U_{\rm FF}(<0)$ is a contact-type s-wave interaction, which is assumed to be tunable by using a Feshbach resonance. As in the Bose-Fermi case explained in Sec. 2.1, the bare interaction is related to the s-wave scattering length $a_{\rm FF}$ as

$$\frac{4\pi a_{\rm FF}}{m} = -\frac{U_{\rm FF}}{1 - U_{\rm FF}\sum_{\boldsymbol{p}}^{p_{\rm c}} \frac{m}{\boldsymbol{p}^2}}. \tag{2.21}$$

In TMA, the fermion self-energy $\Sigma_{\rm F}(\boldsymbol{p}, i\omega_n^{\rm F})$ is diagrammatically given in Fig. 2.2(b) and (c) where all the Bose Green's function $G^0_{\rm B}$ are replaced by the bare Fermi ones $G^0_{\rm F}$. The resulting expression for TMA self-energy $\Sigma_{\rm F}(\boldsymbol{p}, i\omega_n^{\rm F})$ has the form [58],

$$\Sigma_{\rm F}(\boldsymbol{p}, i\omega_n^{\rm F}) = T \sum_{\boldsymbol{q},\omega_m^{\rm B}} \Gamma_{\rm FF}(\boldsymbol{q}, i\omega_m^{\rm B}) G^0_{\rm F}(\boldsymbol{q}-\boldsymbol{p}, i\omega_m^{\rm B} - i\omega_n^{\rm F}) e^{(i\omega_m^{\rm B}-i\omega_n^{\rm F})\delta}, \tag{2.22}$$

where

$$\begin{aligned} \Gamma_{\rm FF}(\boldsymbol{q}, i\omega_m^{\rm B}) &= -\frac{U_{\rm FF}}{1 - U_{\rm FF}\Pi_{\rm FF}(\boldsymbol{q}, i\omega_m^{\rm B})} \\ &= \frac{\frac{4\pi a_{\rm FF}}{m}}{1 + \frac{4\pi a_{\rm FF}}{m}\left[\Pi_{\rm FF}(\boldsymbol{q}, i\omega_m^{\rm B}) - \sum_{\boldsymbol{p}}^{p_{\rm c}} \frac{m}{\boldsymbol{p}^2}\right]}, \end{aligned} \tag{2.23}$$

with

$$\begin{aligned}\Pi_{\rm FF}(\boldsymbol{q}, i\omega_m^{\rm B}) &= T\sum_{\boldsymbol{k},\omega_n^{\rm F}} G_{\rm F}^0(-\boldsymbol{k}+\frac{\boldsymbol{q}}{2}, i\omega_m^{\rm B}-i\omega_n^{\rm F})G_{\rm F}^0(\boldsymbol{k}+\frac{\boldsymbol{q}}{2}, i\omega_n^{\rm F}) \\ &= -\sum_{\boldsymbol{k}} \frac{1-n_{\rm F}(\xi^{\rm F}_{\boldsymbol{k}+\boldsymbol{q}/2})-n_{\rm F}(\xi^{\rm B}_{-\boldsymbol{k}+\boldsymbol{q}/2})}{i\omega_m^{\rm B}-\xi^{\rm F}_{\boldsymbol{k}+\boldsymbol{q}/2}-\xi^{\rm F}_{-\boldsymbol{k}+\boldsymbol{q}/2}}. \end{aligned} \tag{2.24}$$

The particle-particle scattering matrix $\Gamma_{\rm FF}(\boldsymbol{q}, i\omega_m^{\rm B})$ in Eq. (2.23) describes fluctuations in the Cooper channel. Because of the bosonic character of these fluctuations, the boson Matsubara frequency appears in $\Gamma_{\rm FF}(\boldsymbol{q}, i\omega_m^{\rm B})$ (as well as in $\Pi_{\rm FF}(\boldsymbol{q}, i\omega_m^{\rm B})$). We briefly note that the absence of "$-$" in the form of $\Sigma_{\rm F}(\boldsymbol{p}, i\omega_n^{\rm F})$ in Eq. (2.22) which is seen in the Bose-Fermi case in $\Sigma_{\rm F}(\boldsymbol{p}, i\omega_n^{\rm F})$ in Eq. (2.13) is due to bosonic outer loop in the self-energy diagram in Fig. 2.2(b).

The superfluid phase transition temperature $T_{\rm c}$ in the present Fermi-Fermi case can be conveniently determined from the Thouless criterion [92], stating that the superfluid instability occurs when the Fermi-Fermi particle-particle scattering matrix $\Gamma_{\rm FF}(\boldsymbol{q}, i\omega_m^{\rm B})$ has a pole at $\boldsymbol{q} = \omega_m^B = 0$, as

$$\Gamma_{\rm FF}(\boldsymbol{q}=0, i\omega_m^{\rm B}=0)^{-1}=0. \tag{2.25}$$

In TMA, the Thouless criterion gives the $T_{\rm c}$-equation as

$$1 = -\frac{4\pi a_{\rm FF}}{m}\sum_{\boldsymbol{p}}\left[\frac{1}{2\xi^{\rm F}_{\boldsymbol{p}}}\tanh\left(\frac{\beta}{2}\xi^{\rm F}_{\boldsymbol{p}}\right)-\frac{m}{\boldsymbol{p}^2}\right]. \tag{2.26}$$

As in the Bose-Fermi case, we actually solve the $T_{\rm c}$-equation in Eq. (2.26), together with the equation for the number $N_{\rm F}$ of Fermi atoms,

$$N_{\rm F} = 2T\sum_{\boldsymbol{p},\omega_n^{\rm F}} G_{\rm F}(\boldsymbol{p}, i\omega_n^{\rm F})e^{i\omega_n^{\rm F}\delta}, \tag{2.27}$$

to determine $T_{\rm c}$ and $\mu_{\rm F}(T_{\rm c})$ in a consistent manner. Here, we have assumed a population balanced Fermi gas (where the number $N_\uparrow$ of $\uparrow$-spin atoms equals the number $N_\downarrow$ of $\downarrow$-spin atoms). Above $T_{\rm c}$, we only solve the number equation in Eq. (2.27), to determine $\mu_{\rm F}(T > T_{\rm c})$.

Figure 2.3 shows the self-consistent solution for the TMA coupled $T_{\rm c}$-equation (2.26) with the number equation (2.27). In the weak-coupling BCS regime $(k_{\rm F}a_{\rm FF})^{-1} \lesssim -1$, pairing fluctuations are weak, so that the Fermi chemical potential is close to the Fermi energy $\varepsilon_{\rm F}$ (see Fig. 2.3(b)). In this regime, $T_{\rm c}$ is close to the weak-coupling BCS result $T_{\rm BCS}$, given by [49, 50]

$$T_{\rm BCS} \simeq 0.614\varepsilon_{\rm F}e^{\frac{\pi}{2k_{\rm F}a_{\rm FF}}}, \qquad (k_{\rm F}a_{\rm FF})^{-1} \ll -1. \tag{2.28}$$

However, $T_{\rm c}$ gradually deviates from $T_{\rm BCS}$, with increasing the interaction strength, reflected by the enhancement of (Fermi-Fermi) pairing fluctuations. At the same time, the Fermi chemical potential $\mu_{\rm F}(T_{\rm c})$ gradually deviate from the Fermi energy $\varepsilon_{\rm F}$ to be negative in the strong-coupling BEC regime $(k_{\rm F}a_{\rm FF})^{-1} \gtrsim 1$. In the BEC regime, it has been shown that the particle-particle scattering matrix $\Gamma_{\rm FF}(\boldsymbol{q}, i\omega_m^{\rm B})$ is

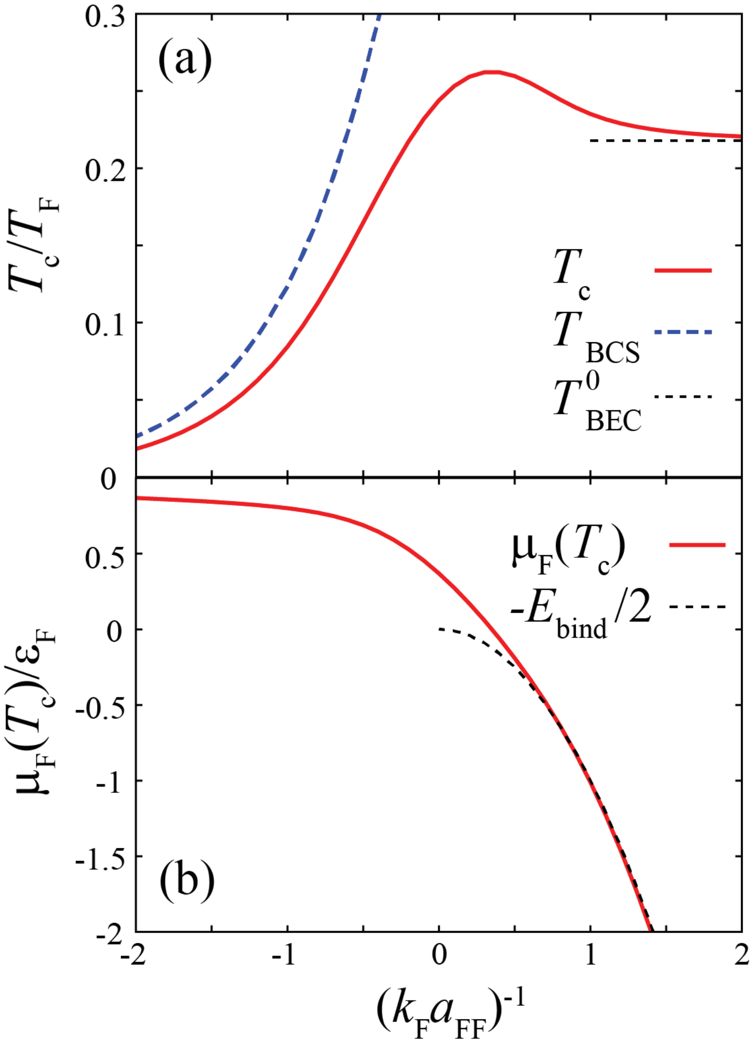

Figure 2.3: Self-consistent solutions for the TMA coupled $T_{\rm c}$-equation (2.26) with the number equation (2.27) in the case of a strongly-interacting two-component Fermi gas. (a) $T_{\rm c}$, (b) $\mu_{\rm F}(T_{\rm c})$. The interaction strength is measured in terms of $a_{\rm FF}^{-1}$, normalized by the Fermi momentum $k_{\rm F}$. In this scale $(k_{\rm F}a_{\rm BF})^{-1} \lesssim -1$ and $(k_{\rm F}a_{\rm BF})^{-1} \gtrsim 1$ correspond to, the weak-coupling regime and strong-coupling regime, respectively.$\varepsilon_{\rm F} = k_{\rm F}^2/2m$ is the Fermi energy. In panel (a), $T_{\rm BCS}$ is the weak-coupling result in Eq. (2.28). $T^0_{\rm BEC}$ is the BEC phase transition temperature of an ideal gas with $N_{\rm F}/2$ Bose molecules. In panel (b) $E_{\rm bind}$ is the binding energy of a two-body bound molecule in Fig. 2.31.

reduced to the molecular Bose Green's function with the molecular mass $M = 2m$ as (For derivation see Appendix C.)

$$\begin{aligned}\Gamma_{\rm FF}(\boldsymbol{q}, i\omega_m^{\rm B}) &\backsimeq \frac{8\pi}{m^2 a_{\rm FF}} G_{\rm B}^{\rm mol}(\boldsymbol{q}, i\omega_m^{\rm B}),\\ &= \frac{8\pi}{m^2 a_{\rm FF}} \frac{1}{i\omega_m^{\rm B} - \xi_{\boldsymbol{q}}^{\rm mol}}, \qquad (k_{\rm F}a_{\rm FF})^{-1} \gg 1. \qquad (2.29)\end{aligned}$$

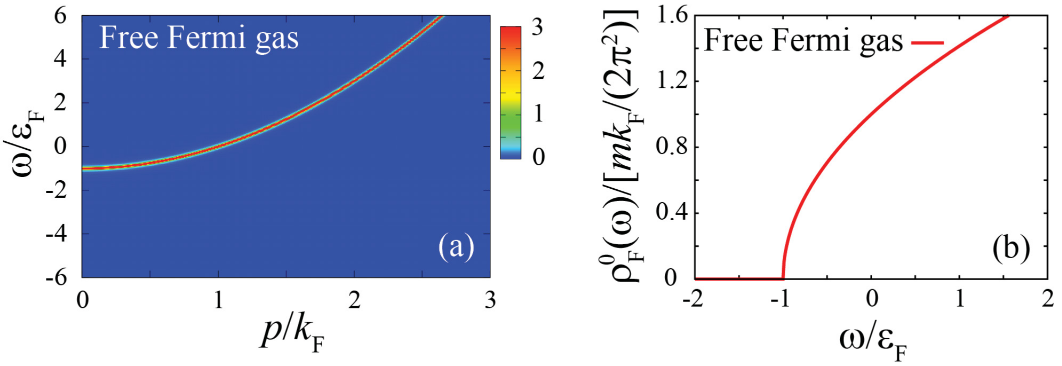

Figure 2.4: Calculated intensity of the single-particle spectral weight $A^0_{\rm F}(\boldsymbol{p},\omega)$ (a), as well as the density of states $\rho^0_{\rm F}(\omega=0)=mk_{\rm F}/(2\pi^2)$ (b), in a free Fermi gas at $T=0$. The intensity of panel (a) is normalized by $\varepsilon_{\rm F}^{-1}$.

Here, $\xi^{\rm mol}_{\boldsymbol{q}}=q^2/(2M)-\mu^{\rm mol}_{\rm B}$ is the molecular kinetic energy, measured from the molecular chemical potential,

$$\mu^{\rm mol}_{\rm B}=2\mu_{\rm F}+E_{\rm bind}, \tag{2.30}$$

with $E_{\rm bind}$ being the magnitude of the binding energy of the two-body bound state given by,

$$E_{\rm bind}=\frac{1}{ma^2_{\rm FF}}. \tag{2.31}$$

In addition, the number equation (2.27) in the BEC limit is reduced to [49, 50],

$$\frac{N_{\rm F}}{2}=\sum_{\boldsymbol{q}} n_{\rm B}\left(\frac{q^2}{2M}-\mu^{\rm mol}_{\rm B}\right), \tag{2.32}$$

which is just the same as the number equation for an ideal Bose gas with $N_{\rm F}/2$ bosons. Physically Eq. (2.32) indicates that the system is dominated by tightly bound Fermi-Fermi molecules. Indeed, one sees in Fig. 2.3(a) that as one enters deep inside the strong-coupling BEC regime ($(k_{\rm F}a_{\rm FF})^{-1}\gg 1$), the calculated $T_{\rm c}$ in TMA approaches

$$T^0_{\rm BEC}=\frac{2\pi}{M}\left(\frac{N_{\rm F}/2}{\zeta(3/2)}\right)^{3/2}, \tag{2.33}$$

of an ideal Bose gas with $N/2$ bosons with the molecular mass $M=2m$ given by Eq. (2.33). Here, $\zeta(3/2)\simeq 2.612$ is the zeta function. In addition, both the Thouless condition for Eq. (2.29) and the BEC condition in Eq. (2.26) give

$$\mu_{\rm F}(T_c)=-\frac{E_{\rm bind}}{2}, \tag{2.34}$$

which can be seen in Fig. 2.3(b) in the strong-coupling BEC regime.

An advantage of using TMA in an ultracold Fermi gas is that one can examine single-particle spectral weight $A_{\rm F}(\boldsymbol{p},\omega)$ as well as single-particle density of states

$\rho_{\rm F}(\omega)$, over the entire BCS-BEC crossover region. These quantities are related to the analytic continued TMA Green's function $G_{\rm F}(\boldsymbol{p}, i\omega_n^{\rm F} \to \omega + i\delta)$ as

$$A_{\rm F}(\boldsymbol{p},\omega) = -\frac{1}{\pi}{\rm Im}\left[G_{\rm F}(\boldsymbol{p}, i\omega_n^{\rm F} \to \omega + i\delta)\right], \tag{2.35}$$

$$\begin{aligned}\rho_{\rm F}(\omega) &= -\frac{1}{\pi}\sum_{\boldsymbol{p}}{\rm Im}\left[G_{\rm F}(\boldsymbol{p}, i\omega_n^{\rm F} \to \omega + i\delta)\right] \\ &= \sum_{\boldsymbol{p}} A_{\rm s}(\boldsymbol{p},\omega).\end{aligned} \tag{2.36}$$

We briefly note that the analytic continued thermal Green's function $G_{\rm F}(\boldsymbol{p}, i\omega_n^{\rm F} \to \omega + i\delta)$ is just the retarded Green's function $G_{\rm F}^{\rm R}(\boldsymbol{p},\omega)$.

The simplest non-interacting case at $T = 0$, one has

$$\begin{aligned}G_{\rm F}^0(\boldsymbol{p}, i\omega_n^{\rm F} \to \omega + i\delta) = G_{\rm F}^{\rm 0R}(\boldsymbol{p},\omega) &= \frac{1}{\omega + i\delta - \xi_{\boldsymbol{p}}^{\rm F}} \\ &= P\left(\frac{1}{\omega - \xi_{\boldsymbol{p}}^{\rm F}}\right) - i\pi\delta(\omega - \xi_{\boldsymbol{p}}^{\rm F}),\end{aligned} \tag{2.37}$$

where P means taking Cauchy's principal value. Substituting Eq. (2.37) into Eqs. (2.35) and (2.36), we obtain

$$A_{\rm F}^0(\boldsymbol{p},\omega) = \delta(\omega - \xi_{\boldsymbol{p}}^{\rm F}), \tag{2.38}$$

$$\begin{aligned}\rho_{\rm F}^0(\omega) &= \sum_{\boldsymbol{p}} A_{\rm F}^0(\boldsymbol{p},\omega) \\ &= \frac{m^{3/2}}{\sqrt{2}\pi^2}\sqrt{\omega + \varepsilon_{\rm F}}.\end{aligned} \tag{2.39}$$

We plot these in Fig. 2.4.

Figure 2.5 shows the Fermi density of states (DOS) $\rho_{\rm F}(\omega)$ in the BCS-BEC crossover regime of an ultracold Fermi gas at $T_{\rm c}$. Although the superfluid gap vanishes at $T_{\rm c}$, one sees in Fig. 2.5 a BCS-state like dip structure around $\omega = 0$, which develops as one passes through the unitarity limit ($(k_{\rm F}a_{\rm FF})^{-1} = 0$). This dip structure is sometimes referred to as the pseudogap associated with strong-pairing fluctuations existing in the BCS-BEC crossover region near $T_{\rm c}$.

The corresponding anomaly is seen in the spectral intensity $A_{\rm F}(\boldsymbol{p},\omega)$, as shown in Fig. 2.6. In contrast to the single spectral peak line along the free particle dispersion $\omega = p^2/2m - \varepsilon_{\rm F}$ seen in Fig. 2.4(a), the splitting of the dispersion is seen in Fig. 2.6, which becomes more remarkable for a stronger pairing interaction. Since DOS is given by the momentum summation of the spectral weight $A_{\rm F}(\boldsymbol{p},\omega)$ (see Eq. (2.36)), the suppression of the spectral intensity around $\omega = 0$ in Fig. 2.6(b) and (c) agrees with the suppression of $\rho_{\rm F}(\omega)$ around $\omega = 0$ in Fig. 2.5.

It has been shown that the above pseudogap phenomenon can be explained as a particle-hole coupling effect caused by strong fluctuations in the Cooper channel

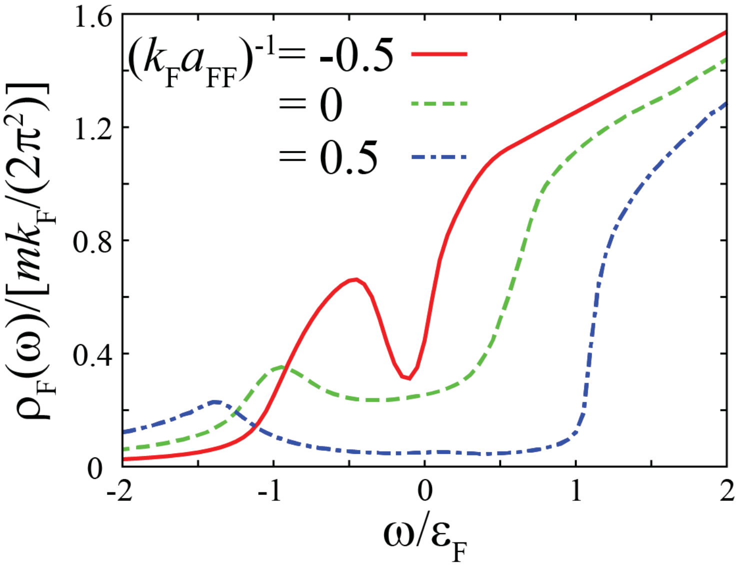

Figure 2.5: Calculated Fermi density of states $\rho_{\rm F}(\omega)$ in the BCS-BEC crossover regime of an ultracold Fermi gas at $T_{\rm c}$.

[58–60, 66]. Noting that the low energy and low momentum pairing fluctuations described by the particle-particle scattering matrix $\Gamma_{\rm FF}$ are enhanced near $T_{\rm c}$ (Note that $\Gamma_{\rm FF}(0,0)$ diverges at $T_{\rm c}$ because of the Thouless criterion in Eq. (2.25)),

$$\begin{aligned}
\Sigma_{\rm F}(\boldsymbol{p}, i\omega^{\rm F}_n) &= T\sum_{\boldsymbol{q},\omega^{\rm B}_m}\Gamma_{\rm FF}(\boldsymbol{q}, i\omega^{\rm B}_m)G^0_{\rm F}(\boldsymbol{q}-\boldsymbol{p}, i\omega^{\rm B}_m - i\omega^{\rm F}_n)e^{(i\omega^{\rm B}_{n'}-i\omega^{\rm F}_m)\delta} \\
&\simeq TG^0_{\rm F}(-\boldsymbol{p}, -i\omega^{\rm F}_n)\sum_{\boldsymbol{q},\omega^{\rm B}_m}\Gamma_{\rm FF}(\boldsymbol{q}, i\omega^{\rm B}_m)e^{i\omega^{\rm B}_m\delta} \\
&\equiv -G^0_{\rm F}(-\boldsymbol{p}, -i\omega^{\rm F}_n)\Delta^2_{\rm pg}, \qquad (2.40)
\end{aligned}$$

where

$$\Delta^2_{\rm pg} = -T\sum_{\boldsymbol{q},i\omega^{\rm B}_m}\Gamma_{\rm FF}(\boldsymbol{q}, i\omega^{\rm B}_m)e^{i\omega^{\rm B}_m\delta}, \qquad (>0) \qquad (2.41)$$

is sometimes referred to as the pseudogap parameter in the literature [58–60, 66]. Substituting Eq. (2.40) into the TMA Green's function in Eq. (2.11), we obtain

$$G_{\rm F}(\boldsymbol{p}, i\omega^{\rm F}_n) = \frac{1}{i\omega^{\rm F}_n - \xi^{\rm F}_{\boldsymbol{p}} - \frac{\Delta^2_{\rm pg}}{i\omega^{\rm F}_n + \xi^{\rm F}_{\boldsymbol{p}}}}. \qquad (2.42)$$

Equation (2.42) indicates that pairing fluctuations that are described by the particle-particle scattering matrix $\Gamma_{\rm FF}(\boldsymbol{q}, i\omega^{\rm B}_m)$ couple Fermi-particle excitations ($\omega = \xi^{\rm F}_{\boldsymbol{p}}$) with Fermi-hole excitations ($\omega = -\xi^{\rm F}_{\boldsymbol{p}}$), with the coupling constant $\Delta^2_{\rm pg}$. When we rewrite Eq. (2.42) as

$$G_{\rm F}(\boldsymbol{p}, i\omega^{\rm F}_n) = \frac{i\omega^{\rm F}_n + \xi^{\rm F}_{\boldsymbol{p}}}{(i\omega^{\rm F}_n)^2 - (\xi^{\rm F}_{\boldsymbol{p}})^2 - \Delta^2_{\rm pg}}, \qquad (2.43)$$

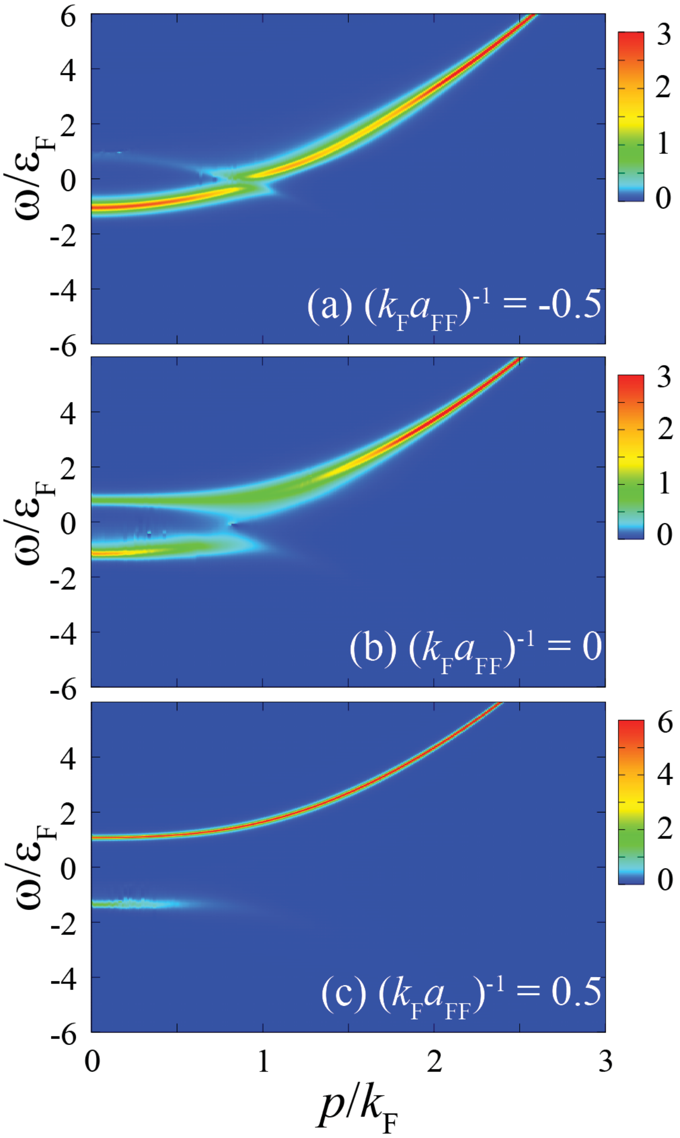

Figure 2.6: Calculated intensity of TMA single-particle spectral weight $A_{\rm F}(\boldsymbol{p},\omega)$ at $T_{\rm c}$. (a) $(k_{\rm F}a_{\rm FF})^{-1}=-0.5$. (b) $(k_{\rm F}a_{\rm FF})^{-1}=0$. (c) $(k_{\rm F}a_{\rm FF})^{-1}=0.5$. The intensity is normalized by $\varepsilon_{\rm F}^{-1}$.

we find that Eq. (2.43) has the same form as the diagonal component of the BCS meanfield Green's function [90],

$$G_{\rm F}^{\rm BCS}(\boldsymbol{p},i\omega_n^{\rm F})=\frac{i\omega_n^{\rm F}+\xi_{\boldsymbol{p}}^{\rm F}}{(i\omega_n^{\rm F})^2-(\xi_{\boldsymbol{p}}^{\rm F})^2-\Delta^2},\tag{2.44}$$

where Δ is the superfluid order parameter. As a result the approximate Green's function in Eq. (2.43) gives a BCS-state like gapped DOS with the energy gap being equal to $2\Delta_{\rm pg}^2$. Actually, pairing fluctuations cause a finite lifetime of quasi-particle excitations, that partially fills up the gap structure, leading to the pseudogap seen in Fig. 2.5. Evaluating the single-particle dispersion from the analytic continued

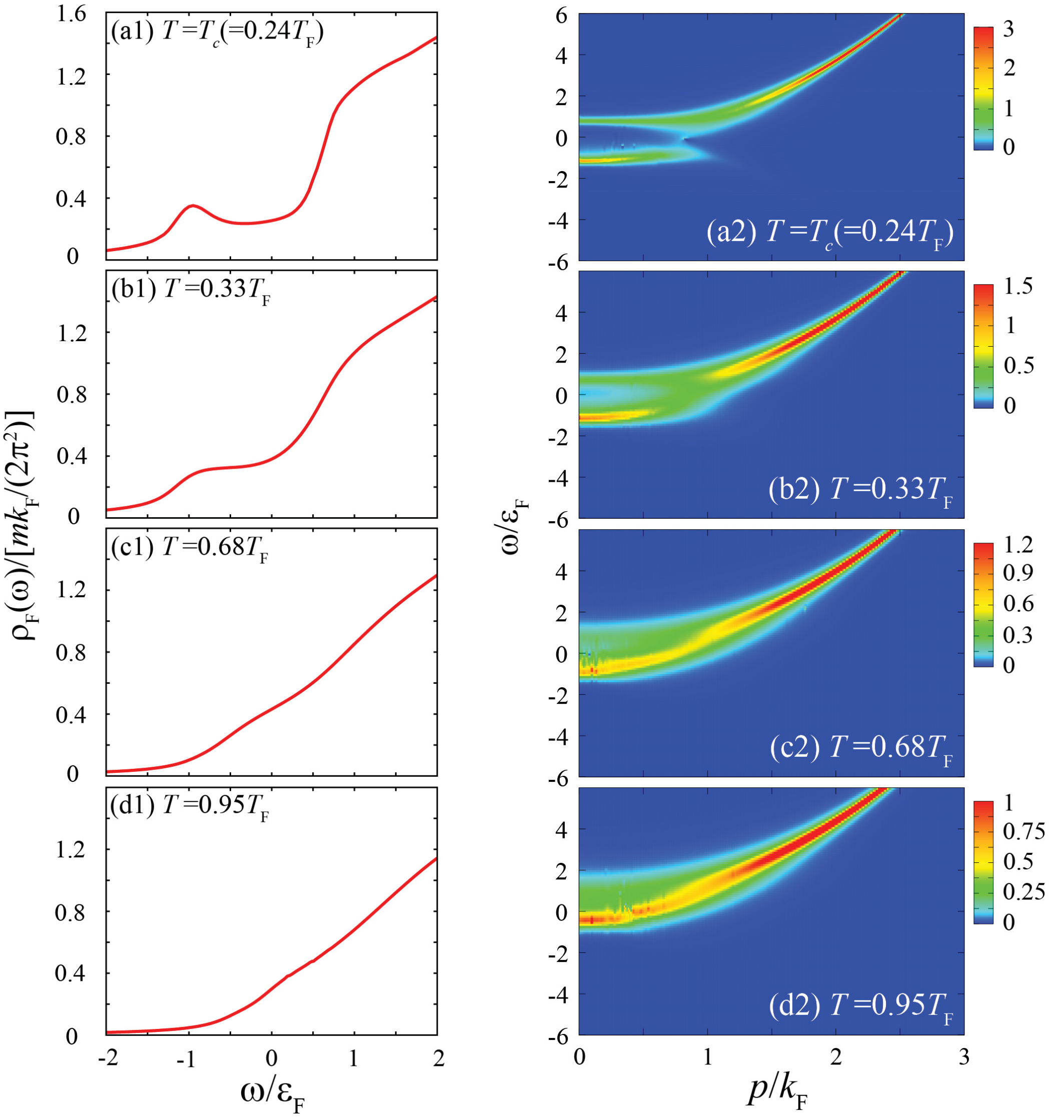

Figure 2.7: Calculated (a1)∼(d1) density of states $\rho_{\rm F}(\omega)$, and (a2)∼(d2) intensity of single-particle spectral weight $A_{\rm F}(\boldsymbol{p},\omega)$ in a Fermi gas at $(k_{\rm F}a_{\rm FF})^{-1}=0$ above $T_{\rm c}$.

Eq. (2.43), one has

$$\omega=\pm\sqrt{(\xi^{\rm F}_{\boldsymbol{p}})^2+\Delta_{\rm pg}^2}=\pm E_{\boldsymbol{p}}. \tag{2.45}$$

Because Eq. (2.43) gives the spectral weight as

$$A_{\rm F}(\boldsymbol{p},\omega)=\frac{1}{2}\left(1+\frac{\xi^{\rm F}_{\boldsymbol{p}}}{E_{\boldsymbol{p}}}\right)\delta(\omega-E_{\boldsymbol{p}})+\frac{1}{2}\left(1-\frac{\xi^{\rm F}_{\boldsymbol{p}}}{E_{\boldsymbol{p}}}\right)\delta(\omega+E_{\boldsymbol{p}}), \tag{2.46}$$

we can also qualitatively explain the splitting of the spectral peak seen in Fig. 2.6.

Figure 2.7 shows DOS $\rho_{\rm F}(\omega)$, as well as the spectral weight $A_{\rm F}(\boldsymbol{p},\omega)$, above $T_{\rm c}$. As expected, the anomalies seen in these quantities at $T_{\rm c}$ gradually disappears as one increases the temperature, reflecting the weakening of low-energy pairing fluctuations.

In the current stage of cold Fermi gas physics, the existence of the pseudogap has not been experimentally confirmed yet, because there is no experimental technique to directly observe DOS in this field. However, the recent photoemission type experiment on a ^{40}K [67–69] Fermi gas has observed an anomalous spectral peak in the unitary regime, which agrees with the calculated photoemission spectrum in TMA.

2.4 Inadequacy of ordinary TMA in a Bose-Fermi Mixture

In the previous section, we showed that TMA can describe the BCS-BEC crossover behavior of T_c as well as the pseudogap phenomenon originating from strong-pairing fluctuations, in an ultracold Fermi gas. In this section however, we point out that the simple application of this strong-coupling approximation to a Bose-Fermi mixture explained in Sec. 2.2 gives an unphysical result on the Fermi chemical potential, implying the need for improvement of TMA [44].

Figure 2.8(a) shows the calculated Bose-Einstein condensation temperature T_BEC in a Bose-Fermi mixture, with $N_\mathrm{F} = N_\mathrm{B} = N$ and $m_\mathrm{F} = m_\mathrm{B} = m$. To obtain this result, we use TMA formalism in Sec. 2.2. In the weak-coupling regime ($(k_\mathrm{F}a_\mathrm{BF})^{-1} \lesssim -1$), T_BEC agrees with the BEC transition temperature T^0_BEC of an ideal gas with N bosons, given in Eq. (2.33). With increasing the strength of the inter-species pairing interaction $(k_\mathrm{F}a_\mathrm{BF})^{-1}$, T_BEC is found to monotonically decrease reflecting the decrease in the number of Bose atoms that can contribute to BEC because of the formation of preformed hetero-molecules. T_BEC eventually vanishes in the strong coupling regime when $(k_\mathrm{F}a_\mathrm{BF})^{-1} \simeq 1.62$ [44]. The system in the stronger coupling side $(k_\mathrm{F}a_\mathrm{BF})^{-1} \gtrsim 1.62$ is considered to be dominated by composite Fermi molecules. As mentioned previously, T_BEC is determined from the gapless condition in Eq. (2.17).

At a glance the behavior of T_BEC shown in Fig. 2.8(a) seems justifying the validity of TMA for a Bose-Fermi mixture. However, as shown in Fig. 2.8(b), the calculated Fermi chemical potential μ_F at T_BEC in TMA still takes a large value ($\mu_\mathrm{F} \simeq 0.62\varepsilon_\mathrm{F}$), even at the interaction strength where T_BEC vanishes. This indicates that there are still many unpaired Fermi and Bose atoms even in the strong-coupling regime ($(k_\mathrm{F}a_\mathrm{BF})^{-1} > 0$), where they can form two-body bound molecules.

In the strong-coupling limit, all the Fermi and Bose atoms would form composite molecular fermions, forming the Fermi surface with the Fermi energy

$$E^\mathrm{M}_\mathrm{F} = \frac{p^2_\mathrm{F}}{2M} = \frac{1}{2}\varepsilon_\mathrm{F}, \tag{2.47}$$

where p_F and ε_F are the Fermi momentum and Fermi energy of a free atomic Fermi gas, respectively. Thus, noting that the binding energy of a two-body bound molecule equals

$$E_\mathrm{bind} = \frac{1}{ma^2_\mathrm{BF}}, \tag{2.48}$$

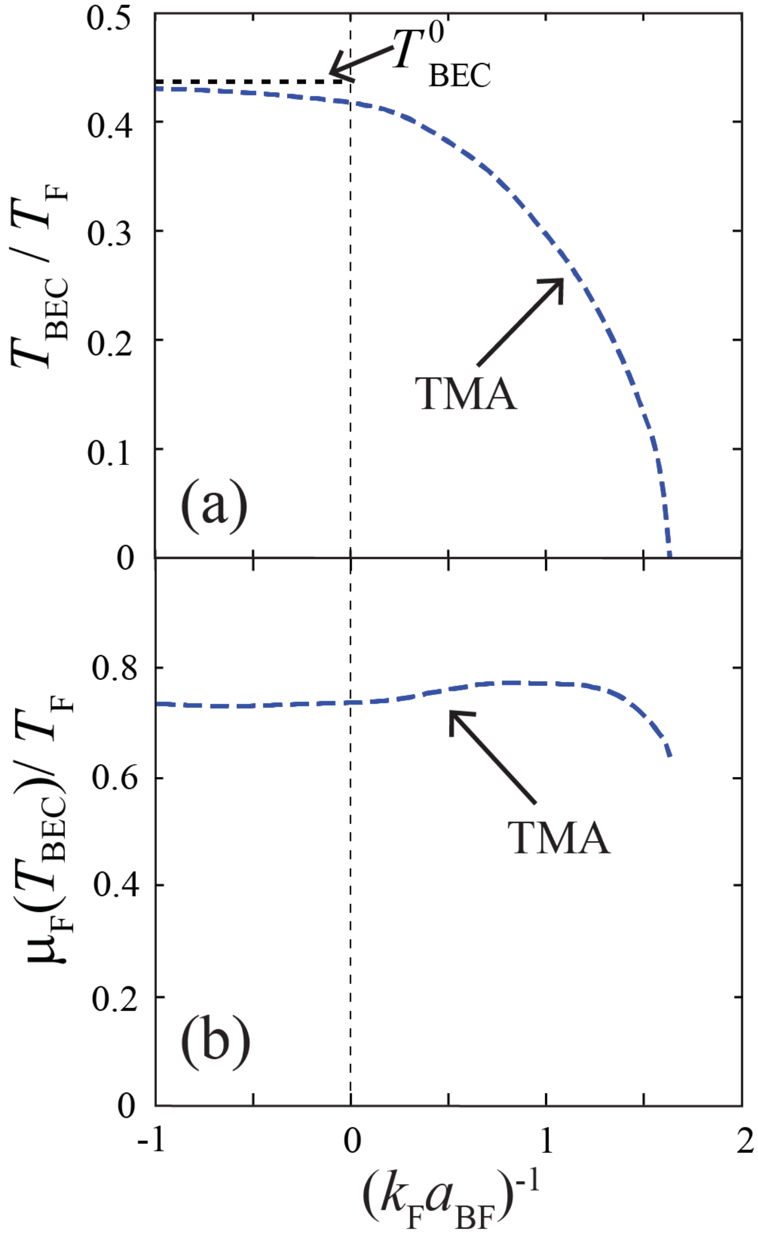

Figure 2.8: TMA self-consistent solution for (a) $T_{\rm BEC}$, and (b) $\mu_{\rm F}(T_{\rm BEC})$ in a Bose-Fermi mixture [44]. $T^0_{\rm BEC}$ is the BEC phase transition temperature in an ideal Bose gas.

we expect the Fermi and Bose chemical potential should approach (For detailed derivation see Appendix C.1.)

$$\begin{aligned}\mu_{\rm B}=\mu_{\rm F} &= -\frac{1}{2}(E_{\rm bind}-E_{\rm F}^{\rm M}) \\ &\simeq -\frac{1}{2ma_{\rm BF}^2}, \qquad (2.49)\end{aligned}$$

in the strong-coupling regime $(k_{\rm F}a_{\rm BF})^{-1}\gtrsim 1$. At the critical interaction strength

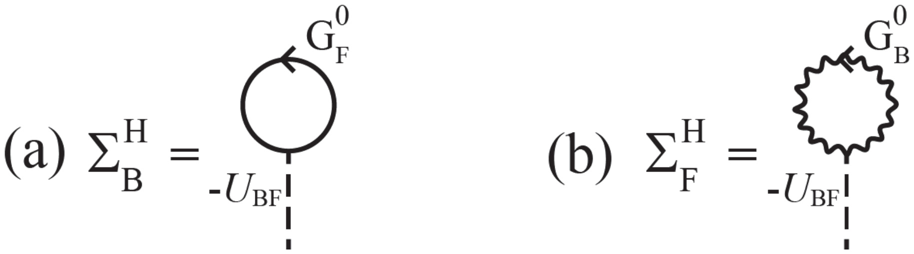

Figure 2.9: Bose (a) and Fermi (b) self-energy in the Hartree approximation. The solid line and wavy line are the bare Fermi $G_{\rm F}^0(\boldsymbol{p}, i\omega_n^{\rm F})$ and Bose $G_{\rm B}^0(\boldsymbol{p}, i\omega_n^{\rm B})$ Green's function, respectively. The dashed line is the attractive inter-species interaction $-U_{\rm BF}(<0)$.

$(k_{\rm F}a_{\rm BF})^{-1} \simeq 1.62$, we have

$$\frac{E_{\rm bind}}{\varepsilon_{\rm F}} = \frac{2}{(k_{\rm F}a_{\rm BF})^2} = 5.25 \gg 1, \tag{2.50}$$

so that the system is expected to be close to a gas of composite molecular fermions. However, as mentioned previously, the positive chemical potential $\mu_{\rm F} = 0.62\varepsilon_{\rm F}$ at the critical interaction strength in "TMA" (see Fig. 2.8(b)) indicates that there are still many unpaired Fermi atoms ($\simeq 0.48N_{\rm F}$) at $T \simeq 0$ [93], despite of this large binding energy in Eq. (2.50). In addition, the existence of unpaired Fermi atoms also means the non-vanishing number of unpaired Bose atoms, that, however, do not exhibit the BEC phase transition in TMA. (Note that $T_{\rm BEC} = 0$ at the critical interaction strength $(k_{\rm F}a_{\rm BF})^{-1} = 1.62$.) These results are clearly unphysical against the situation expected in the strong-coupling regime.

To cure (non-self-consistent) TMA, it would be useful to recall that the non-self-consistent Hartree approximation always gives an unphysical result: The Bose ($\Sigma_{\rm B}^{\rm H}$) and Fermi ($\Sigma_{\rm F}^{\rm H}$) Hartree self-energy are diagrammatic expressed as Fig. 2.9, which gives

$$\Sigma_{\rm B}^{\rm H} = -U_{\rm BF}T\sum_{\boldsymbol{p},\omega_n^{\rm F}} G_{\rm F}^0(\boldsymbol{p}, i\omega_n^{\rm F})e^{i\omega_n^{\rm F}\delta} = -U_{\rm BF}N_{\rm F}^0, \tag{2.51}$$

$$\Sigma_{\rm F}^{\rm H} = U_{\rm BF}T\sum_{\boldsymbol{p},\omega_n^{\rm B}} G_{\rm B}^0(\boldsymbol{p}, i\omega_n^{\rm B})e^{i\omega_n^{\rm B}\delta} = -U_{\rm BF}N_{\rm B}^0, \tag{2.52}$$

where

$$N_{\rm s=B,F}^0 = \sum_{\boldsymbol{p}} n_{\rm s}(\varepsilon_{\boldsymbol{p}} - \mu_{\rm s}) \tag{2.53}$$

The Green's function in this approximation are then given by,

$$G_{\rm B}(\boldsymbol{p}, i\omega_n^{\rm B}) = \frac{1}{i\omega_n^{\rm B} - (\varepsilon_{\boldsymbol{p}} - \mu_{\rm B} - U_{\rm BF}N_{\rm F}^0)}, \tag{2.54}$$

$$G_{\rm F}(\boldsymbol{p}, i\omega_n^{\rm F}) = \frac{1}{i\omega_n^{\rm F} - (\varepsilon_{\boldsymbol{p}} - \mu_{\rm F} - U_{\rm BF}N_{\rm B}^0)}. \tag{2.55}$$

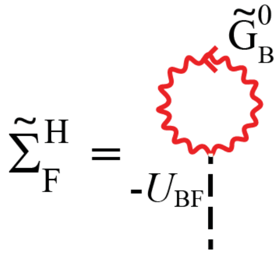

Figure 2.10: Fermi self-energy $\tilde{\Sigma}^{\rm H}_{\rm F}$ in the modified Hartree approximation. $\tilde{G}^0_{\rm B}(\boldsymbol{p}, i\omega^{\rm B}_n)$ is given in Eq. (2.60).

In the non-interacting case ($U_{\rm BF} = 0$), we obtain $\mu_{\rm B} = 0$ and $\mu_{\rm F} = \varepsilon_{\rm F}$ at $T = 0$. On the other hand, in the strong-coupling regime ($U_{\rm BF} \gg \varepsilon_{\rm F}$) at $T = 0$ the coupled number equations

$$N_{\rm B} = \sum_{\boldsymbol{p}} n_{\rm B}(\varepsilon_{\boldsymbol{p}} - \mu_{\rm B} - U_{\rm BF} N^0_{\rm F}), \tag{2.56}$$

and

$$N_{\rm F} = \sum_{\boldsymbol{p}} n_{\rm F}(\varepsilon_{\boldsymbol{p}} - \mu_{\rm F} - U_{\rm BF} N^0_{\rm B}), \tag{2.57}$$

unphysically give double-valued solutions,

$$\begin{cases} \mu_{\rm B} = 0, \\ \mu_{\rm F} = \varepsilon_{\rm F} - U_{\rm BF} N_{\rm B} \qquad (< 0), \end{cases} \tag{2.58}$$

and

$$\begin{cases} \mu_{\rm B} = -U_{\rm BF} N_{\rm F}, \\ \mu_{\rm F} = \varepsilon_{\rm F}. \end{cases} \tag{2.59}$$

For example, substitution of Eq. (2.58) into Eq. (2.53) gives $N^0_{\rm B} = N_{\rm B}$ and $N^0_{\rm F} = 0$, which is immediately found to satisfy Eqs. (2.56) and (2.57). The same discussion also confirms the second solution in Eq. (2.59).

These two solutions in Eqs. (2.58) and (2.59) are very different from each other, because one solution has a positive Fermi chemical potential ($\mu_{\rm F} = \varepsilon_{\rm F}$) and the other has a negative one ($\mu_{\rm F} = \varepsilon_{\rm F} - U_{\rm BF} N_{\rm B}$). The TMA result shown in Fig. 2.8(b) is somehow close to the second one in Eq. (2.59).

On the other hand, the above mentioned problem of double-valued solution can be removed by replacing $\Sigma^{\rm H}_{\rm F}$ by $\tilde{\Sigma}^{\rm H}_{\rm F}$ shown in Fig. 2.10, where the Bose Green's function $\tilde{G}^0_{\rm B}$ has the form,

$$\begin{aligned} \tilde{G}^0_{\rm B}(\boldsymbol{p}, i\omega^{\rm B}_n) &= \frac{1}{[G^0_{\rm B}(\boldsymbol{p}, i\omega^{\rm B}_n)]^{-1} - \Sigma^{\rm H}_{\rm B}} \\ &= \frac{1}{i\omega^{\rm B}_n - (\varepsilon_{\boldsymbol{p}} - \tilde{\mu}_{\rm B})}. \end{aligned} \tag{2.60}$$

Here $\tilde{\mu}_{\rm B} = \mu_{\rm B} - \Sigma^{\rm H}_{\rm B}$ is the effective Bose chemical potential. Equation (2.60) actually equals the dressed Bose Green's function $G_{\rm B}(\boldsymbol{p}, i\omega^{\rm B}_n)$, so that $\tilde{G}^0_{\rm B}$ in Eq. (2.60) satisfies the gapless condition. When we use the Fermi self-energy $\tilde{\Sigma}_{\rm F}^{\rm H}$, the Bose number equation in Eq. (2.54) is slightly modified to become,

$$N_{\rm B}=\sum_{\boldsymbol{p}} n_{\rm B}(\varepsilon_{\boldsymbol{p}}-\mu_{\rm B}-U_{\rm BF}N_{\rm F}^0), \tag{2.61}$$

and

$$N_{\rm F}=\sum_{\boldsymbol{p}} n_{\rm F}(\varepsilon_{\boldsymbol{p}}-\mu_{\rm F}-U_{\rm BF}N_{\rm B}). \tag{2.62}$$

Equations (2.61) and (2.62) gives the expected single-valued solution,

$$\begin{cases}\mu_{\rm B}=0,\\ \mu_{\rm F}=\varepsilon_{\rm F}-U_{\rm BF}N_{\rm B}.\end{cases} \tag{2.63}$$

This result implies that a modification of the bare Bose Green's function in the TMA self-energies may be a key to solve the problem in TMA when applied to a Bose-Fermi mixture.

2.5 Improved T-matrix Approximation (iTMA)

Based on the discussions in Sec. 2.4, we now improve the ordinary TMA which we explained in Sec. 2.2, so as to meet our condition. To satisfy the gapless Bose excitations at $T_{\rm BEC}$ everywhere in the theory in a simple manner, we replace the bare Bose Green's function $G_{\rm B}^0=[i\omega_n^{\rm B}-(\varepsilon_{\boldsymbol{p}}-\mu_{\rm B})]^{-1}$ appearing in the TMA diagrams in Fig. 2.2 with the modified one [86, 94],

$$\tilde{G}_{\rm B}^0(\boldsymbol{p},i\omega_n^{\rm B})=\frac{1}{i\omega_n^{\rm B}-(\varepsilon_{\boldsymbol{p}}-\mu_{\rm B})-\tilde{\Sigma}_{\rm B}(\boldsymbol{p}=0,i\omega_n^{\rm B}=0)}. \tag{2.64}$$

(In what follows, we only deal with the case with $m_{\rm F}=m_{\rm B}=m$, and $N_{\rm F}=N_{\rm B}=N$, for simplicity.) On the other hand, we retain the same bare Green's function

$$G_{\rm F}^0(\boldsymbol{p},i\omega_n^{\rm F})=\frac{1}{i\omega_n^{\rm F}-(\varepsilon_{\boldsymbol{p}}-\mu_{\rm F})}, \tag{2.65}$$

for fermion lines in Fig. 2.2. The resulting self-energy diagrams for our improved T-matrix approximation (iTMA) is given as Fig. (2.11).

Summing up the diagrams in Fig. 2.11 as in the case of ordinary TMA we obtain the iTMA Bose ($\tilde{\Sigma}_{\rm B}$) and Fermi ($\tilde{\Sigma}_{\rm F}$) self-energies, given by

$$\tilde{\Sigma}_{\rm B}(\boldsymbol{p},i\omega_n^{\rm B})=T\sum_{\boldsymbol{q},\omega_m^{\rm F}}\tilde{\Gamma}_{\rm BF}(\boldsymbol{q},i\omega_m^{\rm F})G_{\rm F}^0(\boldsymbol{q}-\boldsymbol{p},i\omega_m^{\rm F}-i\omega_n^{\rm B})e^{(i\omega_m^{\rm F}-i\omega_n^{\rm B})\delta}, \tag{2.66}$$

$$\tilde{\Sigma}_{\rm F}(\boldsymbol{p},i\omega_n^{\rm F})=-T\sum_{\boldsymbol{q},\omega_m^{\rm F}}\tilde{\Gamma}_{\rm BF}(\boldsymbol{q},i\omega_m^{\rm F})\tilde{G}_{\rm B}^0(\boldsymbol{q}-\boldsymbol{p},i\omega_m^{\rm F}-i\omega_n^{\rm F})e^{(i\omega_m^{\rm F}-i\omega_n^{\rm F})\delta}. \tag{2.67}$$

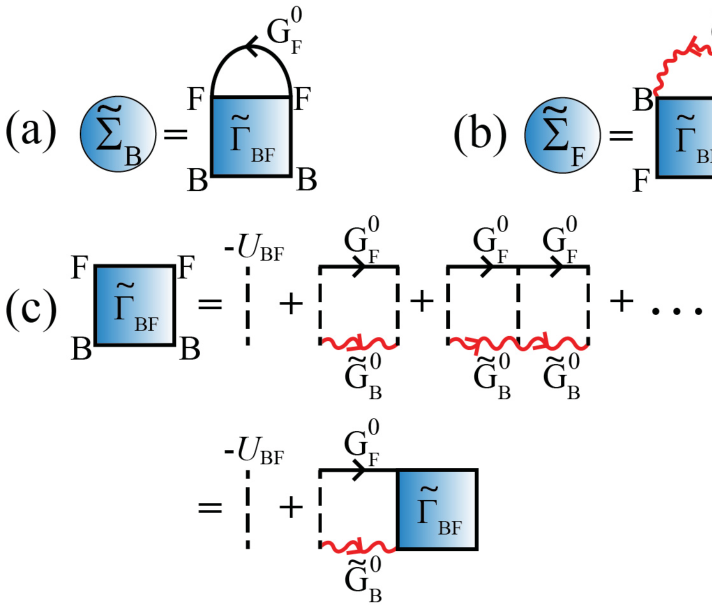

Figure 2.11: Self-energy corrections in our improved TMA (iTMA). (a) Bose self-energy $\tilde{\Sigma}_{\rm B}(\boldsymbol{p}, i\omega_n^{\rm B})$. (b) Fermi self-energy $\tilde{\Sigma}_{\rm F}(\boldsymbol{p}, i\omega_n^{\rm F})$. (c) $\tilde{\Gamma}_{\rm BF}$ is the iTMA boson-fermion scattering matrix. The wavy line and solid line are the Bose Green's function $\tilde{G}^0_{\rm B}(\boldsymbol{p}, i\omega_n^{\rm B})$ in Eq. (2.64) and the bare Fermi Green's function $G^0_{\rm F}(\boldsymbol{p}, i\omega_n^{\rm F})$ in Eq. (2.65), respectively.

Here,

$$\begin{aligned}\tilde{\Gamma}_{\rm BF}(\boldsymbol{q}, i\omega_m^{\rm F}) &= -\frac{U_{\rm BF}}{1 - U_{\rm BF}\tilde{\Pi}_{\rm BF}(\boldsymbol{q}, i\omega_m^{\rm F})} \\ &= \frac{\frac{2\pi a_{\rm BF}}{m_{\rm r}}}{1 + \frac{2\pi a_{\rm BF}}{m_{\rm r}}\left[\tilde{\Pi}_{\rm BF}(\boldsymbol{q}, i\omega_m^{\rm F}) - \sum_{\boldsymbol{p}}^{p_{\rm c}} \frac{2m_{\rm r}}{\boldsymbol{p}^2}\right]},\end{aligned} \tag{2.68}$$

where the iTMA hetero-pair correlation function involves the modified Bose Green's function $\tilde{G}^0_{\rm B}$ as

$$\begin{aligned}\tilde{\Pi}_{\rm BF}(\boldsymbol{q}, i\omega_m^{\rm F}) &= T\sum_{\boldsymbol{k},\omega_n^{\rm B}} G^0_{\rm F}(-\boldsymbol{k} + \frac{\boldsymbol{q}}{2}, i\omega_m^{\rm F} - i\omega_n^{\rm B})\tilde{G}^0_{\rm B}(\boldsymbol{k} + \frac{\boldsymbol{q}}{2}, i\omega_n^{\rm B}) \\ &= -\sum_{\boldsymbol{k}} \frac{1 - n_{\rm F}(\xi^{\rm F}_{\boldsymbol{k}+\boldsymbol{q}/2}) + n_{\rm B}(\tilde{\xi}^{\rm B}_{-\boldsymbol{k}+\boldsymbol{q}/2})}{i\omega_m^{\rm F} - \xi^{\rm F}_{\boldsymbol{k}+\boldsymbol{q}/2} - \tilde{\xi}^{\rm B}_{-\boldsymbol{k}+\boldsymbol{q}/2}}.\end{aligned} \tag{2.69}$$

The resulting single-particle thermal Green's function involves these iTMA corrections as

$$G_{\rm s}(\boldsymbol{p}, \omega) = \frac{1}{i\omega_n^{\rm s} - \xi^{\rm s}_{\boldsymbol{p}} - \tilde{\Sigma}_{\rm s}(\boldsymbol{p}, i\omega_n^{\rm s})}, \tag{2.70}$$

As in the ordinary TMA, BEC transition temperature $T_{\rm BEC}$ is determined from the condition of gapless Bose excitations,

$$\mu_{\rm B} = \tilde{\Sigma}_{\rm B}(\boldsymbol{p} = 0, i\omega_n^{\rm B} = 0). \tag{2.71}$$

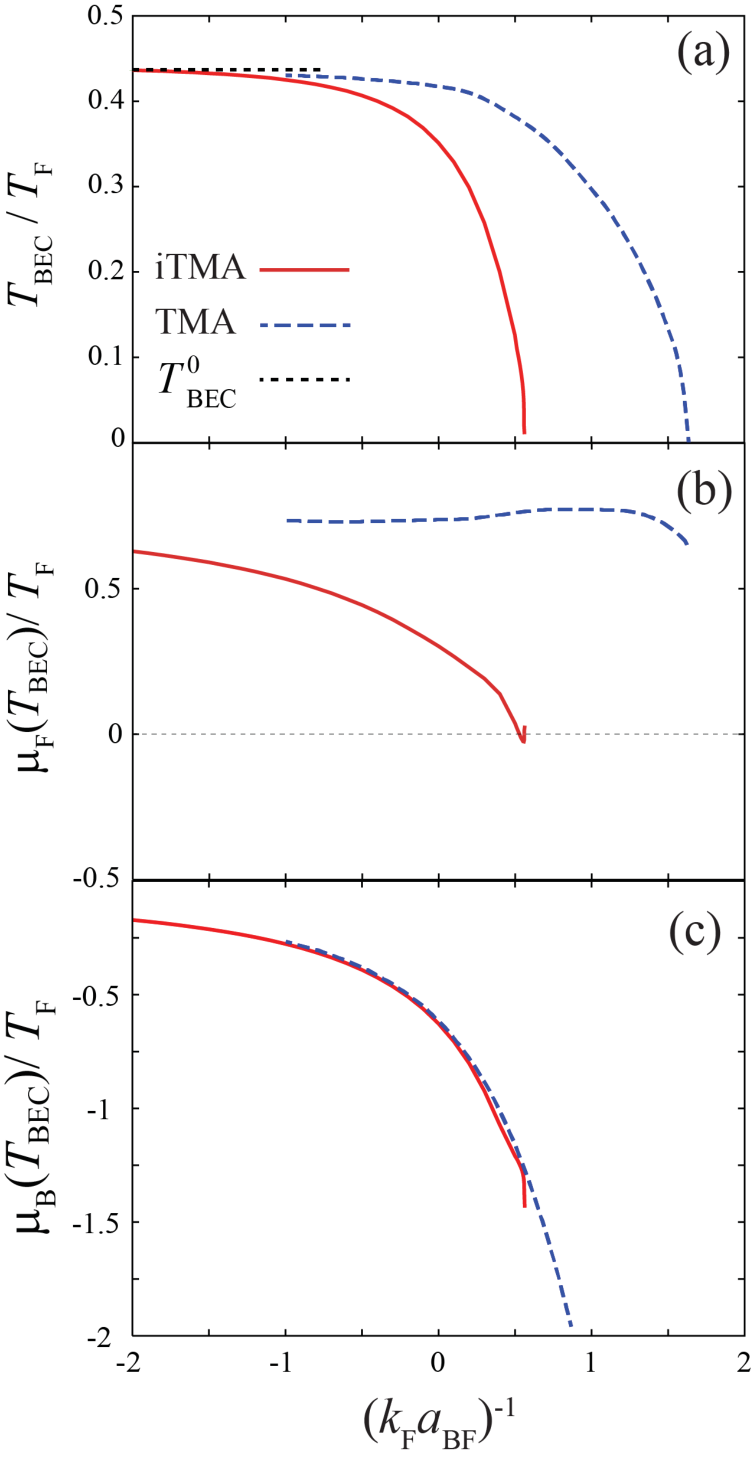

Figure 2.12: iTMA results for (a) $T_{\rm BEC}$,(b) $\mu_{\rm F}(T_{\rm BEC})$, and (c) $\mu_{\rm B}(T_{\rm BEC})$, in a Bose-Fermi mixture. For comparison TMA results are also shown in this figure [44].

In this case, an advantage of iTMA is that the *modified* Bose Green's function $\tilde{G}^0_{\rm B}$ in Eq. (2.64) also consistently satisfied this required at $T_{\rm BEC}$. This enables us to remove the underestimation of effects of low energy Bose excitations (that are nearly gapless) near $T_{\rm BEC}$, in contrast to ordinary in Sec. 2.2.

We briefly note that $\tilde{G}^0_{\rm B}(\boldsymbol{q}-\boldsymbol{p}, i\omega^{\rm F}_m - i\omega^{\rm F}_n)$ in the Fermi self-energy $\tilde{\Sigma}_{\rm F}(\boldsymbol{p}, i\omega^{\rm F}_n)$ in Eq. (2.67) exhibits a singular behavior at $(\boldsymbol{q}, i\omega^{\rm F}_m) = (\boldsymbol{p}, i\omega^{\rm F}_n)$ in numerically evaluating $T_{\rm BEC}$ in iTMA. In Appendix D, we explain how to avoid this singularity in computation [95]. Figure 2.12 (a) shows self-consistent solutions for $T_{\rm BEC}$, $\mu_{\rm F}(T_{\rm BEC})$, as well as $\mu_{\rm B}(T_{\rm BEC})$ in iTMA. Although the overall behavior of $T_{\rm BEC}$ remains unchanged, $T_{\rm BEC}$ is suppressed more considerably, to vanish at $(k_{\rm F}a_{\rm BF})^{-1} \simeq 0.56$, the underestimation of hetero-pairing fluctuations in TMA is corrected in iTMA, by using the Bose Green's function $\tilde{G}^0_{\rm B}$ satisfying the gapless condition in the self-energies. In Fig. 2.12(b), the Fermi atomic chemical potential $\mu_{\rm F}(T_{\rm BEC})$ in iTMA is found to monotonically decrease with increasing interaction strength, to eventually vanish around when $T_{\rm BEC}$ vanishes. This is just the expected behavior of $\mu_{\rm F}$ as one approaches the strong-coupling regime where the formation of composite Fermi molecules occurs. Figure 2.12(c) shows that as the interaction increases the Bose atomic chemical potential $\mu_{\rm B}$ monotonically decreases and almost similar to that in TMA.

Of course, iTMA still has room for improvement, that is, using the fully dressed Green's functions in evaluating the self-energies would give more improved results, which remains as a future problem. However, Fig. 2.12 shows that our iTMA is a minimal strong-coupling theory to correctly describe the Fermi chemical potential in the strong-coupling regime, which the ordinary TMA cannot treat properly. In the following two chapters, we examine the strong-coupling normal state properties of a Bose-Fermi mixture with a tunable inter-species pairing interaction using iTMA.

Chapter 3

Single-particle Properties of a Bose-Fermi Mixture above T_{BEC}

In this chapter, we investigate the single-particle properties of a Bose-Fermi mixture. Including Bose-Fermi hetero-pairing fluctuations within the framework of iTMA discussed in the previous chapter, we calculate the single particle density of states as well as the single particle spectral weight, in both the Bose and Fermi channels above the BEC phase transition temperature T_{BEC}. As shown in Sec. 2.3, strong pairing fluctuations cause a pseudogap phenomenon in the density of states in the BCS-BEC crossover regime of an ultracold Fermi gas. However, we find that such a dip structure is not produced by Bose-Fermi hetero-pairing fluctuations in the intermediate coupling regime around the unitarity ($(k_{\mathrm{F}}a_{\mathrm{BF}})^{-1} = 0$). A shallow dip is only seen in the density of states in the strong-coupling regime. We explain this difference between the Bose-Fermi case and the Fermi-Fermi case from the viewpoint of coupling phenomenon among Fermi atomic excitations, Bose atomic excitations, and Fermi molecular excitations, caused by hetero-pairing fluctuations in the former case. We clarify that this coupling phenomenon strongly reflects detailed spectral structure of the single-particle spectral weight.

3.1 Expressions for Density of States and Spectral Weight in iTMA

In our iTMA, single-particle density of states (DOS) $\rho_{\mathrm{s=B,F}}(\omega)$, as well as the single-particle spectral weight (SW) $A_{\mathrm{s=B,F}}(\boldsymbol{p},\omega)$, can be conveniently evaluated from the analytic continued single-particle dressed Green's function,

$$G_{\mathrm{s}}^{\mathrm{R}}(\boldsymbol{p},\omega) = G_{\mathrm{s}}(\boldsymbol{p}, i\omega_n^{\mathrm{s}} \to \omega + i\delta). \tag{3.1}$$

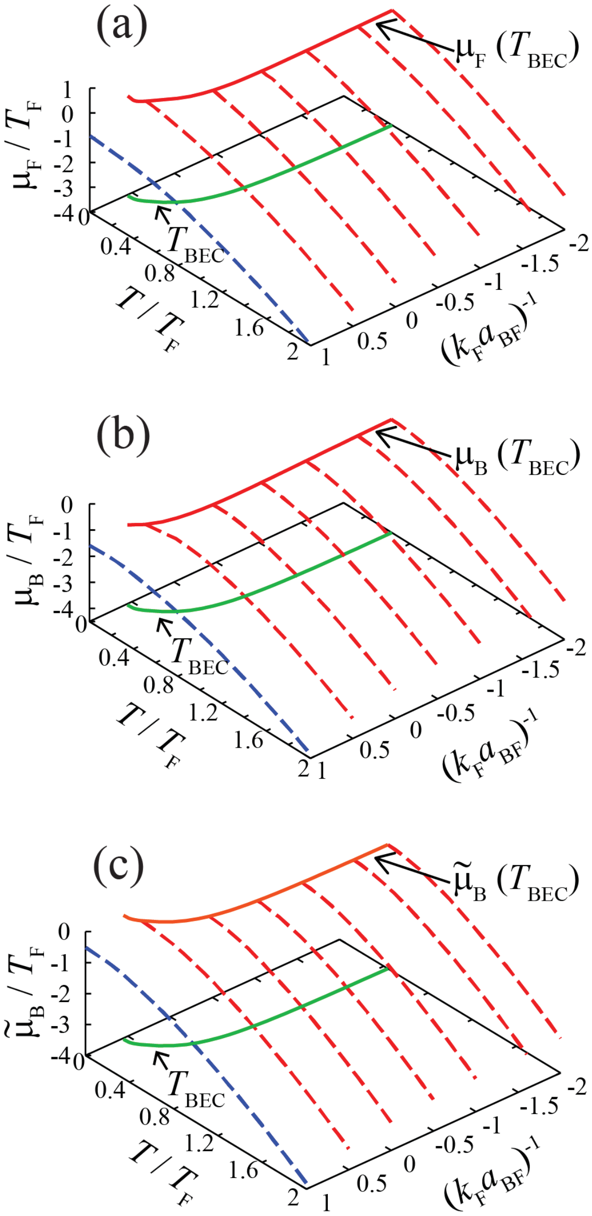

Figure 3.1: Fermi chemical potential $\mu_{\rm F}(T)$ (a), and Bose chemical potential $\mu_{\rm B}(T)$ (b) in the normal state of a Bose-Fermi mixture. Panel (c) shows the effective Bose chemical potential $\tilde{\mu}_{\rm B}(T) = \mu_{\rm B} - \tilde{\Sigma}_{\rm B}(0,0)$. Note that $\tilde{\mu}_{\rm B}(T_{\rm BEC}) = 0$.

As explained in Sec. 2.3 in the case of a two-component Fermi gas, the spectral weight $A_{\rm s}(\boldsymbol{p},\omega)$, as well as the density of states $\rho_{\rm s}(\omega)$ are related to $G^{\rm R}_{\rm s}(\boldsymbol{p},\omega)$ as,

$$\begin{aligned} A_{\rm s}(\boldsymbol{p},\omega) &= -\frac{1}{\pi}{\rm Im}\left[G^{\rm R}_{\rm s}(\boldsymbol{p},\omega)\right] \\ &= -\frac{1}{\pi}\frac{{\rm Im}\tilde{\Sigma}_{\rm s}(\boldsymbol{p}, i\omega^{\rm s}_n \to \omega + i\delta)}{[\omega - \xi^{\rm s}_{\boldsymbol{p}} - {\rm Re}\tilde{\Sigma}_{\rm s}(\boldsymbol{p}, i\omega^{\rm s}_n \to \omega + i\delta)]^2 + [{\rm Im}\tilde{\Sigma}_{\rm s}(\boldsymbol{p}, i\omega^{\rm s}_n \to \omega + i\delta)]^2}, \end{aligned} \tag{3.2}$$

$$
\begin{aligned}
\rho_{\rm s}(\omega) &= -\frac{1}{\pi}\sum_{\boldsymbol{p}} {\rm Im}\left[G_{\rm s}^{\rm R}(\boldsymbol{p},\omega)\right] \\
&= \sum_{\boldsymbol{p}} A_{\rm s}(\boldsymbol{p},\omega). \qquad (3.3)
\end{aligned}
$$

In this thesis, we numerically carry out the analytic continuation in Eq. (3.1) by using Pade's approximation [96].

To evaluate $A_{\rm s}(\boldsymbol{p},\omega)$ and $\rho_{\rm s}(\omega)$ in Eqs. (3.2) and (3.3), we need to determine $\mu_{\rm B}(T)$ and $\mu_{\rm F}(T)$, which is achieved by solving the coupled number equations

$$N_{\rm B} = -T\sum_{\boldsymbol{p},\omega_n^{\rm B}} G_{\rm B}(\boldsymbol{p}, i\omega_n^{\rm B})e^{i\omega_n^{\rm B}\delta}, \qquad (3.4)$$

and

$$N_{\rm F} = T\sum_{\boldsymbol{p},\omega_n^{\rm F}} G_{\rm F}(\boldsymbol{p}, i\omega_n^{\rm F})e^{i\omega_n^{\rm F}\delta}, \qquad (3.5)$$

where $G_{\rm s=B,F}(\boldsymbol{p}, i\omega_n^{\rm s})$ is the dressed Green's function in iTMA given by Eq. (2.70). The BEC phase transition temperature $T_{\rm BEC}$ is determined by solving Eqs. (3.4) and (3.5) together with the gapless condition in Eq. (2.71). The resulting $\mu_{\rm F}(T \geq T_{\rm BEC})$, $\mu_{\rm B}(T \geq T_{\rm BEC})$, as well as the effective Bose chemical potential $\tilde{\mu}_{\rm B}(T \geq T_{\rm BEC}) = \mu_{\rm B} - \tilde{\Sigma}_{\rm B}(\boldsymbol{p} = 0, i\omega_n^{\rm B} = 0)$ (which works as the Bose chemical potential in the modified Bose Green's function in Eq. (2.64)), are summarized in Fig. 3.1. We will use these numerical data in calculating single-particle quantities in Eqs. (3.2) and (3.3).

3.2 Single-particle Density of States $\rho_{\rm s}(\omega)$ at $T_{\rm BEC}$

Figure 3.2 shows the density of states $\rho_{\rm s=B,F}(\omega)$ in a Bose-Fermi mixture at $T_{\rm BEC}$. With increasing the interaction strength, we find in panel (a1) that the lower edge of the Fermi density of states $\rho_{\rm F}(\omega)$ around $\omega = -\varepsilon_{\rm F}$ gradually becomes obscure. However, while $\rho_{\rm F}(\omega)$ exhibits a pseudogap (dip) structure around $\omega = 0$ in the unitarity regime ($(k_{\rm F}a_{\rm FF})^{-1} \sim 0$ see Fig. 2.5) in Fermi-Fermi case, such an anomalous structure is not seen in the present Bose-Fermi case, even in the unitarity limit $(k_{\rm F}a_{\rm BF})^{-1} = 0$. A shallow dip structure only appears in $\rho_{\rm F}(\omega \simeq 0)$ in the strong-coupling side when $(k_{\rm F}a_{\rm BF})^{-1} = 0.5$, as shown in Fig. 3.2(a2). In the strong-coupling limit $(k_{\rm F}a_{\rm BF})^{-1} \to +\infty$, the system is dominated by tightly bound molecular fermions with a large binding energy $E_{\rm bind} = 1/(ma_{\rm BF}^2)$. Since these composite fermions are occupied to the molecular Fermi energy, $E_{\rm F}^{\rm M} = p_{\rm F}^2/(2M)$ $(M = 2m)$ in Eq. (2.47), dissociation energy $\omega = |E_{\rm bind}| - E_{\rm F}^{\rm M}$ (> 0) would be necessary to produce Fermi atomic and Bose atomic excitations. In this sense the shallow but relatively large "pseudogap" structure appearing in the strong-coupling regime in Fig. 3.2(a2) is considered to reflect that the Bose-Fermi mixture gradually transforms to a gas of composite Fermi molecules in this regime ($(k_{\rm F}a_{\rm BF})^{-1} \geq 0$). Apart from this, the absence of a dip structure in a unitary Bose-Fermi mixture indicates that hetero-pairing fluctuations affects the Fermi single-particle excitations in a different manner, compared to the Fermi-Fermi case in BCS-BEC crossover region.

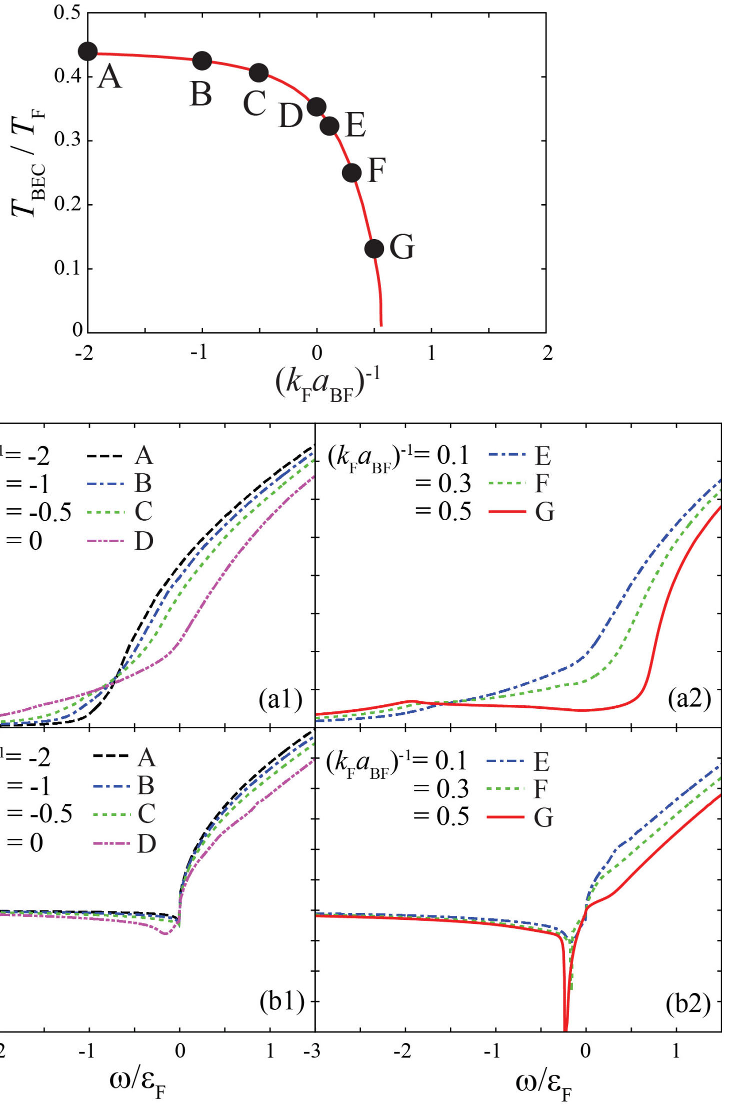

Figure 3.2: Calculated single-particle density of states $\rho_{s=\mathrm{B,F}}(\omega)$ in a Bose-Fermi mixture at T_{BEC}. (a1), (a2) Fermi component $\rho_{\mathrm{F}}(\omega)$. (b1), (b2) Bose component $\rho_{\mathrm{B}}(\omega)$. For clarity we show T_{BEC} at each interaction strength in the uppermost panel.

Figure 3.2(b1) and (b2) shows the Bose density of states $\rho_{\mathrm{B}}(\omega)$ at T_{BEC} in the weak- and strong-coupling side, respectively. As the interaction strength is gradually increased, $\rho_{\mathrm{B}}(\omega)$ is found to be suppressed in the region $\omega/\varepsilon_{\mathrm{F}} > 0$. This tendency is also consistent with the above mentioned molecular picture in the strong-coupling regime, where one indeed needs finite dissociation energy to produce Bose atomic excitations. In the strong-coupling side shown in panel (b2), the negative Bose density of states $\rho_{\mathrm{B}}(\omega)$ in the negative energy region ($\omega < 0$) becomes remarkable, especially just below $\omega = 0$. The high peak structure of $\rho_{\mathrm{B}}(\omega)$ in the negative energy region when $(k_{\mathrm{F}}a_{\mathrm{BF}})^{-1} = 0.5$ implies the existence of strong Bose spectral intensity in the low energy region, which we will examine in the next section.

3.3 Single-particle Spectral Weight $A_{\rm s=B,F}(\boldsymbol{p},\omega)$ at $T_{\rm BEC}$

Since the spectral weight $A_{\rm s}(\boldsymbol{p},\omega)$ may be interpreted as "momentum-resolved" density of states (see Eq. (3.2)), we can obtain more detailed information about strong-coupling corrections to single-particle excitations from $A_{\rm s}(\boldsymbol{p},\omega)$.

Figure 3.3 shows $A_{\rm s=B,F}(\boldsymbol{p},\omega)$ in a Bose-Fermi mixture at $T_{\rm BEC}$. Starting from the non-interacting case (panels (a1) and(b1)), the sharp peak line along the free particle dispersion gradually becomes broad with increasing interaction strength indicating finite lifetime of quasi-particles by the inter-species interaction. At the same time, the spectral intensity below the free particle dispersion gradually grows, to give an additional two peak structure in the strong-coupling regime $(k_{\rm F}a_{\rm BF})^{-1}=0.5$ (a relatively sharp upward peak line and broad downward peak structure). Apart from the details, this tendency is seen in both the Bose ($A_{\rm B}(\boldsymbol{p},\omega)$) and Fermi ($A_{\rm F}(\boldsymbol{p},\omega)$) spectral weight.

To grasp the background physics of Fig. 3.3, it is convenient to rewrite the iTMA Bose-Fermi scattering matrix $\tilde{\Gamma}_{\rm BF}(\boldsymbol{q},i\omega_m^{\rm F})$ in Eq. (2.68) as,

$$\begin{aligned}\tilde{\Gamma}_{\rm BF}(\boldsymbol{q},i\omega_m^{\rm F}) &= \frac{\frac{4\pi a_{\rm BF}}{m}}{1+\frac{4\pi a_{\rm BF}}{m}\left[\tilde{\Pi}_{\rm BF}(\boldsymbol{q},i\omega_m^{\rm F})-\sum_{\boldsymbol{p}}^{p_{\rm c}}\frac{m}{\boldsymbol{p}^2}\right]}\\ &\simeq \frac{\alpha_{\rm BF}}{i\omega_m^{\rm F}-\xi_{\boldsymbol{q}}^{\rm CF}},\end{aligned} \tag{3.6}$$

where

$$\xi_{\boldsymbol{q}}^{\rm CF}=\frac{\boldsymbol{q}^2}{2M}-\mu_{\rm CF} \tag{3.7}$$

may be viewed as the kinetic energy of a composite Fermi molecule, measured from the "molecular chemical potential" $\mu_{\rm CF}$ (where $M=2m$ is the mass of a composite molecule), and $\alpha_{\rm BF}$ is a constant. The expression in Eq. (3.6) is actually valid only in the strong-coupling limit where the molecular dissociation does not occur and in this regime $\alpha_{\rm BF}=8\pi/(m^2a_{\rm BF})>0$ given by Eq. (2.29)(For detailed derivation see Appendix C.1.). However, this simple approximation is very useful in understanding the strong-coupling effects associated with hetero-pairing fluctuations in the strong-coupling regime ($(k_{\rm F}a_{\rm BF})^{-1}\geq 0$). Indeed when we determine the value of $\mu_{\rm CF}$ as the peak energy of the spectrum, $-(1/\pi){\rm Im}\tilde{\Gamma}_{\rm BF}(\boldsymbol{p},i\omega_m^{\rm F}\to\omega+i\delta)$ at $\boldsymbol{p}=0$, the resulting molecular dispersion $\xi_{\boldsymbol{p}}^{\rm CF}$ well describes one of the additional peak structures in $A_{\rm s}(\boldsymbol{p},\omega)$, as shown in Fig 3.3 (a6) and (b6), implying that the approximate expression in Eq. (3.6) really contributes to the spectral weight $A_{\rm s}(\boldsymbol{p},\omega)$, at least in the strong-coupling regime.

Substituting Eq. (3.6) into Eqs. (2.66) and (2.67) and after summing up the fermion Matsubara frequencies $\omega_m^{\rm F}$ we obtain,

$$\tilde{\Sigma}_{\rm B}(\boldsymbol{p},i\omega_n^{\rm B})=\alpha_{\rm BF}\sum_{\boldsymbol{q}}\left[\frac{n_{\rm F}(\xi_{\boldsymbol{q}}^{\rm F})}{i\omega_n^{\rm B}-\xi_{\boldsymbol{p}-\boldsymbol{q}}^{\rm CF}+\xi_{\boldsymbol{q}}^{\rm F}}-\frac{n_{\rm F}(\xi_{\boldsymbol{q}}^{\rm CF})}{i\omega_n^{\rm B}+\xi_{\boldsymbol{p}-\boldsymbol{q}}^{\rm F}-\xi_{\boldsymbol{q}}^{\rm CF}}\right], \tag{3.8}$$

$$\tilde{\Sigma}_{\rm F}(\boldsymbol{p},i\omega_n^{\rm F})=\alpha_{\rm BF}\sum_{\boldsymbol{q}}\left[\frac{n_{\rm B}(\tilde{\xi}_{\boldsymbol{q}}^{\rm B})}{i\omega_n^{\rm F}-\xi_{\boldsymbol{p}-\boldsymbol{q}}^{\rm CF}+\tilde{\xi}_{\boldsymbol{q}}^{\rm B}}+\frac{n_{\rm F}(\xi_{\boldsymbol{q}}^{\rm CF})}{i\omega_n^{\rm F}+\tilde{\xi}_{\boldsymbol{p}-\boldsymbol{q}}^{\rm B}-\xi_{\boldsymbol{q}}^{\rm CF}}\right]. \tag{3.9}$$

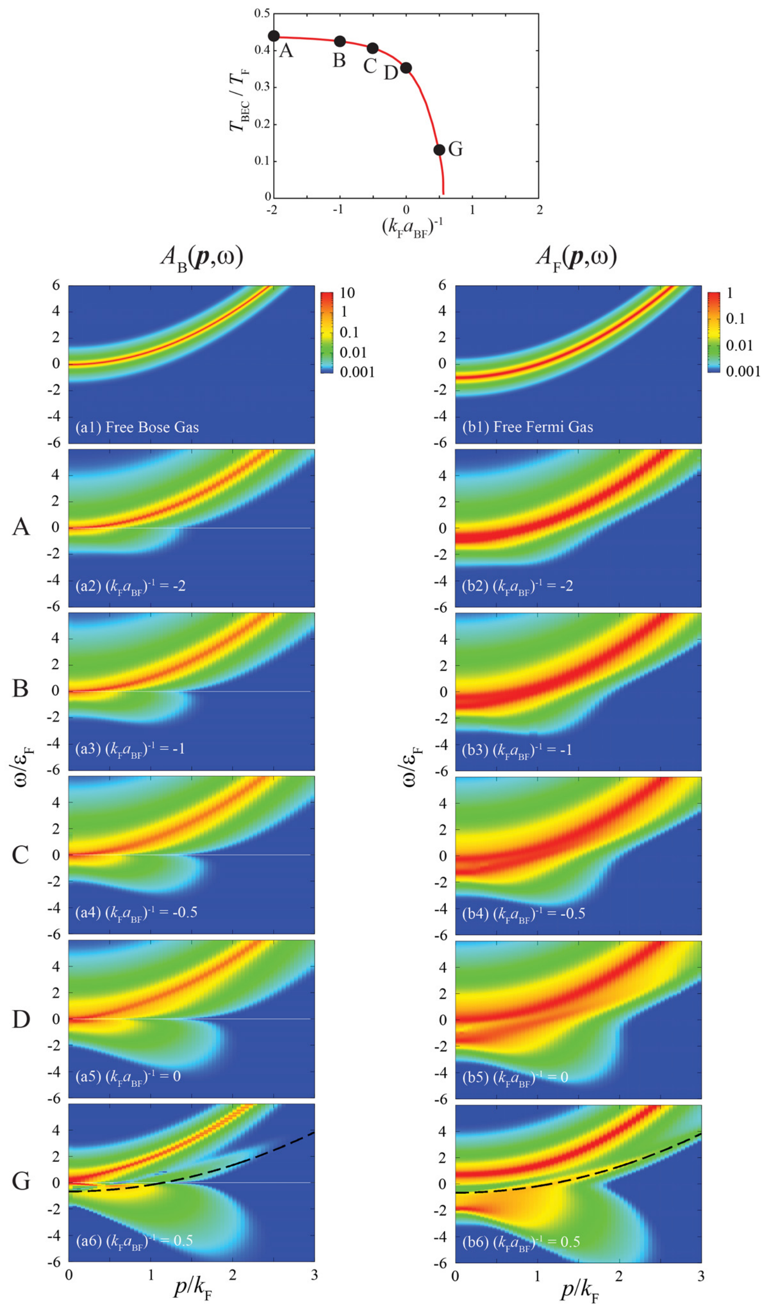

Figure 3.3: Calculated intensity of single-particle spectral weight at $T_{\rm BEC}$ normalized by $\varepsilon_{\rm F}^{-1}$ (where, $\varepsilon_{\rm F}$ is the atomic Fermi energy). (a1)-(a6) $A_{\rm B}(\boldsymbol{p},\omega)$. (b1)-(b6) $A_{\rm F}(\boldsymbol{p},\omega)$. The Bose spectral weight $A_{\rm B}(\boldsymbol{p},\omega)$ is negative when $\omega<0$, so that we plot $\mathrm{sgn}(\omega)\times A_{\rm B}(\boldsymbol{p},\omega)$ in the left panels. The dashed lines in panel (a6) and (b6) shows the molecular dispersion $\omega=\boldsymbol{p}^2/(2M)-\mu_{\rm CF}$, where $M=2m$ is a molecular mass. The Fermi molecular chemical potential $\mu_{\rm CF}$ is determined as the peak energy of the spectrum, $-(1/\pi)\mathrm{Im}[\tilde{\Gamma}_{\rm BF}(\boldsymbol{p}=0,i\omega_n^{\rm F}\to\omega+i\delta)]$. For clarity, we show $T_{\rm BEC}$ in the cases of (a2)∼(a6) and (b2)∼(b6) in the uppermost panel "A∼D and G". The spectral weight at "G" is separately shown in Fig. 3.4.

To further simplify Eqs. (3.8) and (3.9), we note that the Bose distribution function $n_{\rm B}(\tilde{\xi}_{\boldsymbol{q}}^{\rm B})$ becomes very large around $\boldsymbol{q}=0$ near $T_{\rm BEC}$ because of the gapless condition at $T_{\rm BEC}$. In addition, when we consider the strong-coupling regime at $(k_{\rm F}a_{\rm BF})^{-1}=0.5$ shown in Figs. 3.3(a6) and (b6), one finds that $\mu_{\rm F}(T_{\rm BEC})/\varepsilon_{\rm F}\ll 1$ (see Fig. 2.12(b)). Using these, we can approximately set $\boldsymbol{q}=0$ in the denominator of the first term in each Eqs. (3.8) and (3.9), as well as ignore the Fermi chemical potential $\mu_{\rm F}$ there. In addition, when composite Fermi molecules form the Fermi surface, one may approximate the momentum $\boldsymbol{q}$ in the denominator of the second terms in Eq. (3.8) and (3.9) to an "effective Fermi momentum" $\tilde{\boldsymbol{p}}_{\rm F}^{\rm CF}$ of molecular fermions, where $|\tilde{\boldsymbol{p}}_{\rm F}^{\rm CF}|=\sqrt{2M\mu_{\rm CF}}$. These approximations give

$$\tilde{\Sigma}_{\rm B}(\boldsymbol{p},i\omega_n^{\rm B})=\frac{\lambda_{\rm F}}{i\omega_n^{\rm B}-\xi_{\boldsymbol{p}}^{\rm CF}}-\left\langle\frac{\lambda_{\rm CF}}{i\omega_n^{\rm B}+\xi^{\rm F}_{\boldsymbol{p}-\tilde{\boldsymbol{p}}_{\rm F}^{\rm CF}}}\right\rangle, \tag{3.10}$$

$$\tilde{\Sigma}_{\rm F}(\boldsymbol{p},i\omega_n^{\rm F})=\frac{\lambda_{\rm B}}{i\omega_n^{\rm F}-\xi_{\boldsymbol{p}}^{\rm CF}}+\left\langle\frac{\lambda_{\rm CF}}{i\omega_n^{\rm F}+\tilde{\xi}^{\rm B}_{\boldsymbol{p}-\tilde{\boldsymbol{p}}_{\rm F}^{\rm CF}}}\right\rangle, \tag{3.11}$$

where

$$\lambda_{\rm B}=\alpha_{\rm BF}N_{\rm B}^0,\qquad \Big(N_{\rm B}^0=\sum_{\boldsymbol{p}}n_{\rm B}(\tilde{\xi}_{\boldsymbol{p}}^{\rm B})\Big), \tag{3.12}$$

$$\lambda_{\rm F}=\alpha_{\rm BF}N_{\rm F}^0,\qquad \Big(N_{\rm F}^0=\sum_{\boldsymbol{p}}n_{\rm F}(\xi_{\boldsymbol{p}}^{\rm F})\Big), \tag{3.13}$$

$$\lambda_{\rm CF}=\alpha_{\rm BF}N_{\rm CF}^0,\qquad \Big(N_{\rm CF}^0=\sum_{\boldsymbol{p}}n_{\rm F}(\xi_{\boldsymbol{p}}^{\rm CF})\Big), \tag{3.14}$$

and the average $\langle\cdots\rangle$ is taken over the direction of the molecular Fermi momentum $\tilde{\boldsymbol{p}}_{\rm F}^{\rm CF}$. Substituting Eqs. (3.10) and (3.11) into the iTMA Green's function in Eq. (2.70), we obtain, after taking analytic continuation ($i\omega_n^{\rm s}\to\omega+i\delta$),

$$G_{\rm B}^{\rm R}(\boldsymbol{p},\omega)\simeq\frac{1}{\omega-\xi_{\boldsymbol{p}}^{\rm B}-\dfrac{\lambda_{\rm F}}{\omega-\xi_{\boldsymbol{p}}^{\rm CF}}+\left\langle\dfrac{\lambda_{\rm CF}}{\omega+\xi^{\rm F}_{\boldsymbol{p}-\tilde{\boldsymbol{p}}_{\rm F}^{\rm CF}}}\right\rangle}, \tag{3.15}$$

$$G_{\rm F}^{\rm R}(\boldsymbol{p},\omega)\simeq\frac{1}{\omega-\xi_{\boldsymbol{p}}^{\rm F}-\dfrac{\lambda_{\rm B}}{\omega-\xi_{\boldsymbol{p}}^{\rm CF}}-\left\langle\dfrac{\lambda_{\rm CF}}{\omega+\tilde{\xi}^{\rm B}_{\boldsymbol{p}-\tilde{\boldsymbol{p}}_{\rm F}^{\rm CF}}}\right\rangle}. \tag{3.16}$$

Equation (3.15) and (3.16) clearly indicate that hetero-pairing fluctuations cause a coupling phenomenon among Fermi atomic excitations ($\xi_{\boldsymbol{p}}^{\rm F}$), Bose atomic excitations ($\tilde{\xi}_{\boldsymbol{p}}^{\rm B}$), and Fermi molecular excitations ($\xi_{\boldsymbol{p}}^{\rm CF}$), with the coupling constants $\lambda_{\rm s=B,F,CF}$ in Eqs. (3.12)-(3.14) [97]. This explains the appearance of the spectral peak along the Fermi molecular dispersion, $\omega=\xi_{\boldsymbol{p}}^{\rm CF}=\boldsymbol{p}^2/(2M)-\mu_{\rm CF}$, in Figs. 3.3(a6) and (b6) (dashed lines).

On the other hand, $\lambda_{\rm CF}$ in Eq. (3.15) brings about coupling between Bose atomic excitations ($\omega=\xi_{\boldsymbol{p}}^{\rm B}$) and Fermi hole excitations ($\omega=-\xi^{\rm F}_{\boldsymbol{p}-\tilde{\boldsymbol{p}}_{\rm F}^{\rm CF}}$). In this regard, because of the average over the direction of $\tilde{\boldsymbol{p}}_{\rm F}^{\rm CF}$ in Eq. (3.15), the contribution from the hole excitations gives a broad spectral structure in $A_{\rm B}(\boldsymbol{p},\omega)$ such that,

$$-\frac{(p+\tilde{p}_{\rm F}^{\rm CF})^2}{2m} \leq \omega \leq -\frac{(p-\tilde{p}_{\rm F}^{\rm CF})^2}{2m}. \tag{3.17}$$

Here we are considering the strong-coupling case in Figs. 3.3(a6) so that we have ignored $\mu_{\rm F}$, as $\mu_{\rm F} \ll \varepsilon_{\rm F}$. Such a broad spectral structure in $A_{\rm B}(\boldsymbol{p},\omega)$ is indeed seen in the negative energy region in Fig. 3.3(a6). We point out that this contribution as well as the molecular contribution around $\boldsymbol{p}=0$ (where $\xi_{\boldsymbol{p}}^{\rm CF}<0$), also explain the negative Bose density of states ($\rho_{\rm B}(\omega<0)$) with the negative peak structure seen in Fig. 3.2(b2), when $(k_{\rm F}a_{\rm BF})^{-1}=0.5$.

The last term of the denominator in the Fermi Green's function in Eq. (3.16) also contains the average over the direction $\tilde{\boldsymbol{p}}_{\rm F}^{\rm CF}$. This also explains the broad downward spectral structure in the negative energy region of the Fermi spectral weight $A_{\rm F}(\boldsymbol{p},\omega)$ in Fig. 3.3(b6).

At a glance, this spectral intensity and the spectral structure in the positive energy region coming from the ordinary Fermi particle dispersion $\omega=\xi_{\boldsymbol{p}}^{\rm F}$ may appear to give a pseudogap structure in the density of states $\rho_{\rm F}(\omega)$ around $\omega=0$, as in the case of a two-component Fermi gas (where strong-coupling effects results into pseudogap phenomenon due to particle-hole coupling near the Fermi surface). However, the above-mentioned Fermi molecular dispersion, which passes through $\omega=0$, increases the Fermi density of states $\rho_{\rm F}(\omega)$ around $\omega=0$, so that $\rho_{\rm F}(\omega)$ actually does not exhibit such a dip structure in the unitarity limit ($(k_{\rm F}a_{\rm BF})^{-1}=0$), as shown in Fig. 3.2(a1). Because of the same reason, although a dip structure appears in $\rho_{\rm F}(\omega\sim 0)$ when $(k_{\rm F}a_{\rm BF})^{-1}=0.5$ (see Fig. 3.2(a2)), it is very shallow.

Figure 3.4 shows the interaction strength $(k_{\rm F}a_{\rm BF})^{-1}$ dependence of spectral weight $A_{\rm s=B,F}(\boldsymbol{p},\omega)$ at a finite momentum $\boldsymbol{p}=1.5k_{\rm F}$ corresponding to the Fig. 3.3. In Fig. 3.4(a) and (b) one can clearly see a sharp peak corresponding to the free-particle dispersion $\omega>0$. Furthermore, one can also see that as the interaction strength increases, two more peak structures corresponding to the composite fermion dispersion $\omega>0$ and broad Fermi hole (Bose) atomic dispersion $\omega<0$ are formed corresponding to Bose (Fermi) spectral weight $A_{\rm s=B,F}(\boldsymbol{p},\omega)$, shown in the inset of Fig. 3.4(a) and (b), respectively. (Note that in Fermi spectral weight $A_{\rm F}(\boldsymbol{p},\omega)$ composite fermion peak exists at unitarity, consistent with Fig. 3.3(b5).)

Figure 3.5 shows the spectral weight $A_{\rm s=B,F}(\boldsymbol{p},\omega)$ at $T\approx 0$ when $(k_{\rm F}a_{\rm BF})^{-1}=1$. In this figure, the spectral peak along the molecular $\omega=\xi_{\boldsymbol{p}}^{\rm CF}$ is invisible, in contrast to the case at $(k_{\rm F}a_{\rm BF})^{-1}=0.5$ in Fig. 3.3(a6) and (b6). As a result, we see a clear gap-like structure around $\omega=0$ in each Bose and Fermi spectral weight in Fig. 3.5. We note that the BEC phase transition vanishes in the strong-coupling regime when $(k_{\rm F}a_{\rm BF})^{-1}\geq 0.56$ (see Fig. 2.12(a)). In addition, when $(k_{\rm F}a_{\rm BF})^{-1}=1$, the Fermi chemical potential $\mu_{\rm F}$, as well as the effective Bose chemical potential $\tilde{\mu}_{\rm B}=\mu_{\rm B}-\Sigma_{\rm B}(0,0)$, are negative (see Fig. 3.1). Thus, in the case of Fig. 3.5 ($(k_{\rm F}a_{\rm BF})^{-1}=1$ and $T/T_{\rm F}=0.0036\ll 1$), the Fermi distribution function $n_{\rm F}(\xi_{\boldsymbol{p}}^{\rm F})=n_{\rm F}(\varepsilon_{\boldsymbol{p}}+|\mu_{\rm F}|)$ in Eq. (3.8) as well the Bose distribution function $n_{\rm B}(\tilde{\xi}_{\boldsymbol{p}}^{\rm B})=n_{\rm B}(\varepsilon_{\boldsymbol{p}}+|\tilde{\mu}_{\rm B}|)$ in Eq. (3.9), can be safely ignored, which gives Eqs. (3.15) and (3.16) with $\lambda_{\rm F}=\lambda_{\rm B}=0$,

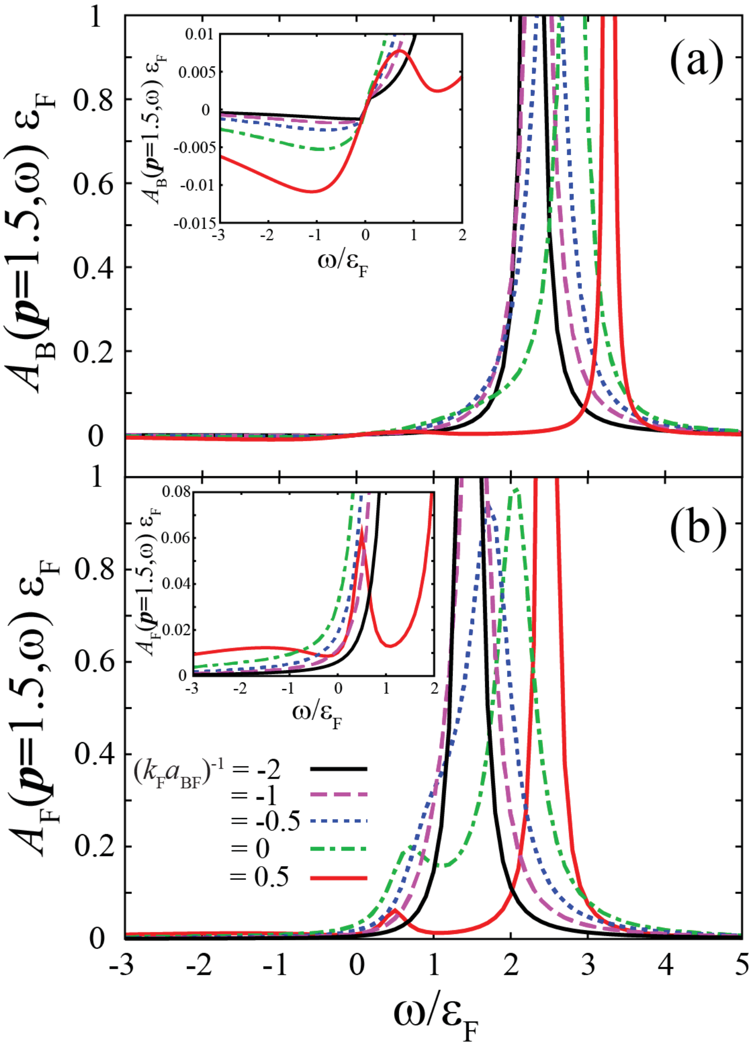

Figure 3.4: Single-particle spectral weight at $\boldsymbol{p} = 1.5k_{\mathrm{F}}$, as a function of energy ω. We take $(k_{\mathrm{F}}a_{\mathrm{BF}})^{-1} = 0.5$. (a) Bose component. (b) Fermi component.

that is,

$$G^{\mathrm{R}}_{\mathrm{B}}(\boldsymbol{p},\omega) \simeq \frac{1}{\omega - \xi^{\mathrm{B}}_{\boldsymbol{p}} + \left\langle \dfrac{\lambda_{\mathrm{CF}}}{\omega + \xi^{\mathrm{F}}_{\boldsymbol{p}-\tilde{\boldsymbol{p}}^{\mathrm{CF}}_{\mathrm{F}}}} \right\rangle}, \tag{3.18}$$

$$G^{\mathrm{R}}_{\mathrm{F}}(\boldsymbol{p},\omega) \simeq \frac{1}{\omega - \xi^{\mathrm{F}}_{\boldsymbol{p}} - \left\langle \dfrac{\lambda_{\mathrm{CF}}}{\omega + \tilde{\xi}^{\mathrm{B}}_{\boldsymbol{p}-\tilde{\boldsymbol{p}}^{\mathrm{CF}}_{\mathrm{F}}}} \right\rangle}. \tag{3.19}$$

This expression immediately explains the vanishing molecular spectral peak in Fig. 3.5. On the other hand, because the molecular fermions form a Fermi surface in the strong-coupling regime, the molecular chemical potential μ_{CF} is positive in the case of Fig. 3.5. Thus, the coupling constant $\lambda_{\mathrm{CF}} = \alpha_{\mathrm{BF}}n_{\mathrm{F}}(\xi^{\mathrm{CF}}_{\boldsymbol{p}})$ does *not* vanish, leading

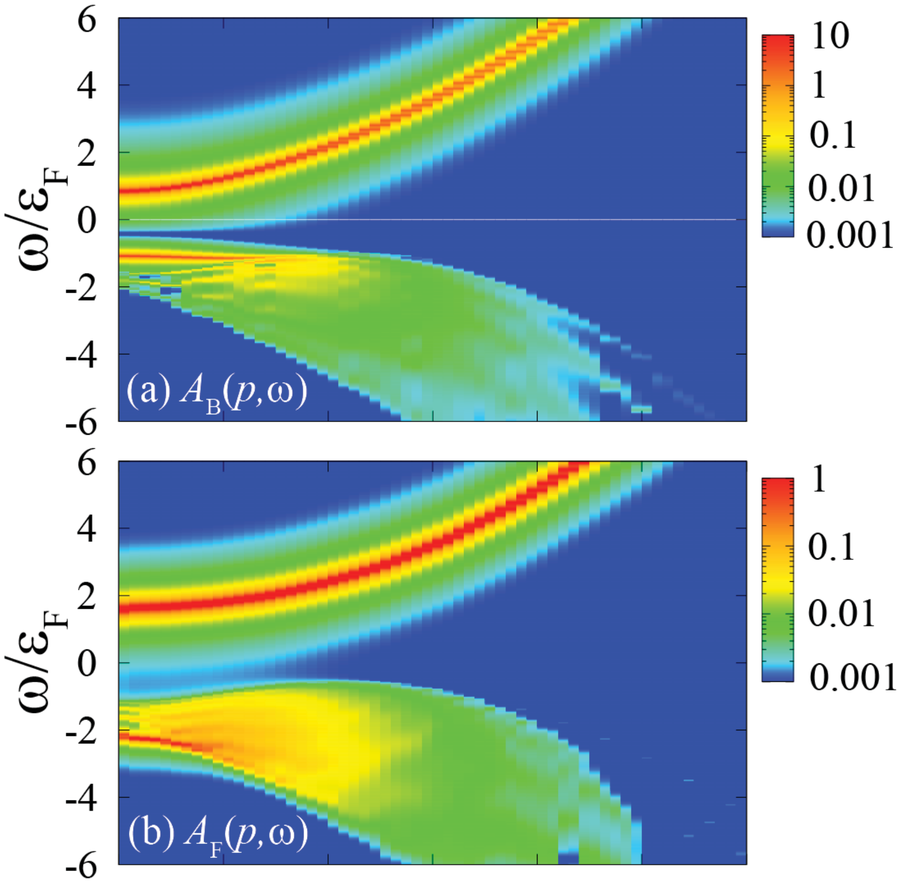

Figure 3.5: Intensity of singe-particle spectral weight in the strong-coupling regime, when $(k_{\rm F}a_{\rm BF})^{-1} = 1$ and $T/T_{\rm F} = 0.0036$. (a) Bose component $A_{\rm B}(\boldsymbol{p}, \omega)$. (b) Fermi component $A_{\rm F}(\boldsymbol{p}, \omega)$. The intensity is normalized by $\varepsilon_{\rm F}^{-1}$.

to the non-vanishing spectral structure in the negative energy region of the spectral weight there.

Estimating the (pseudo)gap energy $\omega_{\rm gap}^{\rm B}$ in the Bose spectral weight $A_{\rm B}(\boldsymbol{p}, \omega)$, as well as the gap energy $\omega_{\rm gap}^{\rm F}$ in the Fermi spectral weight $A_{\rm F}(\boldsymbol{p}, \omega)$, from the peak-to-peak energy at $\boldsymbol{p} = 0$ in Figs. 3.5 (a) and (b), respectively, and we find that their magnitudes are different as,

$$\begin{cases} \omega_{\rm gap}^{\rm B} = 1.9\varepsilon_{\rm F}, \\ \omega_{\rm gap}^{\rm F} = 3.7\varepsilon_{\rm F}, \end{cases} \tag{3.20}$$

although they both originate from the dissociation of a Bose-Fermi molecule.

To explain the reason for this difference in a simple manner, the approximate Green's functions in Eqs. (3.18) and (3.19) are helpful. We obtain the two bosonic eigen-energies $\omega_{\pm}^{\rm B}$ at $\boldsymbol{p} = 0$ from the pole of the Green's function

$$\omega = \xi_{\boldsymbol{p}=0}^{\rm B} - \frac{\lambda_{\rm CF}}{\omega + \xi_{\tilde{\boldsymbol{p}}_{\rm F}^{\rm CF}}^{\rm F}}, \tag{3.21}$$

which gives

$$\omega_\pm^{\rm B}=\frac{1}{2}\left[[|\mu_{\rm B}|-|\mu_{\rm F}|-\varepsilon_{\tilde{\boldsymbol{p}}_{\rm F}^{\rm CF}}]\pm\sqrt{(|\mu_{\rm B}|+|\mu_{\rm F}|+\varepsilon_{\tilde{\boldsymbol{p}}_{\rm F}^{\rm CF}})^2-4\lambda_{\rm CF}}\right]. \tag{3.22}$$

In the same manner, the pole equation of the Green's function in Eq.(3.19)

$$\omega=\xi_{\boldsymbol{p}=0}^{\rm F}+\frac{\lambda_{\rm CF}}{\omega+\xi_{\tilde{\boldsymbol{p}}_{\rm F}^{\rm CF}}^{\rm B}} \tag{3.23}$$

gives the two fermionic eigen-energies $\omega_\pm^{\rm F}$ at $\boldsymbol{p}=0$,

$$\omega_\pm^{\rm F}=\frac{1}{2}\left[[|\mu_{\rm F}|-|\tilde{\mu}_{\rm B}|-\varepsilon_{\tilde{\boldsymbol{p}}_{\rm F}^{\rm CF}}]\pm\sqrt{(|\tilde{\mu}_{\rm B}|+|\mu_{\rm F}|+\varepsilon_{\tilde{\boldsymbol{p}}_{\rm F}^{\rm CF}})^2+4\lambda_{\rm CF}}\right]. \tag{3.24}$$

Using these results, one obtains the bosonic energy gap $\omega_{\rm gap}^{\rm B}=\omega_+^{\rm B}-\omega_-^{\rm B}$, and the fermionic energy gap $\omega_{\rm gap}^{\rm F}=\omega_+^{\rm F}-\omega_-^{\rm F}$ as, respectively,

$$\begin{cases}\omega_{\rm gap}^{\rm B}=\sqrt{(|\mu_{\rm B}|+|\mu_{\rm F}|+\varepsilon_{\tilde{\boldsymbol{p}}_{\rm F}^{\rm CF}})^2-4\lambda_{\rm CF}},\\ \omega_{\rm gap}^{\rm F}=\sqrt{(|\tilde{\mu}_{\rm B}|+|\mu_{\rm F}|+\varepsilon_{\tilde{\boldsymbol{p}}_{\rm F}^{\rm CF}})^2+4\lambda_{\rm CF}}.\end{cases} \tag{3.25}$$

To estimate Eqs. (3.25) in the case of Fig. 3.5, we simply employ the strong-coupling expression $\alpha_{\rm BF}=8\pi/(m^2a_{\rm BF})$ in $\lambda_{\rm CF}=\alpha_{\rm BF}N_{\rm CF}^0$, and assume that all the atoms form Fermi molecules ($N_{\rm CF}^0\simeq N_{\rm F}$). Substituting the iTMA values,

$$\begin{cases}\mu_{\rm F}=-0.92\varepsilon_{\rm F},\\ \mu_{\rm B}=-1.59\varepsilon_{\rm F},\\ \tilde{\mu}_{\rm B}=-0.51\varepsilon_{\rm F},\end{cases} \tag{3.26}$$

into Eq. (3.25), we obtain

$$\begin{cases}\omega_{\rm gap}^{\rm B}=2.35\varepsilon_{\rm F},\\ \omega_{\rm gap}^{\rm F}=3.56\varepsilon_{\rm F}.\end{cases} \tag{3.27}$$

This rough estimation gives comparable gap sizes to Eq. (3.20).

Deep inside the strong-coupling regime ($(k_{\rm F}a_{\rm BF})^{-1}\gg 1$), the value of $|\mu_{\rm F}|+|\mu_{\rm B}|$ would approach the binding energy $E_{\rm bind}=1/(ma_{\rm BF}^2)$ ($\gg\varepsilon_{\rm F}$) of a tightly bound molecule (Eq. (2.49)). In this extreme case, one may safely ignore other terms in Eq. (3.25), which gives

$$\omega_{\rm gap}^{\rm B}=\omega_{\rm gap}^{\rm F}=E_{\rm bind}, \tag{3.28}$$

as expected.

Now we compare our results for a Bose-Fermi mixture with those in case of a two-component Fermi gas. In the latter, following the same procedure as in the case of Bose-Fermi mixture, we approximate the particle-particle scattering matrix $\Gamma_{\rm FF}(\boldsymbol{q},i\omega_m^{\rm B})$ in Eq. (2.23) to the Cooper-pair propagator,

$$\Gamma_{\rm FF}(\boldsymbol{q},i\omega_m^{\rm B})=\frac{\alpha_{\rm FF}}{i\omega_m^{\rm B}-\xi_{\boldsymbol{q}}^{\rm CB}}. \tag{3.29}$$

Here,

$$\xi_{\boldsymbol{q}}^{\rm CB} = \frac{\boldsymbol{q}^2}{(2M)} - \mu_{\rm CB}, \tag{3.30}$$

is the kinetic energy of a Cooper pair, where $M = 2m$ is the molecular mass and $\mu_{\rm CB}$ is the chemical potential. The factor $\alpha_{\rm FF} = 8\pi/(m^2 a_{\rm FF})$ in the strong-coupling BEC limit [52], where $a_{\rm FF}$ is the s-wave scattering length in terms of a contact-type interaction $-U_{\rm FF}$ between Fermi atoms. Using Eq. (3.29) we have the approximate self-energy, given by

$$\Sigma_{\rm F}(\boldsymbol{p}, i\omega_n^{\rm F}) = \alpha_{\rm FF} \sum_{\boldsymbol{q}} \left[\frac{n_{\rm B}(\xi_{\boldsymbol{q}}^{\rm CB})}{i\omega_n^{\rm F} + \xi_{\boldsymbol{p}-\boldsymbol{q}}^{\rm F} - \xi_{\boldsymbol{q}}^{\rm CB}} + \frac{n_{\rm F}(\xi_{\boldsymbol{q}}^{\rm F})}{i\omega_n^{\rm F} + \xi_{\boldsymbol{q}}^{\rm F} - \xi_{\boldsymbol{p}-\boldsymbol{q}}^{\rm CB}} \right]. \tag{3.31}$$

At the superfluid phase transition temperature $T_{\rm c}$, the Cooper-pair chemical potential $\mu_{\rm CB}$ vanishes, according to the Thouless criterion [92], which leads to the divergence of the Bose distribution function $n_{\rm B}(\xi_{\boldsymbol{q}}^{\rm CB})$ at $\boldsymbol{q} = 0$. Noting this, we approximately set $\boldsymbol{q} = 0$ in the denominator of the first term in Eq. (3.31). For the second term in Eq. (3.31), we approximately replace $\boldsymbol{q}$ by the "effective Fermi momentum" $\tilde{\boldsymbol{p}}_{\rm F}$ of Fermi atoms, in the denominator where $|\tilde{\boldsymbol{p}}_{\rm F}| = \sqrt{2m\mu_{\rm F}}$. (We consider the unitary regime, where the Fermi chemical potential is still positive, see Fig 2.3.) Using these approximations, Eq. (3.31) reduces to

$$\Sigma_{\rm F}(\boldsymbol{p}, i\omega_n^{\rm F}) = \frac{\lambda_{\rm CB}}{i\omega_n^{\rm F} + \xi_{\boldsymbol{p}}^{\rm F}} + \left\langle \frac{\lambda_{\rm F}}{i\omega_n^{\rm F} - \xi_{\boldsymbol{p}-\tilde{\boldsymbol{p}}_{\rm F}}^{\rm CB}} \right\rangle, \tag{3.32}$$

and the TMA single-particle Fermi Green's function with this approximate self-energy in Eq. (3.32) has the form,

$$G_{\rm F}^{\rm R}(\boldsymbol{p}, \omega) \simeq \frac{1}{\omega - \xi_{\boldsymbol{p}}^{\rm F} - \dfrac{\lambda_{\rm CB}}{\omega + \xi_{\boldsymbol{p}}^{\rm F}} - \left\langle \dfrac{\lambda_{\rm F}}{\omega - \xi_{\boldsymbol{p}-\tilde{\boldsymbol{p}}_{\rm F}}^{\rm CB}} \right\rangle}. \tag{3.33}$$

Equation (3.33) shows that bosonic pairing fluctuations $\Gamma_{\rm FF}$ couple Fermi atomic dispersion ($\omega = \xi_{\boldsymbol{p}}^{\rm F}$) with the hole dispersion ($\omega = -\xi_{\boldsymbol{p}}^{\rm F}$) with the coupling constant $\lambda_{\rm CB} = \alpha_{\rm FF} \sum_{\boldsymbol{q}} n_{\rm B}(\xi_{\boldsymbol{q}}^{\rm CB})$. When we only retain this effect, Eq. (3.33) reproduces the "pseudo-gapped" Green's function in Eq. (2.42), where $\lambda_{\rm CB}$ (> 0) plays the role as the square of the pseudogap parameter $\Delta_{\rm pg}$ in Eq. (3.33). In a Bose-Fermi mixture, the corresponding coupling phenomenon is brought about by Bose atomic excitations, being characterized by $\lambda_{\rm B}$ in Eq. (3.16). However, what is coupled with the Fermi atomic dispersion by $\lambda_{\rm B}$ is the Fermi molecular dispersion ($\omega = \xi_{\boldsymbol{p}}^{\rm CF} = \boldsymbol{p}^2/(2M) - \mu_{\rm CF}$), passing through $\omega = 0$. Thus, although the particle-hole coupling phenomenon in a two-component Fermi gas suppresses the single-particle density of states $\rho_{\rm F}(\omega \sim 0)$ (pseudogap phenomenon), the Fermi-molecule coupling in a Bose Fermi mixture enhances $\rho_{\rm F}(\omega \sim 0)$.

The last term in the denominator in Eq. (3.33) corresponds similar to that in Eq. (3.16). However, while the latter gives a broad spectral structure in the *negative*

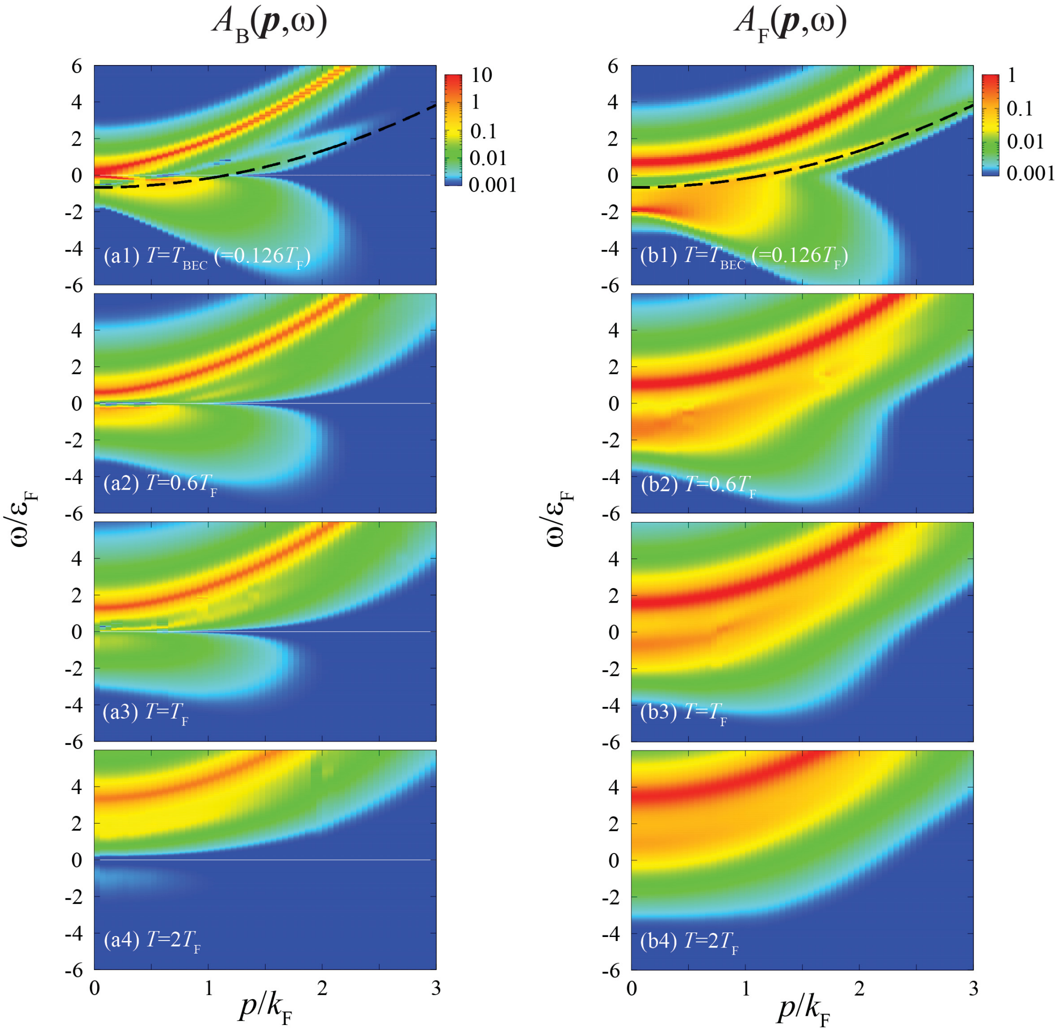

Figure 3.6: Intensity of single-particle spectral weight above $T_{\rm BEC}$. (a1)∼(a4) $A_{\rm B}(\boldsymbol{p},\omega)$. (b1)∼(b3) $A_{\rm F}(\boldsymbol{p},\omega)$. We take $(k_{\rm F}a_{\rm BF})^{-1}=0.5$.

energy region of the spectral weight (see Fig. 3.3(b6)), the former in the Fermi-Fermi case induces a spectral structure in the *positive* energy region around

$$\frac{(p-\tilde{p}_{\rm F})^2}{2M}\le\omega\le\frac{(p+\tilde{p}_{\rm F})^2}{2M}\quad(T=T_{\rm c}). \tag{3.34}$$

This broad spectral structure has not been so frequently discussed in cold Fermi gas physics, because the spectral intensity in the positive energy region is usually dominated by the strong peak intensity along the Fermi particle dispersion ($\omega=\xi^{\rm F}_{\boldsymbol{p}}$). However, it has been pointed out [98] that this particle dispersion becomes broad, when it is in the region in Eq. (3.34), because of the coupling phenomenon described by $\lambda_{\rm F}$ in Eq. (3.33).

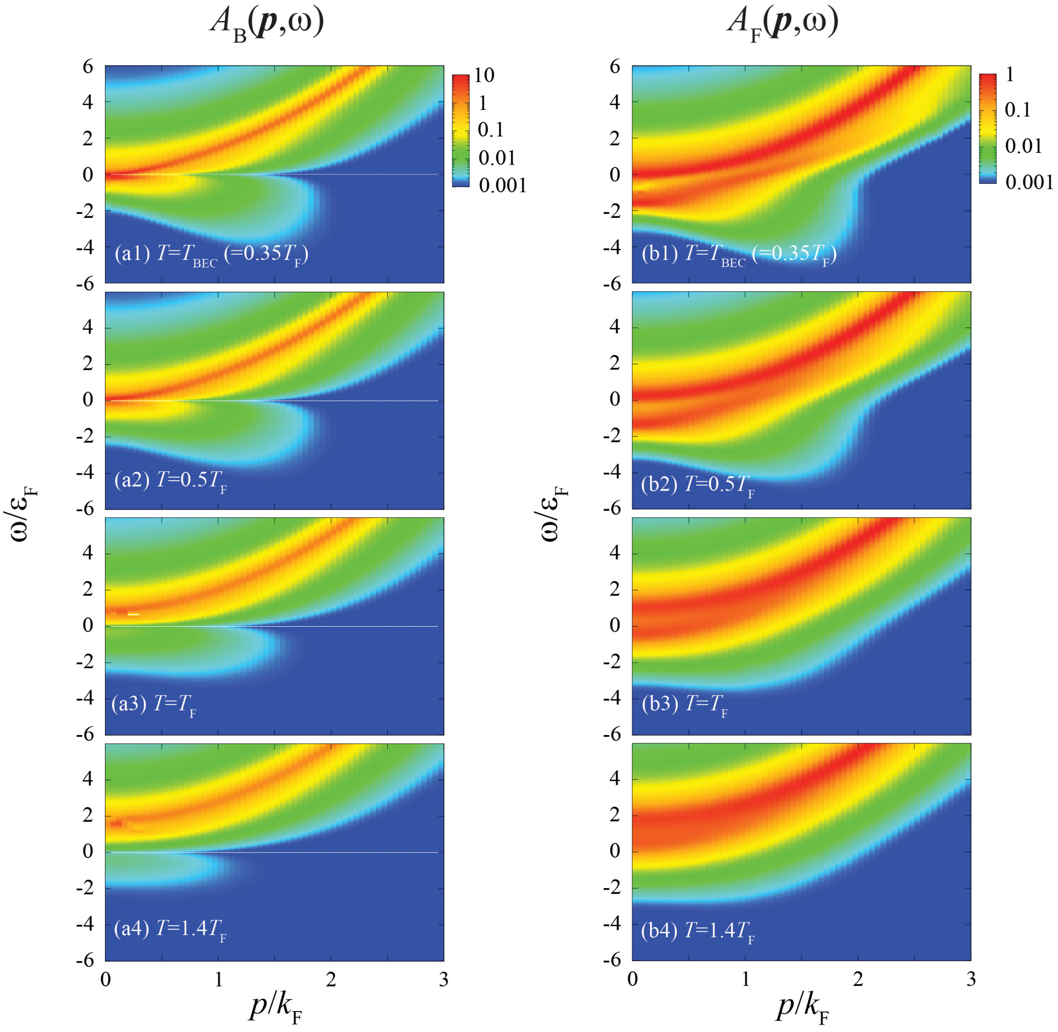

Figure 3.7: Intensity of single-particle spectral weight above $T_{\rm BEC}$. (a1)∼(a4) $A_{\rm B}(\boldsymbol{p},\omega)$. (b1)∼(b3) $A_{\rm F}(\boldsymbol{p},\omega)$. We take $(k_{\rm F}a_{\rm BF})^{-1}=0$.

3.4 Single-particle Spectral Weight above $T_{\rm BEC}$

Figures 3.6 shows the temperature dependence of the spectral weight $A_{\rm s=B,F}(\boldsymbol{p},\omega)$ when $(k_{\rm F}a_{\rm BF})^{-1}=0.5$. In Figs. 3.6(a1)-(a4) (left panels) and (b1)-(b4) (right panels) one sees that the coupling between the Fermi atomic, Bose atomic and composite fermionic excitations are gradually suppressed, as one increases of temperature, as expected. From the viewpoint of Eqs. (3.15) and (3.16), this behavior can be understood as the result of the fact that all the coupling constants $\lambda_{\rm s=B,F,CB}$ become small because the chemical potentials $\mu_{\rm F}$, $\tilde{\mu}_{\rm B}$, and $\mu_{\rm CF}$, decrease with increasing the temperature (see Fig. 3.1). We briefly note that, this tendency is also seen in other interaction strengths as shown in Figs. 3.7 and 3.8 at unitarity ($(k_{\rm F}a_{\rm BF})^{-1}=0$) and weak-coupling regime ($(k_{\rm F}a_{\rm BF})^{-1}=-1.0$), respectively. (Note that this behavior appears at lower temperatures in weaker interaction strength because the coupling between the excitations are weak.)

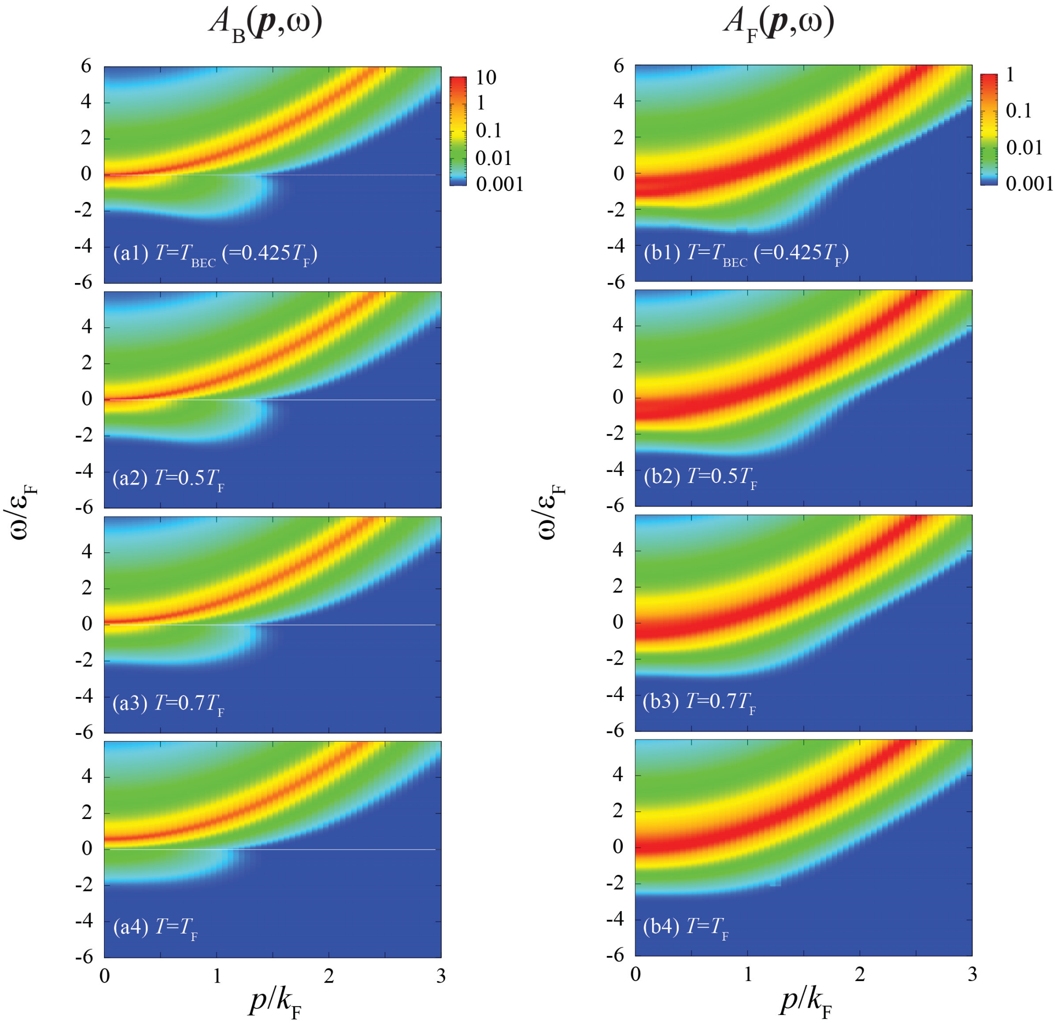

Figure 3.8: Intensity of single-particle spectral weight above T_{BEC}. (a1)∼(a4) $A_{\mathrm{B}}(\boldsymbol{p},\omega)$. (b1)∼(b3) $A_{\mathrm{F}}(\boldsymbol{p},\omega)$. We take $(k_{\mathrm{F}}a_{\mathrm{BF}})^{-1} = -1.0$.

However, we see in Figs. 3.6(a1)-(a4) and (b1)-(b4) that the spectral structure is still somehow different from the non-interacting case, even at $T \sim T_{\mathrm{F}}$. Indeed we see in Fig. 3.9 that the spectral weight $A_{\mathrm{s=B,F}}(\boldsymbol{p}=0,\omega)$ exhibits a double peak structure, as a function of the energy ω even at $T/T_{\mathrm{F}} = 1$ in $A_{\mathrm{F}}(\boldsymbol{p}=0,\omega)$, and at $T/T_{\mathrm{F}} = 0.6$ in $A_{\mathrm{B}}(\boldsymbol{p}=0,\omega)$. Regarding these the photoemission-type experiment developed by JILA group [67–69] can observe the occupied spectral weight, which is given by the product of the spectral weight (Fermi or Bose) and the Fermi or Bose distribution function, depending on the particle statistics. Thus, these anomalous spectral structures in the negative energy region may be observable even at relatively high temperatures by using this experimental technique.

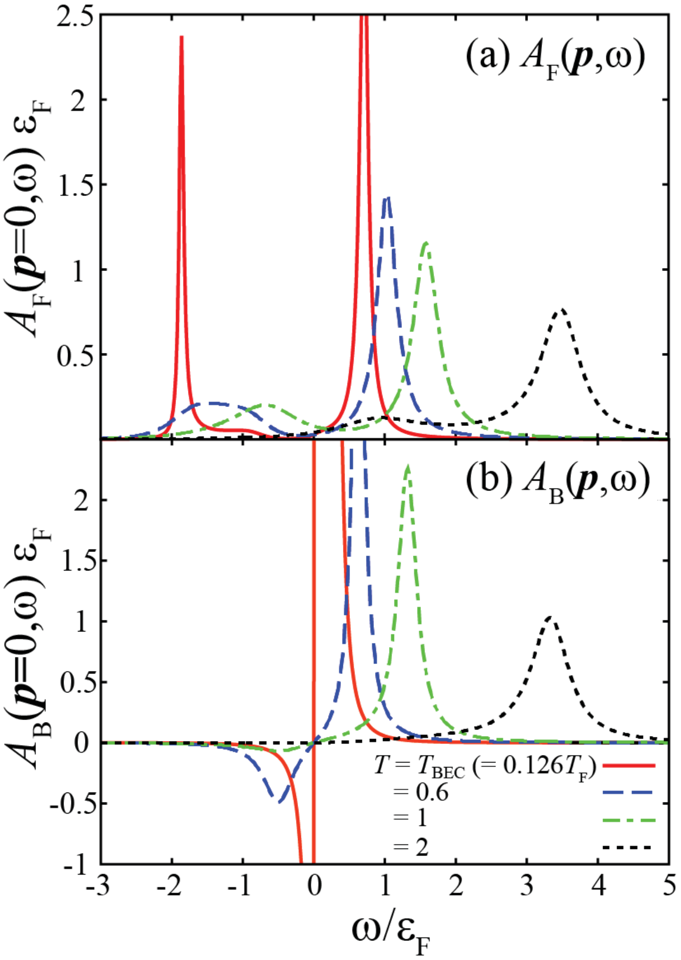

Figure 3.9: Single-particle spectral weight at $\boldsymbol{p} = 0$, as a function of energy ω. We take $(k_{\rm F}a_{\rm BF})^{-1} = 0.5$.

Chapter 4

Universal Thermodynamics of a Bose-Fermi Mixture

In this chapter, we discuss thermodynamic properties of a unitary Bose-Fermi mixture in the normal state above $T_{\rm BEC}$. To minimize the ambiguity coming from the improved T-matrix approximation (iTMA), we only use this appropriate strong-coupling theory to evaluate the Fermi ($\mu_{\rm F}$) and Bose ($\mu_{\rm B}$) chemical potential as functions of temperature. Then, we calculate various quantities, such as internal energy E, pressure P, entropy S, as well as the specific heat at constant volume C_V, by using thermodynamic identities, without further complicated iTMA calculations. In particular, we employ the so-called universal thermodynamics, which is valid for a unitary gas ($a_{\rm BF}^{-1} = 0$), to simplify the latter part of our calculations. We show that among the thermodynamic quantities calculated by this approach, the specific heat at constant volume C_V is strongly affected by hetero-nuclear pairing fluctuations, to exhibit an anomalous non-monotonic temperature dependence near $T_{\rm BEC}$. On the other hand, the other quantities (E, P, S) exhibit a monotonic temperature dependence, even in the strongly interacting unitarity limit. We point out that C_V is a useful quantity to see how strong hetero-pairing fluctuations affect system properties of a Bose-Fermi mixture at the unitarity. In this section we deal with a uniform Bose-Fermi mixture described by the Hamiltonian Eq. (2.1) with population balance ($N_{\rm B} = N_{\rm F} = N$) and mass balance ($m_{\rm B} = m_{\rm F} = m$).

4.1 Combined iTMA with Universal Thermodynamics

In the previous chapter, we clarified that hetero-pairing fluctuations remarkably modify single-particle Bose and Fermi excitations near the Bose-Einstein condensation temperature $T_{\rm BEC}$. Since thermal excitations of a Bose-Fermi mixture would reflect detailed Bose and Fermi single-particle excitation spectra, it is an interesting problem to examine thermodynamic properties of the system in the region where hetero-pairing fluctuations are strong.

In considering strong-coupling effects on various physical quantities by using an appropriate strong-coupling theory, one crucial problem is that, the reliability of this theory usually depends on what we examine. For example, in case of a two-component Fermi gas, the Gaussian pair-fluctuating theory developed by Nozieres and Schmitt-Rink (NSR) [49] is known to be able to correctly describe the so-called BCS (Bardeen-Cooper-Schrieffer)- BEC crossover behavior of the superfluid phase transition temperature $T_{\rm c}$, which however, breaks down in considering the single-particle density of states (DOS), because NSR unphysically gives negative DOS in the crossover region near $T_{\rm c}$. This problem is overcome in TMA [58], which however, is known to unphysically give negative spin susceptibility [99]. The positive susceptibility is restored by the so-called extended TMA (ETMA), however it has been shown that ETMA still has some room for improvement in the presence of mass imbalance [100, 101]. These examples means that, even when one of the calculated quantities by a strong-coupling theory agrees with an experimental result, it does not guarantee the reliability of the other calculated result by this theory.

Recently, to avoid this difficulty, in cold Fermi gas physics, Ref, [82] has proposed to combine a strong-coupling theory with thermodynamic identities, to evaluate various thermodynamic quantities in a unified manner. In this approach, complicated strong-coupling calculations to include strong-pairing fluctuations in the crossover region are only carried out in order to determine the Fermi chemical potential $\mu_{\rm F}$. Other various ground state quantities, such as the internal energy, compressibility, Tan's contact [83–85], are all derived from the calculated $\mu_{\rm F}$ by way of *exact* thermodynamic identities without relying on any approximate strong-coupling theory. An advantage of this hybrid approach is that, because the calculated quantities are related to exact thermodynamic identities, experimental confirmation for one of these results immediately mean the correctness of other quantities (even when they have not been experimentally measured). On the other hand, when one meets discrepancy between an experimental result and a calculated quantity, one may only improve the strong-coupling theory, to repeat the above mentioned procedure. Indeed using this approach, Ref. [82] succeeds in quantitatively reproducing experimental results on various ground state quantities of a superfluid Fermi gas in the BCS-unitarity regime in a unified manner.

In this chapter, we extend this previous work for an ultracold Fermi gas to a Bose-Fermi mixture, to study thermodynamic properties of this system in the normal state above $T_{\rm BEC}$. Regarding this, we point out that, in the case of Ref. [82] for an ultracold Fermi gas, the suppression of the variable T by considering the ground state has greatly simplified this approach in calculating various thermodynamic quantities from the chemical potential. In our Bose-Fermi case at finite temperatures $T \geq T_{\rm BEC}$, although we can not use this idea, we can still simplify our approach by restricting our target to a unitary Bose-Fermi mixture, because of the following reason.

As discussed in Chapter 2, we actually do not use the bare inter-species interaction $-U_{\rm BF}$ in Eq. (2.1), but the interaction strength is measured in terms of the inverse s-wave scattering length $a_{\rm BF}^{-1}$, which is related to the bare interaction $-U_{\rm BF}$ as

$$\frac{4\pi a_{\rm BF}}{m} = -\frac{U_{\rm BF}}{1 - U_{\rm BF}\sum_{\boldsymbol{p}}^{p_{\rm c}} \frac{1}{2\varepsilon_{\boldsymbol{p}}}}. \tag{4.1}$$

As usual, a_{BF}^{-1} is normalized by the Fermi momentum k_{F} of N_{F} Fermi atoms, and interaction effects are conveniently described by the dimensionless parameter $(k_{\mathrm{F}}a_{\mathrm{BF}})^{-1}$ in theory. In this case in the unitarity limit, the diverging scattering length ($|a_{\mathrm{BF}}| \to \infty$) naturally gives the vanishing "interaction parameter" $(k_{\mathrm{F}}a_{\mathrm{BF}})^{-1} = 0$, so that the only relevant energy scales are T and $\mu_{\mathrm{s=B,F}}$, because the energy scale related to inter-species interaction no longer exists, as in the non-interacting case. (Note that, however the system itself is strongly affected by the inter-species interaction.)

The thermodynamics in this special case, which is frequently referred to as the universal thermodynamics in the literature [81], allows us to use the following simple expression for the thermodynamic potential Ω as a function of $(T, \mu_{\mathrm{B}}, \mu_{\mathrm{F}})$,

$$\Omega = \frac{TV}{\lambda_T^3} F(X_{\mathrm{B}}, X_{\mathrm{F}}), \tag{4.2}$$

where V is the volume of the system, and

$$\lambda_T = \sqrt{\frac{2\pi}{mT}}, \tag{4.3}$$

is the thermal de-Broglie wavelength. In Eq. (4.1) $F(X_{\mathrm{B}}, X_{\mathrm{F}})$ is a dimensionless function, involving the dimensionless variables $X_{\mathrm{s=B,F}}$ given by,

$$X_{\mathrm{s=B,F}} = \frac{\mu_{\mathrm{s}}}{T}. \tag{4.4}$$

Starting from the expression for the thermodynamic potential Ω in Eq. (4.1), we construct a combined iTMA with universal thermodynamics, to investigate the thermodynamic properties of a normal-state "unitary" Bose-Fermi mixture ($(k_{\mathrm{F}}a_{\mathrm{BF}})^{-1} = 0$). In this regard, we briefly note that the unitarity limit is located in between the weak-coupling limit $(k_{\mathrm{F}}a_{\mathrm{BF}})^{-1} \to -\infty$ (where an ideal gas mixture of bosons and fermions are realized) and the strong-coupling limit $(k_{\mathrm{F}}a_{\mathrm{BF}})^{-1} \to +\infty$ (where the system is dominated by ideal gas of Fermi molecules). In addition, as seen in Fig. 2.12, the unitarity limit is close to the critical interaction strength ($(k_{\mathrm{F}}a_{\mathrm{BF}})^{-1} = 0.56$) at which T_{BEC} vanishes. Thus, although our approach based on universal thermodynamics can only examine in the unitarity case, it is still useful to see how the two limiting cases $(k_{\mathrm{F}}a_{\mathrm{BF}})^{-1} \to \pm\infty$ are related to each other from thermodynamic point of view.

The equation for the number $N_{\mathrm{s=B,F}}$ of atoms (s = B: boson, s = F: fermion) is conveniently obtained from the thermodynamic potential Ω as,

$$\begin{aligned} N_{\mathrm{s=B,F}} &= -\left(\frac{\partial \Omega}{\partial \mu_{\mathrm{s}}}\right)_{T,V,\mu_{-\mathrm{s}}} \\ &= -\frac{V}{\lambda_T^3}\left(\frac{\partial F}{\partial X_{\mathrm{s}}}\right)_{X_{-\mathrm{s}}}. \end{aligned} \tag{4.5}$$

Here, the second line in Eq. (4.5) is obtained by using Eq. (4.2) and "-s" stands for the opposite component to “s”. We then obtain from Eq. (4.5),

$$\begin{aligned} dF(X_{\rm B}, X_{\rm F}) &= \sum_{\rm s=B,F} \left(\frac{\partial F(X_{\rm B}, X_{\rm F})}{\partial X_{\rm s}}\right)_{X_{-\rm s}} dX_{\rm s} \\ &= -\sum_{\rm s=B,F} \frac{N_{\rm s}\lambda_T^3}{TV}\left[\frac{\partial \mu_{\rm s}(T)}{\partial T} - \frac{\mu_{\rm s}(T)}{T}\right] dT. \end{aligned} \tag{4.6}$$

In case of population balance which we are considering, one may take,

$$N_{\rm B} = N_{\rm F} = V\frac{(2m\varepsilon_{\rm F})^{3/2}}{(6\pi^2)} \tag{4.7}$$

where $\varepsilon_{\rm F} = k_{\rm F}^2/(2m)$ is the atomic Fermi energy. Substituting Eq. (4.7) into Eq. (4.6), which is followed by integration over T' between $[\infty, T]$, we have,

$$F(X_{\rm B}, X_{\rm F}) = -\frac{4\varepsilon_{\rm F}^{3/2}}{3\sqrt{\pi}} \sum_{\rm s=B,F} \int_{\infty}^{T} \frac{dT'}{T'^{5/2}} \left[\frac{d\mu_{\rm s}(T')}{dT'} - \frac{\mu_{\rm s}(T')}{T'}\right]. \tag{4.8}$$

We briefly note that the system approaches an ideal classical gas in the high temperature limit $T \to \infty$, wherein $\Omega \propto T$. Using this, we have taken $F(X_{\rm B}, X_{\rm F})|_{T\to\infty} = 0$ in obtaining Eq. (4.8).

Once the dimensionless scaling function $F(X_{\rm B}, X_{\rm F})$ is determined, the pressure P can be immediately obtained as,

$$P = -\frac{\Omega}{V} = -\frac{T}{\lambda_T^3} F(X_{\rm B}, X_{\rm F}). \tag{4.9}$$

The entropy S can also be evaluated from the thermodynamic identity as,

$$S = -\left(\frac{\partial \Omega}{\partial T}\right)_{V,\mu_{\rm s}} = V\left(\frac{\partial P}{\partial T}\right)_{\mu_{\rm s}}. \tag{4.10}$$

Taking the derivative of P in Eq. (4.9) with respect to temperature T and using Eq. (4.5) one can rewrite the expression to entropy S in Eq. (4.10) as,

$$\begin{aligned} S &= -\frac{5V}{2\lambda_T^3} F(X_{\rm B}, X_{\rm F}) - \frac{TV}{\lambda_T^3} \sum_{\rm s=B,F} \left(\frac{\partial F(X_{\rm B}, X_{\rm F})}{\partial X_{\rm s}}\right)_{X_{-\rm s}} \left(\frac{\partial X_{\rm s}}{\partial T}\right)_{\mu_{\rm s}} \\ &= \frac{5}{2}\frac{PV}{T} - \frac{1}{T}\sum_{\rm s=B,F} N_{\rm s}\mu_{\rm s}. \end{aligned} \tag{4.11}$$

The internal energy E is then determined from the thermodynamic relation as,

$$\begin{aligned} E &= -PV + TS + \sum_{\rm s=B,F} \mu_{\rm s} N_{\rm s} \\ &= \frac{3}{2} PV. \end{aligned} \tag{4.12}$$

In obtaining the last expression in Eq. (4.12) we have substituted Eqs. (4.9) and (4.11) into the first line in Eq. (4.12). Although Eq. (4.12) is just the same as the well-known formula in an ideal gas, we emphasize that is a result of the universal thermodynamics for a unitary gas. Eq. (4.12) shows that one need not calculate the entropy S, in evaluating the specific heat at constant volume C_V, that is,

$$C_V = \left(\frac{\partial E}{\partial T}\right)_V = \frac{3}{2}V\frac{dP}{dT}. \tag{4.13}$$

The above approach based on the universal thermodynamics enables us to calculate Ω, P, S, E, as well as C_V, once the Bose and Fermi chemical potential are determined as functions of temperature T.

In our combined strong-coupling iTMA with universal thermodynamics, we determine $\mu_{\rm s=B,F}(T)$ in iTMA [86,94], as explained in Chapter 3, that is we determine these from number equations (3.4) and (3.5). At the unitarity, the Bose-Fermi scattering matrix $\tilde{\Gamma}_{\rm BF}(\boldsymbol{q}, i\omega_m^{\rm F})$ in Eq. (2.68), describing effects of hetero-pairing fluctuations is reduced to, by taking $(k_{\rm F}a_{\rm BF})^{-1} \to 0$,

$$\tilde{\Gamma}_{\rm BF}(\boldsymbol{q}, i\omega_m^{\rm F}) = \frac{1}{\tilde{\Pi}_{\rm BF}(\boldsymbol{q}, i\omega_m^{\rm F}) - \sum_{\boldsymbol{p}}^{p_{\rm c}} \frac{1}{2\varepsilon_{\boldsymbol{p}}}}. \tag{4.14}$$

Since the hetero-pair correlation function does not explicitly involve the scattering length $a_{\rm BF}$, we can use the same expression as before (Eq. (2.69)),

$$\tilde{\Pi}_{\rm BF}(\boldsymbol{q}, i\omega_m^{\rm F}) = -\sum_{\boldsymbol{k}} \frac{1 - n_{\rm F}(\xi^{\rm F}_{\boldsymbol{k}+\boldsymbol{q}/2}) + n_{\rm B}(\tilde{\xi}^{\rm B}_{-\boldsymbol{k}+\boldsymbol{q}/2})}{i\omega_m^{\rm F} - \xi^{\rm F}_{\boldsymbol{k}+\boldsymbol{q}/2} - \tilde{\xi}^{\rm B}_{-\boldsymbol{k}+\boldsymbol{q}/2}}. \tag{4.15}$$

The determination for $T_{\rm BEC}$ in a unitary Bose-Fermi mixture is also the same as before

$$\mu_{\rm B} = \tilde{\Sigma}_{\rm B}(\boldsymbol{p} = 0, i\omega_n^{\rm B} = 0). \tag{4.16}$$

4.2 Virial Expansion to Evaluate $\mu_{\rm s}(T)$ in the High Temperature Region

To determine the scaling function $F(X_{\rm B}, X_{\rm F})$ from Eq. (4.8), we need $\mu_{\rm B}(T)$ and $\mu_{\rm F}(T)$ from $T_{\rm BEC}$ to the high temperature region ($T \gg T_{\rm F}$). In principle, the Bose and Fermi number equations (3.4) and (3.5) in iTMA are valid for this purpose. However, because the system approaches to a classical gas at high temperatures, we can actually avoid complicated strong-coupling iTMA calculations, thereby employing the high temperature virial expansion method [102–110].

The virial expansion for the thermodynamic potential Ω of a Bose-Fermi mixture is given by, up to the second order,

$$\begin{aligned}\Omega &= -\frac{TV}{\lambda_{\rm T}^3}\sum_{i,j} B_{ij} z_{\rm F}^i z_{\rm B}^j \\ &= -\frac{TV}{\lambda_{\rm T}^3}\left[B_{01}z_{\rm B} + B_{02}z_{\rm B}^2 + B_{10}z_{\rm F} + B_{20}z_{\rm F}^2 + B_{11}z_{\rm F}z_{\rm B}\right],\end{aligned} \tag{4.17}$$

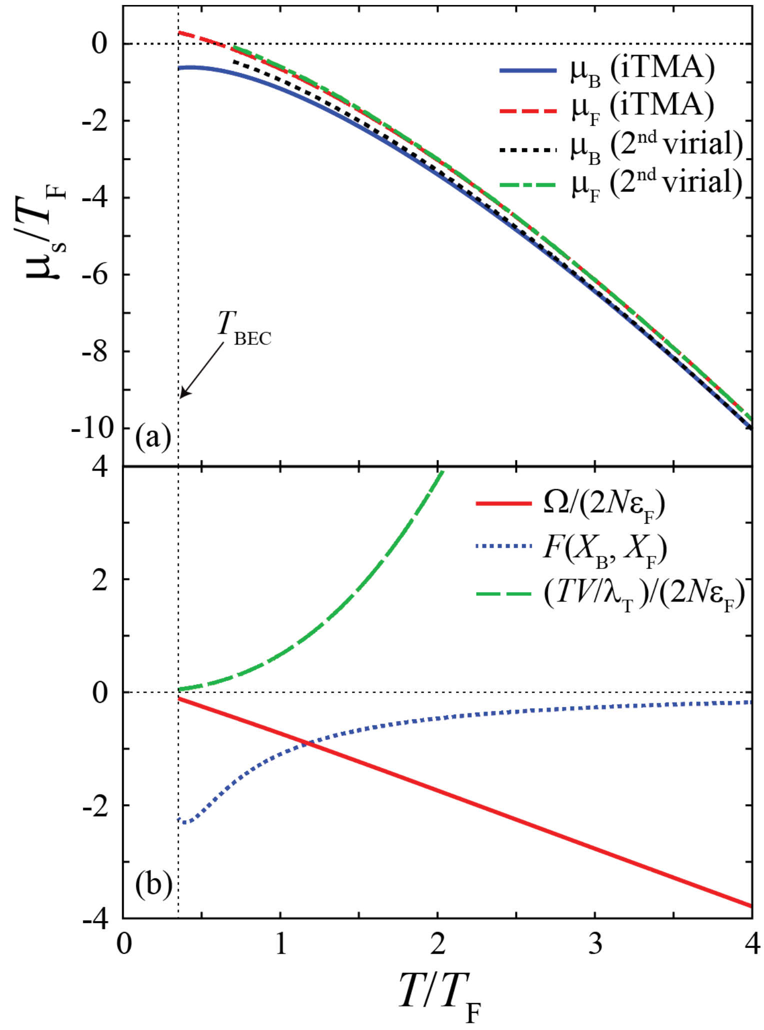

Figure 4.1: (a) Calculated Bose ($\mu_{\rm B}$) and Fermi ($\mu_{\rm F}$) chemical potential in a unitary Bose-Fermi mixture above $T_{\rm BEC}$ ($= 0.35T_{\rm F}$, where $T_{\rm F}$ is the Fermi temperature of an N Fermi atomic gas). In this figure, "2$^{\rm nd}$ virial" shows the result by the second-order virial expansion method. (b) Calculated scaling function $F(X_{\rm B}, X_{\rm F})$ as a function of temperature, which is calculated from Eq. (4.8). In this panel we also plot the thermodynamic potential Ω in Eq. (4.2), as well as the prefactor TV/λ_T^3 in this equation.

where

$$z_{\rm s=B,F} = \exp\left(\frac{\mu_{\rm s}}{T}\right), \tag{4.18}$$

is the Bose (s = B) and Fermi (s = F) fugacity. In Eq. (4.17), we implicitly assume $z_{\rm s=B,F} < 1$, or $\mu_{\rm s=B,F} < 0$, expected in the high temperature classical regime ($T \gg T_{\rm F}, T_{\rm BEC}$). B_{ij} is the virial coefficient. In particular, the coefficient B_{11} involves the effects of the inter-species interaction. Substituting Eq. (4.17) into the first line in Eq. (4.5), we have

$$N_{\rm B} = \frac{V}{\lambda_{\rm T}^3}\left[B_{01}z_{\rm B} + 2B_{02}z_{\rm B}^2 + B_{11}z_{\rm F}z_{\rm B}\right], \tag{4.19}$$

$$N_{\mathrm{F}} = \frac{V}{\lambda_{\mathrm{T}}^3}\left[B_{10}z_{\mathrm{F}} + 2B_{20}z_{\mathrm{F}}^2 + B_{11}z_{\mathrm{F}}z_{\mathrm{B}}\right]. \tag{4.20}$$

Using the standard approach, the virial coefficients B_{ij} is evaluated as

$$\begin{cases} B_{i0} = (-1)^{i+1}i^{-5/2} \\ B_{0j} = j^{-5/2} \\ B_{11} = \sqrt{2}. \end{cases} \tag{4.21}$$

We explain the outline of this derivation in Appendix E.

Figure 4.1(a) compares $(\mu_{\mathrm{F}}(T), \mu_{\mathrm{B}}(T))$ in iTMA (Eqs. (3.4) and (3.5)) with those calculated from the "2^{nd}-order" virial number equations (4.19) and (4.20) in a unitary Bose-Fermi mixture. The figure shows that the iTMA result is well reproduced by the virial expansion method when $T/T_{\mathrm{F}} \gtrsim 3$. Keeping this result in mind, we use iTMA to calculate $\mu_{\mathrm{s}}(T)$ at $T_{\mathrm{BEC}} \leq T \leq 3T_{\mathrm{F}}$, and the 2^{nd}-order virial expansion when $T \geq 3T_{\mathrm{F}}$.

This strategy gives the scaling function $F(X_{\mathrm{B}}, X_{\mathrm{F}})$ in Fig. 4.1(b). We briefly note that, although $F(X_{\mathrm{B}}, X_{\mathrm{F}})$ exhibits a non-monotonic temperature dependence near T_{BEC}, the thermodynamic potential Ω in Eq. (4.17) itself shows the expected monotonic temperature dependence, because of the T-dependent prefactor $TV/\lambda_T^3 \propto T^{5/2}$ in Eq. (4.17). To explicitly confirm the monotonic behavior of Ω, we also plot it in Fig. 4.1(b).

4.3 Thermodynamic Properties of a Unitary Bose-Fermi Mixture

Figure 4.2 shows the calculated thermodynamic quantities P, E, and S in a unitary Bose-Fermi mixture obtained from our combined iTMA with universal thermodynamics (Eqs. (4.9), (4.11), and (4.12)). Here, we briefly note on the following two issues. First, in the strongly-coupling limit, all the N atomic bosons and N atomic fermions form N composite Fermi molecules. Thus, the total number of particles changes from $2N$ to N, as one moves from the weak- to strong-coupling limit. Second, the internal energy E in strong-coupling limit shown in Fig. 4.2(b) does not involve the contribution from the binding energy of N composite fermions,

$$E_{\mathrm{bind}} = \frac{N}{ma_{\mathrm{BF}}^2}. \tag{4.22}$$

That is, the correct internal energy E_{g} in the strong-coupling limit should be

$$E_{\mathrm{g}} = E - \frac{N}{ma_{\mathrm{BF}}^2}. \tag{4.23}$$

In each panel in Fig. (4.2), one finds that the temperature dependence is rather similar to weak-coupling limit ("ideal Bose-Fermi mixture"), compared to the result in strong-coupling limit ("ideal molecular Fermi gas"). Regarding this it is important to recall that the formation of two-body bound Fermi molecules only appear when

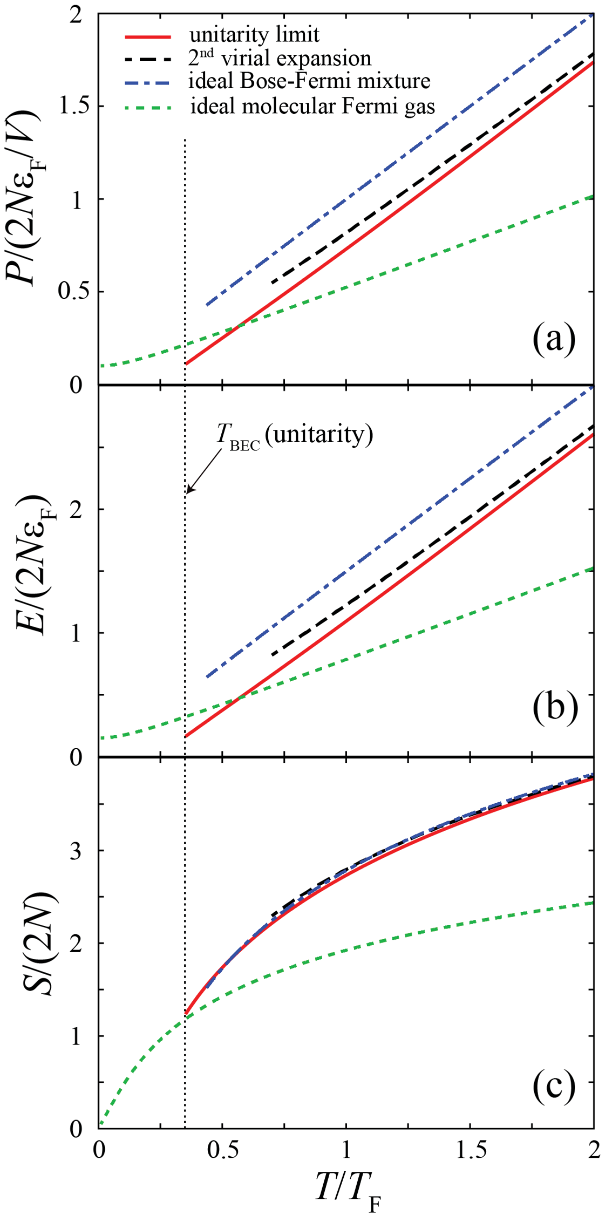

Figure 4.2: Calculated temperature dependence of thermodynamic quantities in the normal state of a unitary Bose-Fermi mixture. (a) pressure P. (b) internal energy E. (c) entropy S. In panel (b), the trivial contribution from the molecular binding energy $E_{\rm bind} = N/(ma_{\rm BF}^2)$ is subtracted from E. In this figure, "$2^{\rm nd}$ virial expansion" shows the result obtained using $\mu_{\rm s=B,F}$ obtained from the coupled number equations (4.19) and (4.20). For comparison, each panel also shows the result in weak-coupling limit ("ideal Bose-Fermi mixture," where $T_{\rm BEC} = 0.44T_{\rm F}$), as well as that in the strong-coupling limit ("ideal molecular Fermi gas," where BEC does not occur).

$a_{\rm BF}^{-1} \geq 0$. In the present system, there is competition between the Bose-Einstein condensation of atomic bosons and the formation of composite Bose-Fermi molecules, and the energetically favorable state depends on the strength of an inter-species interaction. At the unitarity, hetero-pairing fluctuations are enhanced near $T_{\rm BEC}$; however a clear molecular picture is still not valid, because of the vanishing binding energy $E_{\rm bind} \to 0$ in Eq. (4.22), although the unitarity limit ($a_{\rm BF}^{-1} = 0$) is located at the center of the weak-coupling limit ($a_{\rm BF}^{-1} \to -\infty$) and the strong-coupling limit ($a_{\rm BF}^{-1} \to +\infty$).

In a unitary Fermi gas, strong-coupling corrections to the ground state energy is characterized by the so-called Bertsch parameter [111], which is given by the ratio of the internal energy of unitary Fermi gas to that in a non-interacting Fermi gas. As an extension of this to a unitary Bose-Fermi mixture, it is interesting to relate the internal energy $E_{\rm unitarity}$ of a unitary Bose-Fermi mixture to the internal energy $E_{\rm free}$ of an ideal Bose-Fermi mixture. When we express the former energy as $E_{\rm unitarity} = \eta_{\rm BF} E_{\rm free}$, one finds, for example, at $T_{\rm BEC}$ of the ideal Bose-Fermi mixture,

$$\eta_{\rm BF} = 0.444. \tag{4.24}$$

The measurement of this parameter would be useful for the estimation of interaction effects in a unitary Bose-Fermi mixture, as well as the assessment of our theoretical approach. Because the internal energy E is directly related to the pressure P (see Eq. (4.9)), one can also evaluate $\eta_{\rm BF}$, from the observation of the pressure P, by using the combined Gibbs-Duhem relation with the local density approximation developed in Ref. [112].

However, apart from this kind of quantitative analysis, Fig. 4.2 shows that it is difficult to quantitatively discuss strong-coupling effects on the thermodynamic quantities in this figure, because their overall behavior are very much similar to those in the non-interacting case, as well as in the high temperature classical region.

4.4 Specific Heat at Constant Volume C_V and Strong coupling Effects in a Unitary Bose-Fermi Mixture

Figure 4.3 shows the specific heat at constant volume C_V. In contrast to P, E, and S, one sees in this figure that C_V exhibits a qualitatively different temperature dependence from the non-interaction case, as well as in the case of strong-coupling limit. That is, while C_V monotonically increases (decreases) with the decreasing temperature in the non-interacting case (strong-coupling limit), it exhibits a non-monotonic temperature dependence in the unitarity limit. Since, this low temperature behavior cannot be explained by the virial expansion, it is considered to be a quantum many-body phenomenon. We briefly note that, because the specific heat is physically related to energy fluctuations, it is considered to be more sensitive to pairing fluctuations than the internal energy E (as well as $P = (2/3)E/V$). Furthermore, C_V is also directly related to the temperature-derivative of entropy S, any change in the latter is magnified in the former, leading to the high sensitivity of C_V to pairing fluctuations than S.

To explore the origin of the anomalous non-monotonic behavior of C_V in Fig.

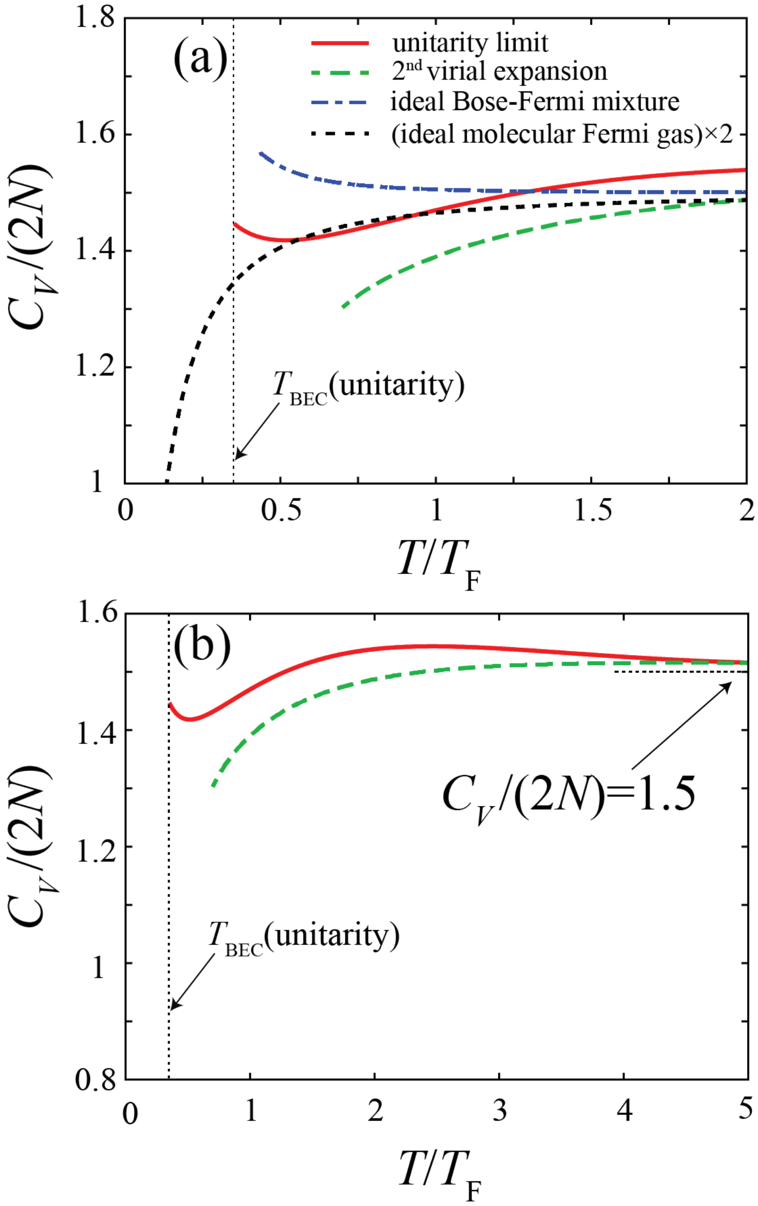

Figure 4.3: (a) Calculated specific heat at constant volume C_V in a unitary Bose-Fermi mixture. "2$^{\rm nd}$ virial expansion" shows the result by the virial expansion method. "ideal Bose-Fermi mixture" shows the specific heat in the non-interacting case. The result in the strong-coupling limit is shown as "ideal molecular Fermi gas". (b) To confirm that C_V approaches the expected value, $C_V/(2N) = 1.5$ we show the result at higher temperatures.

4.3(a), we conveniently divide C_V into the "free Fermi gas contribution",

$$C_{V0}^{\rm F} = \frac{d}{dT}\sum_{\boldsymbol{p}} \varepsilon_{\boldsymbol{p}} n_{\rm F}(\varepsilon_{\boldsymbol{p}} - \mu_{\rm F}), \tag{4.25}$$

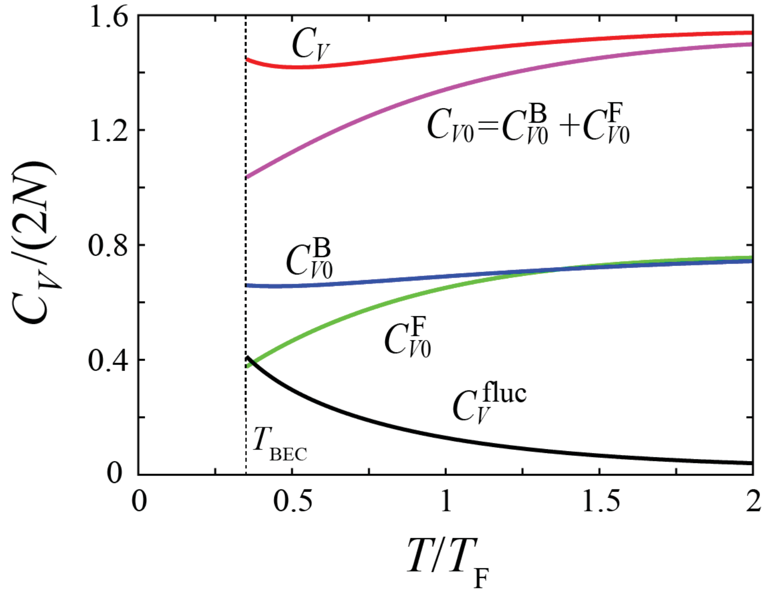

Figure 4.4: Free Bose gas contribution C_{V0}^{B} in Eq. (4.26) and free Fermi gas contribution C_{V0}^{F} in Eq. (4.25). The fluctuation contribution $C_V^{\mathrm{fluc}} \equiv C_V - C_{V0}^{\mathrm{B}} - C_{V0}^{\mathrm{F}}$ is also plotted.

"free Bose gas contribution",

$$C_{V0}^{\mathrm{B}} = \frac{d}{dT} \sum_{\boldsymbol{p}} \varepsilon_{\boldsymbol{p}} n_{\mathrm{B}}(\varepsilon_{\boldsymbol{p}} - \tilde{\mu}_{\mathrm{B}}), \tag{4.26}$$

and the remaining "fluctuation contribution",

$$C_V^{\mathrm{fluc}} = C_V - C_{V0}^{\mathrm{F}} - C_{V0}^{\mathrm{B}}. \tag{4.27}$$

Here, μ_{F} and $\tilde{\mu}_{\mathrm{B}} = \mu_{\mathrm{B}} - \tilde{\Sigma}_{\mathrm{B}}(0,0)$ are evaluated at the unitarity by iTMA. At a glance, the up-turn behavior of C_V near T_{BEC} looks similar to the well known temperature dependence of the specific heat in an ideal Bose gas near T_{BEC}. However, as shown in Fig. 4.4, the free Bose gas contribution C_{V0}^{B} in Eq. (4.26) actually monotonically decreases even near T_{BEC}, so that it cannot explain the behavior of C_V near T_{BEC}. This is because the number of "free Bose atoms",

$$N_{\mathrm{B}}^0 = \sum_{\boldsymbol{p}} n_{\mathrm{B}}(\varepsilon_{\boldsymbol{p}} - \tilde{\mu}_{\mathrm{B}}), \tag{4.28}$$

as well as the number of "free Fermi atoms",

$$N_{\mathrm{F}}^0 = \sum_{\boldsymbol{p}} n_{\mathrm{F}}(\varepsilon_{\boldsymbol{p}} - \mu_{\mathrm{F}}), \tag{4.29}$$

gradually decreases with decreasing the temperature (see Fig. 4.5), due to the growth of scattering states,

$$N_{\mathrm{fluc}} = 2N - N_{\mathrm{B}}^0 - N_{\mathrm{F}}^0, \tag{4.30}$$

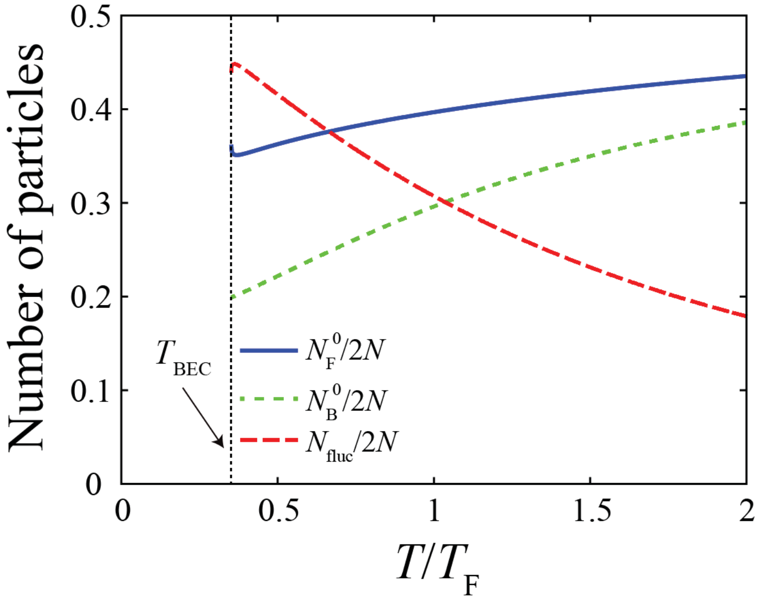

Figure 4.5: The particle number $N_{\rm B}^0$ ($N_{\rm F}^0$) of free Bose (Fermi) atoms, contributing to specific heat $C_{V0}^{\rm B}$ ($C_{V0}^{\rm F}$).

reflecting the enhancement of hetero-pairing fluctuations at low temperatures, As a result the ordinary monotonic increase of the specific heat with decreasing the temperature in an ideal Bose gas is suppressed by the decrease in the number $N_{\rm B}^0$ of Bose atoms that can contribute to BEC.

Since the specific heat in a free Fermi gas monotonically decrease as one decreases the temperature, the decrease of $N_{\rm F}^0$ seen in Fig. 4.5 promotes this characteristic behavior. Thus, the “free particle contribution”,

$$C_{\rm V0} = C_{\rm V0}^{\rm B} + C_{\rm V0}^{\rm F}, \tag{4.31}$$

cannot explain the upturn behavior of C_V in a unitary Bose-Fermi mixture near $T_{\rm BEC}$.

On the other hand, the fluctuation contribution $C_V^{\rm fluc}$ in Eq. (4.27) is enhanced near $T_{\rm BEC}$, reflecting the enhancement of Bose-Fermi pairing fluctuations. Thus, the temperature ($\equiv T_{\rm dip} \simeq 0.5T_{\rm F}$) where the specific heat C_V exhibits a dip structure is due to the fact that the enhancement of the fluctuation contribution $C_V^{\rm fluc}$ exceeds the suppression of the free atomic contribution C_{V0}. In that sense, the dip temperature $T_{\rm dip}$ may be physically interpreted as a characteristic temperature below which hetero-pairing fluctuations are important.

We briefly note that, in addition to the upturn behavior near $T_{\rm BEC}$, C_V in a unitary Bose-Fermi mixture also exhibits a hump structure around $T/T_{\rm F} \sim 2$, as shown in Fig. 4.3(b). Since, C_V in a non-interacting case simply decrease with decrease in temperature, this structure is considered to be coming from the inter-species interaction. However, this hump structure appears in the classical region ($T/T_{\rm F} \simeq\gg 1$), this phenomenon essentially is different from quantum phenomenon. Indeed, a similar structure is already obtained by the high temperature 2nd order

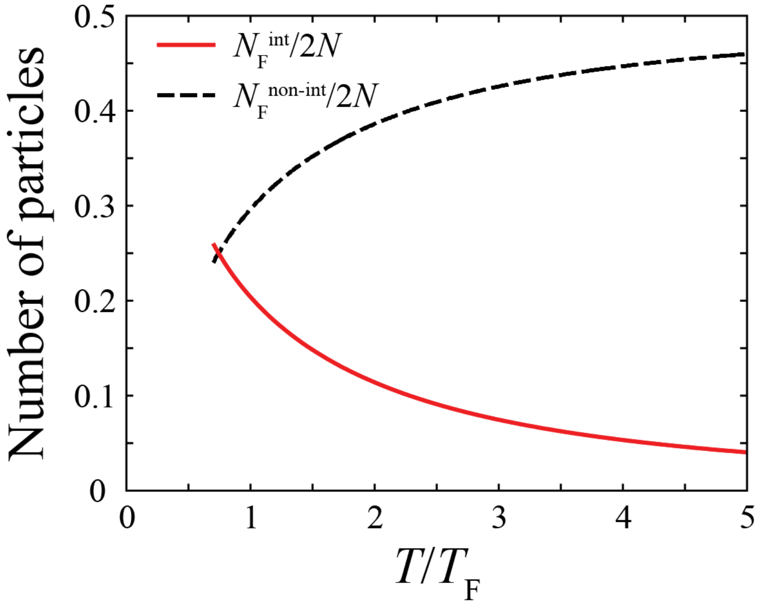

Figure 4.6: “Non-interacting component” $N_{\rm F}^{\rm non-int}$ in Eq. (4.32) and “interacting component” $N_{\rm F}^{\rm int}$ in Eq. (4.33), as function of temperature. The total number of Fermi atoms $N = N_{\rm F}^{\rm non-int} + N_{\rm F}^{\rm int}$. We note that the same result is obtained in the Bose case in Eq. (4.19).

virial expansion, as shown in Fig. 4.3(b). Regarding this, when we divide the number equation (4.20) into the “non-interacting component”,

$$N_{\rm F}^{\rm non-int} = \frac{V}{\lambda_{\rm T}^3}\left(B_{10}z_{\rm F} + 2B_{20}z_{\rm F}^2\right), \tag{4.32}$$

and the “interacting component”,

$$N_{\rm F}^{\rm int} = \frac{V}{\lambda_{\rm T}^3}B_{11}z_{\rm F}z_{\rm B}, \tag{4.33}$$

we find that the latter remains up to a relatively high temperature regime ($T/T_{\rm F} > 1$), as shown in Fig. 4.6, indicating that we cannot ignore effects of the inter-species interaction there.

As a future problem it is interesting to investigate the interaction dependence of $C_V(T)$ from weak-coupling to strong-coupling regime, passing through the unitarity limit. In this case, when one moves from the weak-coupling side to the unitarity limit, if the upturn behavior of C_V once vanishes at an interaction strength ($\equiv \tilde{a}_{\rm BF}^{-1}$ (< 0)), this anomalous behavior of C_V in the region

$$\tilde{a}_{\rm BF}^{-1} \le a_{\rm BF}^{-1} \le 0, \tag{4.34}$$

can physically be regarded as effects of hetero-pairing fluctuations. Since the present theory uses the universal thermodynamics [81], it is not applicable to the region away from the unitarity limit. Thus, improving our theory to that which does not rely on the universal thermodynamics is a crucial future challenge, in order to explore the above-mentioned possibility.

Chapter 5

Summary

To summarize, we have investigated strong-coupling properties of a Bose-Fermi mixture, consisting of a one-component Bose atoms and one-component Fermi atoms, with a tunable inter-species pairing interaction associated with a hetero-nuclear Feshbach resonance. To include strong hetero-pairing fluctuations in the normal state above $T_{\rm BEC}$, we improved the ordinary non-self-consistent T-matrix approximation (TMA) by replacing all the bare Bose Green's function appearing in the TMA self-energy diagrams by a modified one so that the gapless condition for Bose excitations at $T_{\rm BEC}$ can be satisfied everywhere in the diagrams. We showed that this improvement can successfully remove the unphysical behavior of the Fermi chemical potential near the critical interaction strength at which $T_{\rm BEC}$ vanishes.

Using this improved T-matrix approximation (iTMA), we calculated the single-particle density of states $\rho_{\rm s=B,F}(\omega)$, as well as the spectral weight $A_{\rm s=B,F}(\boldsymbol{p},\omega)$ in both the Bose and Fermi components of a Bose-Fermi mixture, to see how hetero-pairing fluctuations affect single-particle properties of the system. From the calculated spectral structure of $A_{\rm s=B,F}(\boldsymbol{p},\omega)$, we clarified that hetero-pairing fluctuations lead to a coupling phenomenon among the Fermi atomic excitations, Bose atomic excitations, as well as Fermi molecular excitations. A similar coupling phenomenon is also known in the BCS-BEC crossover regime of a two-component Fermi gas, where fluctuations in the Cooper channel couple Fermi atomic excitations with the Fermi hole excitations. However, the coupling phenomenon in the latter leads to a pseudo-gapped density of states, we found that it does not cause a dip structure in $\rho_{\rm F}(\omega)$, even in the unitary regime ($(k_{\rm F}a_{\rm BF})^{-1}=0$) of a Bose-Fermi mixture. A shallow dip structure only appears in $\rho_{\rm F}(\omega)$ in the strong-coupling regime. On the other hand, we showed that the coupling phenomenon in the case of a Bose-Fermi mixture causes a triple peak structure in the spectral weight $A_{\rm s=B,F}(\boldsymbol{p},\omega)$, reflecting the coupling among Bose atomic, Fermi atomic and Fermi molecular excitations. We emphasize that such a structure does not appear in the case of a two-component Fermi gas, so that it is a unique feature of a Bose-Fermi mixture with a strong inter-species pairing interaction. We also clarified that this coupling gives negative Bose density of states $\rho_{\rm B}(\omega)<0$ in the negative energy regime.

Besides single-particle excitations, we have also studied thermodynamic properties and strong coupling effects in a unitary Bose-Fermi mixture above $T_{\rm BEC}$. For this purpose we combined our iTMA with universal thermodynamics developed by

Ho, to evaluate the chemical potential $\mu_{\rm s=B,F}(T)$, internal energy $E(T)$, pressure $P(T)$, entropy $S(T)$, as well as specific heat at constant volume $C_V(T)$ as functions of temperature at unitarity. Among them, we found that $C_V(T)$ exhibits non-monotonic temperature dependence, which qualitatively differs from the temperature dependence in the weak-coupling and strong-coupling limit. We pointed out that, this anomalous behavior of $C_V(T)$ originates from the fluctuation correction to this quantity which is enhanced near $T_{\rm BEC}$. On the other hand, the other quantities $E(T)$, $P(T)$, and $S(T)$ exhibit monotonic behavior as in the case of a non-interacting Bose-Fermi case. In this sense, the specific heat $C_V(T)$ is a useful thermodynamic quantity for the study of strong-coupling effects in a unitary Bose-Fermi mixture. (Note that this quantity has recently become observable in cold atom physics.)

In this thesis, we have ignored mass difference between the Bose and Fermi atoms, as well as effects of a harmonic trap, for simplicity. In addition we have only taken into account a Bose-Fermi inter-species interaction, ignoring any other intra-species interactions. Inclusion of these remains as our future problem. Since a strongly-interacting Bose-Fermi mixture is a counterpart of an ultracold Fermi gas, our results would contribute to the further understanding of strong-coupling properties of a quantum system from a more general point of view.

Acknowledgements

I would like to express my sincerest gratitude and appreciation to my supervisor Prof. Yoji Ohashi for giving me the opportunity to be part of his research group, and also in turn allowing me to experience life living in Japan. I would like to thank him for his continued guidance and commitment to my research, and also being very benevolent and supportive over these three years. His supervision has allowed me to discover exciting aspects of research, as well as grow as a researcher. I am also very pleased with the research environment where I could concentrate all my efforts on studies and research.

I would also like to acknowledge Profs. Hiroshi Takano, Shinichi Watanabe, and Yoichi Kamihara as the referees of my thesis, for their helpful comments and suggestions which were useful in improving this work in the final stage.

I am very grateful to Dr. Daisuke Inotani for all discussions and advice that he gave me concerning my research. I would also like to thank Dr. Ryo Hanai and Dr. Hiroyuki Tajima for being available for discussions most of the times, and providing assistance whenever I had problems. I am also grateful to all my lab mates Dr. Tokitake Yamaguchi, Pieter van Wyk, Morio Matsumoto, Daichi Kagamihara, Miki Ota, Yusuke Muto, and Soumita Mondal for creating a good research atmosphere in the Ohashi Lab.

I would like to give a heartfelt gratitude to my mother and father, Rajani and Mahendra Kharga for teaching me invaluable lessons of hard work and perseverance. It is hard to imagine where I would be without my family's guiding support and love, as they have always kept me motivated and focussed. And lastly but certainly not the least, I would like to thank all my friends back home in India who have always been there, whenever I needed any support or felt homesick.

Appendix A

Matsubara Summation Technique

In this appendix, we show the Matsubara summation technique which has been used in obtaining Eq. (2.15).

First, let us consider any complex function given by $g(z)$ such that it has simple poles z_0 in the complex plane as shown in Fig. A.1. Now for instance, let us take another arbitrary complex function $H(z)$ given by,

$$\begin{aligned} H(z) &= g(z)n_{\mathrm{B}}(z) \\ &= \frac{g(z)}{\exp(z/T)-1}. \end{aligned} \tag{A.1}$$

Hence, this function $H(z)$ has additional poles given by,

$$\exp(z/T)-1=0, \tag{A.2}$$

which is at

$$\begin{aligned} z &= i\omega_n^{\mathrm{B}} \\ &= i2n\pi T, \end{aligned} \tag{A.3}$$

due to the presence of Bose distribution function $n_{\mathrm{B}}(z)$. Here $\omega_n^{\mathrm{B}} = 2\pi nT$ is boson Matsubara frequency and $n = 0, \pm 1, \pm 2, \pm 3, \cdots$. Then, we can evaluate the complex integral given below by taking any of the two contours C_0 and C as shown in Fig. A.1, given by

$$-\frac{i}{2\pi}\oint dz H(z) = \begin{cases} \displaystyle\sum_{z_0} \frac{\mathrm{Res}[g(z_0)]}{\exp(z_0/T)-1} & \text{taking contour } C_0, \\ \\ \displaystyle -T\sum_{\omega_n^{\mathrm{B}}} g(i\omega_n^{\mathrm{B}}) & \text{taking contour } C. \end{cases} \tag{A.4}$$

Thus, equating the terms on the right of Eq. (A.4) one obtains,

$$-T\sum_{\omega_n^{\mathrm{B}}} g(i\omega_n^{\mathrm{B}}) = \sum_{z_0} \frac{\mathrm{Res}[g(z_0)]}{\exp(z_0/T)-1} \tag{A.5}$$

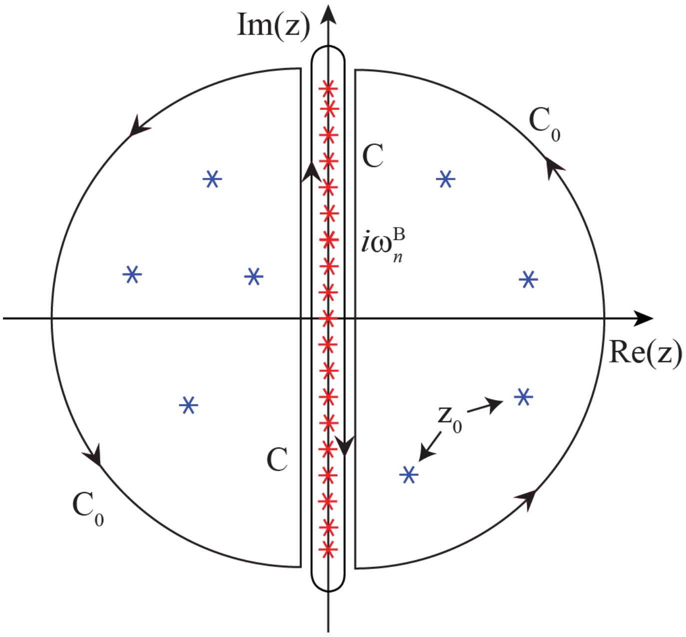

Figure A.1: C and C_0 show two contours enclosing the poles of $H(z)$, respectively, along the imaginary axis given by $i\omega_n^{\mathrm{B}}$ due to Bose distribution function $n_{\mathrm{B}}(z)$ (red crosses), and that enclosing the poles z_0 due to complex function $g(z)$ (blue crosses).

Hetero-nuclear pair correlation function $\Pi_{\mathrm{BF}}(\boldsymbol{q}, i\omega_m^{\mathrm{F}})$ in the first line of Eq. (2.15) can be written as,

$$\Pi_{\mathrm{BF}}(\boldsymbol{q}, i\omega_m^{\mathrm{F}}) = T \sum_{\boldsymbol{k},\omega_n^{\mathrm{B}}} \frac{1}{i\omega_m^{\mathrm{F}} - i\omega_n^{\mathrm{B}} - \xi^{\mathrm{F}}_{-\boldsymbol{k}+\frac{\boldsymbol{q}}{2}}} \frac{1}{i\omega_n^{\mathrm{B}} - \xi^{\mathrm{B}}_{\boldsymbol{k}+\frac{\boldsymbol{q}}{2}}} \tag{A.6}$$

and using Eq. (A.5), one may rewrite Eq. (A.6) into,

$$\Pi_{\mathrm{BF}}(\boldsymbol{q}, i\omega_m^{\mathrm{F}}) = -\sum_{\boldsymbol{k}} \left[\frac{n_{\mathrm{B}}(\xi^{\mathrm{B}}_{-\boldsymbol{k}+\boldsymbol{q}/2})}{i\omega_m^{\mathrm{F}} - \xi^{\mathrm{F}}_{\boldsymbol{k}+\boldsymbol{q}/2} - \xi^{\mathrm{B}}_{-\boldsymbol{k}+\boldsymbol{q}/2}} + \frac{-n_{\mathrm{B}}(i\omega_n^{\mathrm{F}} - \xi^{\mathrm{F}}_{\boldsymbol{k}+\boldsymbol{q}/2})}{i\omega_m^{\mathrm{F}} - \xi^{\mathrm{F}}_{\boldsymbol{k}+\boldsymbol{q}/2} - \xi^{\mathrm{B}}_{-\boldsymbol{k}+\boldsymbol{q}/2}} \right]. \tag{A.7}$$

Furthermore, one can take,

$$\begin{aligned} n_{\mathrm{B}}(i\omega_n^{\mathrm{F}} - \xi^{\mathrm{F}}_{\boldsymbol{k}+\boldsymbol{q}/2}) &= \frac{1}{-\exp(-\xi^{\mathrm{F}}_{\boldsymbol{k}+\boldsymbol{q}/2}) - 1} \\ &= -\frac{\exp(\xi^{\mathrm{F}}_{\boldsymbol{k}+\boldsymbol{q}/2})}{\exp(\xi^{\mathrm{F}}_{\boldsymbol{k}+\boldsymbol{q}/2}) + 1} \\ &= -[1 - n_{\mathrm{F}}(\xi^{\mathrm{F}}_{\boldsymbol{k}+\boldsymbol{q}/2})], \end{aligned} \tag{A.8}$$

where we have used $\exp(i\omega_m^{\mathrm{F}}/T) = -1$. Here, $\omega_m^{\mathrm{F}} = (2m+1)\pi T$ is the fermion Matsubara frequency where $m = \pm 1, \pm 2, \pm 3, \cdots$. Using Eq. (A.8), we reach

$$\Pi_{\mathrm{BF}}(\boldsymbol{q}, i\omega_m^{\mathrm{F}}) = -\sum_{\boldsymbol{k}} \frac{1 - n_{\mathrm{F}}(\xi^{\mathrm{F}}_{\boldsymbol{k}+\boldsymbol{q}/2}) + n_{\mathrm{B}}(\xi^{\mathrm{B}}_{-\boldsymbol{k}+\boldsymbol{q}/2})}{i\omega_m^{\mathrm{F}} - \xi^{\mathrm{F}}_{\boldsymbol{k}+\boldsymbol{q}/2} - \xi^{\mathrm{B}}_{-\boldsymbol{k}+\boldsymbol{q}/2}}. \tag{A.9}$$

Appendix B

Condition for Gapless Bose Excitations

Here, we will show that the Hugenholtz-Pines condition [91] for interacting bosons can be extended to the case of a Bose-Fermi mixture studied in this thesis. For this, we consider the model Hamiltonian in Eq.(2.1) in the coordinate-space representation,

$$H = \sum_{\rm s=B,F} \int d\boldsymbol{r} \psi_{\rm s}^{\dagger}(\boldsymbol{r}) \left[-\frac{\nabla^2}{2m} - \mu_{\rm s} \right] \psi_{\rm s}(\boldsymbol{r}) - U_{\rm BF} \int d\boldsymbol{r} \psi_{\rm B}^{\dagger}(\boldsymbol{r}) \psi_{\rm F}^{\dagger}(\boldsymbol{r}) \psi_{\rm F}(\boldsymbol{r}) \psi_{\rm B}(\boldsymbol{r}), \quad \text{(B.1)}$$

where $\psi_{\rm s=B,F}^{\dagger}(\boldsymbol{r})$ are the Bose (s=B) and Fermi (s=F) field operators. We add a fictitious Hamiltonian to the system to discuss the Hugenholtz-Pines condition, given as

$$\begin{aligned} H'(\lambda_{\rm B}) &= \int d\boldsymbol{r} \left[\psi_{\rm B}^{\dagger}(\boldsymbol{r}) \lambda_{\rm B} + \psi_{\rm B}(\boldsymbol{r}) \lambda_{\rm B}^* \right] \\ &= \int d\boldsymbol{r} \hat{\Psi}_{\rm B}^{\dagger}(\boldsymbol{r}) \hat{\Lambda}_{\rm B}, \end{aligned} \quad \text{(B.2)}$$

where

$$\hat{\Psi}_{\rm B}(\boldsymbol{r}) = \left(\begin{array}{c} \psi_{\rm B}(\boldsymbol{r}) \\ \psi_{\rm B}^{\dagger}(\boldsymbol{r}) \end{array} \right), \quad \text{(B.3)}$$

$$\hat{\Lambda}_{\rm B} = \left(\begin{array}{c} \lambda_{\rm B} \\ \lambda_{\rm B}^* \end{array} \right). \quad \text{(B.4)}$$

Here, $\lambda_{\rm B}$ is a complex number which is taken to be zero at the end of this discussion. In Eq. (B.2) $H'(\lambda_{\rm B})$ gives the phase of the uniform Bose superfluid order parameter as,

$$\Delta_{\rm B} = \langle \psi_{\rm B}(\boldsymbol{r}) \rangle, \quad \text{(B.5)}$$

in the BEC phase. It is important to note that Eq. (B.5) becomes real such that $\Delta_{\rm B} \equiv \Delta_{\rm B}^0$, when $\lambda_{\rm B}$ is chosen to be real ($\lambda_{\rm B} = \lambda_{\rm B}^* \equiv \lambda_B^0$).

Now, if we change the phase of $\lambda_{\rm B}$ in Eq. (B.4) from $\lambda_{\rm B}^0$ by $\delta\phi \ll 1$, then one obtains

$$\lambda_{\rm B} = \lambda_{\rm B}^0 e^{i\delta\phi}. \tag{B.6}$$

So, in order to reinstate the Hamiltonian $H + H'$ to the original form, one needs to perform the canonical transformation, such that

$$\psi_{\rm B}(\boldsymbol{r}) \to \psi_{\rm B}(\boldsymbol{r}) e^{i\delta\phi}. \tag{B.7}$$

This transforms Eq. (B.5) and its conjugate as,

$$\begin{pmatrix} \Delta_{\rm B} \\ \Delta_{\rm B}^* \end{pmatrix} = e^{i\delta\phi\tau_z} \begin{pmatrix} \Delta_{\rm B}^0 \\ \Delta_{\rm B}^0 \end{pmatrix} \simeq \begin{pmatrix} \Delta_{\rm B}^0 \\ \Delta_{\rm B}^0 \end{pmatrix} + \delta\hat{\Delta}_{\rm B}, \tag{B.8}$$

where τ_z is the Pauli matrix, and

$$\delta\hat{\Delta}_{\rm B} \equiv i\delta\phi\Delta_{\rm B}^0 \tau_z \begin{pmatrix} 1 \\ 1 \end{pmatrix}. \tag{B.9}$$

Equation (B.9) can also be obtained by evaluating the response of the BEC order parameter $\Delta_{\rm B}$ to the perturbation,

$$\delta H' \equiv H'(\lambda_{\rm B}^0 e^{i\delta\phi}) - H'(\lambda_{\rm B}^0) = i\lambda_{\rm B}^0 \delta\phi \int d\boldsymbol{r} \hat{\Psi}_{\rm B}^\dagger(\boldsymbol{r}) \tau_z \begin{pmatrix} 1 \\ 1 \end{pmatrix}. \tag{B.10}$$

Using the standard linear response theory, we obtain [88]

$$\begin{aligned} \delta\hat{\Delta}_{\rm B} &= \hat{G}_{\rm B}(\boldsymbol{p} = 0, i\omega_n^{\rm B} = 0)\delta\hat{\Lambda}_{\rm B} \\ &= i\lambda_{\rm B}^0 \delta\phi \hat{G}_{\rm B}(\boldsymbol{p} = 0, i\omega_n^{\rm B} = 0)\tau_z \begin{pmatrix} 1 \\ 1 \end{pmatrix}, \end{aligned} \tag{B.11}$$

where $\delta\hat{\Lambda}_{\rm B}$ transforms similar to Eq. (B.9). Here,

$$\hat{G}_{\rm B}(\boldsymbol{p}, i\omega_n^{\rm B}) = \frac{1}{i\omega_n^{\rm B}\tau_z - \xi_{\boldsymbol{p}}^{\rm B} - \hat{\Sigma}_{\rm B}(\boldsymbol{p}, i\omega_n^{\rm B})} \tag{B.12}$$

is the 2×2-matrix single-particle thermal Bose Green's function, with $\hat{\Sigma}_{\rm B}$ being the 2×2-matrix self-energy. Equations (B.9) and (B.11) give

$$\begin{aligned} \lambda_{\rm B}^0 \tau_z \begin{pmatrix} 1 \\ 1 \end{pmatrix} &= \hat{G}_{\rm B}(0,0)^{-1} \tau_z \begin{pmatrix} 1 \\ 1 \end{pmatrix} \Delta_{\rm B}^0 \\ &= \left[\mu_{\rm B} - \hat{\Sigma}_{\rm B}(0,0)\right] \tau_z \begin{pmatrix} 1 \\ 1 \end{pmatrix} \Delta_{\rm B}^0. \end{aligned} \tag{B.13}$$

Taking the limit $\lambda_{\rm B}^0 \to 0$ in the BEC phase ($\Delta_{\rm B}^0 \neq 0$), we find that Eq. (B.13) is satisfied when

$$[\mu_{\rm B} - \hat{\Sigma}_{\rm B}(0,0)]\tau_z \begin{pmatrix} 1 \\ 1 \end{pmatrix} = 0. \tag{B.14}$$

This is just the same form as the Hugenholtz-Pines condition [91]. At $T_{\rm BEC}$, the off-diagonal components of the matrix self-energy $\hat{\Sigma}_{\rm B}(0,0)$ vanishes, so that the (1,1)-component of Eq. (B.14) gives $\mu_{\rm B} - \Sigma_{\rm B}^{11}(0,0) = 0$. Noting that $\Sigma_{\rm B}^{11}(\boldsymbol{p}, i\omega_n^{\rm B})$ equals $\Sigma_{\rm B}(\boldsymbol{p}, i\omega_n^{\rm B})$ appearing in Eq. (2.12) at $T_{\rm BEC}$, we obtain Eq. (2.17). It is important to note that this relation also holds for iTMA formalism shown in Sec. 2.5.

Appendix C

Ultracold Gas Mixtures in the Strong-coupling Limit

C.1 Bose-Fermi Mixture

In the strong-coupling limit, all Bose and Fermi atoms combine to form tightly bound composite fermions, so that both Bose and Fermi chemical potential are expected to be negative $\mu_{\rm s=B,F} \to -\infty$. In this case, we can neglect both the Bose and Fermi distribution function $n_{\rm s=B,F}$ from Eq. (2.15), giving

$$\begin{aligned} \Pi_{\rm BF}(\boldsymbol{q}, i\omega_m^{\rm F}) &\simeq -\sum_{\boldsymbol{k}}^{p_{\rm c}} \frac{1}{i\omega_m^{\rm F} - \xi_{\boldsymbol{k}+\boldsymbol{q}/2}^{\rm F} - \xi_{-\boldsymbol{k}+\boldsymbol{q}/2}^{\rm B}} \\ &= \frac{m}{2\pi^2} p_{\rm c} - \frac{m}{4\pi}\sqrt{m\Big(\frac{q^2}{4m} - \mu_{\rm F} - \mu_{\rm B} - i\omega_m^{\rm F}\Big)}, \qquad \text{(C.1)} \end{aligned}$$

where $p_{\rm c}$ is a momentum cut-off. Here, we take $m_{\rm B} = m_{\rm F} = m$ as in our thesis. Substituting Eq. (C.1) into Eq. (2.14), we obtain

$$\begin{aligned} \Gamma_{\rm BF}(\boldsymbol{q}, i\omega_m^{\rm F}) &= \frac{1}{\frac{m}{4\pi a_{\rm BF}} + \Big[\Pi_{\rm BF}(\boldsymbol{q}, i\omega_m^{\rm F}) - \sum_{\boldsymbol{p}}^{p_{\rm c}} \frac{m}{\boldsymbol{p}^2}\Big]}, \\ &= \frac{4\pi}{m} \frac{1}{\frac{1}{a_{\rm BF}} - \sqrt{m\Big(\frac{q^2}{4m} - \mu_{\rm F} - \mu_{\rm B} - i\omega_m^{\rm F}\Big)}} \\ &= \frac{4\pi}{m} \frac{\frac{1}{a_{\rm BF}} + \sqrt{m\Big(\frac{q^2}{4m} - \mu_{\rm F} - \mu_{\rm B} - i\omega_m^{\rm F}\Big)}}{\frac{1}{a_{\rm BF}^2} - m\Big(\frac{q^2}{4m} - \mu_{\rm F} - \mu_{\rm B} - i\omega_m^{\rm F}\Big)} \\ &= \frac{4\pi}{m^2 a_{\rm BF}} \frac{1 + \sqrt{\frac{\Big(\frac{q^2}{4m} - \mu_{\rm F} - \mu_{\rm B} - i\omega_m^{\rm F}\Big)}{E_{\rm bind}}}}{E_{\rm bind} - \Big(\frac{q^2}{4m} - \mu_{\rm F} - \mu_{\rm B} - i\omega_m^{\rm F}\Big)}, \qquad \text{(C.2)} \end{aligned}$$

where $E_{\rm bind} = 1/(m a_{\rm BF}^2)$ is the binding energy of a Bose-Fermi molecule. Taking

$$\mu_{\rm CF} = \mu_{\rm B} + \mu_{\rm F} + E_{\rm bind}, \qquad \text{(C.3)}$$

one can rewrite Eq. (C.2) as

$$\begin{aligned}\Gamma_{\mathrm{BF}}(\boldsymbol{q}, i\omega_m^{\mathrm{F}}) &= \frac{4\pi}{m^2 a_{\mathrm{BF}}} \frac{1 + \sqrt{\dfrac{\left(E_{\mathrm{bind}} + \frac{q^2}{4m} - \mu_{\mathrm{CF}} - i\omega_m^{\mathrm{F}}\right)}{E_{\mathrm{bind}}}}}{i\omega_m^{\mathrm{F}} - \left(\frac{q^2}{2M} - \mu_{\mathrm{CF}}\right)} \\ &= \frac{8\pi}{m^2 a_{\mathrm{BF}}} \frac{1}{i\omega_m^{\mathrm{F}} - \xi_{\boldsymbol{q}}^{\mathrm{CF}}},\end{aligned} \tag{C.4}$$

where we have used the fact $E_{\mathrm{bind}} \gg [q^2/(2M) - \mu_{\mathrm{CF}} - i\omega_m^{\mathrm{F}}]$.

In Eq. (C.4), one finds that Bose-Fermi particle-particle matrix $\Gamma_{\mathrm{BF}}(\boldsymbol{q}, i\omega_m^{\mathrm{F}})$ reduces to a molecular Fermi propagator with molecular mass $M = 2m$ and $\xi_{\boldsymbol{q}}^{\mathrm{CF}} = q^2/(2M) - \mu_{\mathrm{CF}}$, where μ_{CF} in Eq. (C.3) works as the molecular Fermi chemical potential. Equation (C.4) also holds for $\tilde{\Gamma}_{\mathrm{BF}}(\boldsymbol{q}, i\omega_m^{\mathrm{F}})$ in iTMA.

C.2 Two-component Fermi Gas

Proceeding similar to Appendix C.1, one can also reach the strong-coupling-limit expression for the pair-correlation function $\Pi_{\mathrm{FF}}(\boldsymbol{q}, i\omega_m^{\mathrm{B}})$ in a two-component Fermi gas as,

$$\Pi_{\mathrm{FF}}(\boldsymbol{q}, i\omega_m^{\mathrm{B}}) = \frac{m}{2\pi^2} p_{\mathrm{c}} - \frac{m}{4\pi} \sqrt{m\Big(\frac{q^2}{4m} - \mu_{\mathrm{F}} - i\omega_m^{\mathrm{B}}\Big)}. \tag{C.5}$$

Using $E_{\mathrm{bind}} = 1/(m a_{\mathrm{FF}}^2)$ as the binding energy of Fermi-Fermi bound molecule and taking,

$$\mu_{\mathrm{CB}} = \mu_{\mathrm{F}} + E_{\mathrm{bind}}, \tag{C.6}$$

we can rewrite the bosonic particle-particle scattering matrix $\Gamma_{\mathrm{FF}}(\boldsymbol{q}, i\omega_m^{\mathrm{B}})$ into the form,

$$\Gamma_{\mathrm{FF}}(\boldsymbol{q}, i\omega_m^{\mathrm{B}}) = \frac{8\pi}{m^2 a_{\mathrm{FF}}} \frac{1}{i\omega_m^{\mathrm{B}} - \xi_{\boldsymbol{q}}^{\mathrm{CB}}}, \tag{C.7}$$

where the relation $E_{\mathrm{bind}} \gg [q^2/(2M) - \mu_{\mathrm{CB}} - i\omega_m^{\mathrm{B}}]$ has been used to obtain the result.

In Eq. (C.7), ones sees that the particle-particle scattering matrix $\Gamma_{\mathrm{FF}}(\boldsymbol{q}, i\omega_m^{\mathrm{B}})$ in a Fermi-Fermi case takes the form of a molecular Bose Green's function with molecular mass $M = 2m$ and $\xi_{\boldsymbol{q}}^{\mathrm{CB}} = q^2/(2M) - \mu_{\mathrm{CB}}$, where μ_{CB} in Eq. (C.6) works as the molecular Bose chemical potential.

Appendix D

Treatment of Singularity in $\tilde{\Sigma}_{\mathrm{F}}(\boldsymbol{p}, i\omega_n^{\mathrm{F}})$ at T_{BEC} using Cubic Spline Interpolation

In this appendix, we discuss the method for removal of singularity existing in Fermi self-energy $\tilde{\Sigma}_{\mathrm{F}}$ in our improved TMA (iTMA). In iTMA we replace the bare Bose Green's function G_{B}^0 appearing in all the self-energy diagrams by a modified one $\tilde{G}_{\mathrm{B}}^0$ in Eq. (2.64), to satisfy the gapless Bose excitations condition at T_{BEC}. As a result, the fermionic self-energy correction $\tilde{\Sigma}_{\mathrm{F}}(\boldsymbol{p}, i\omega_n^{\mathrm{F}})$ given in Eq. (2.67) has a singular behavior at T_{BEC} due to the presence of $\tilde{G}_{\mathrm{B}}^0(\boldsymbol{q}-\boldsymbol{p}, i\omega_m^{\mathrm{F}} - i\omega_n^{\mathrm{F}})$, which diverges when $(\boldsymbol{q}, i\omega_m^{\mathrm{F}}) = (\boldsymbol{p}, i\omega_n^{\mathrm{F}})$ at T_{BEC}.

In order to avoid this singularity in Eq. (2.67), we opt for change of variables in momentum $\boldsymbol{q} - \boldsymbol{p} = \boldsymbol{k}$,

$$\tilde{\Sigma}_{\mathrm{F}}(\boldsymbol{p}, i\omega_n^{\mathrm{F}}) = -T \sum_{\boldsymbol{k}, \omega_m^{\mathrm{F}}} \tilde{\Gamma}_{\mathrm{BF}}(\boldsymbol{k}+\boldsymbol{p}, i\omega_m^{\mathrm{F}}) \tilde{G}_{\mathrm{B}}^0(\boldsymbol{k}, i\omega_m^{\mathrm{F}} - i\omega_n^{\mathrm{F}}) e^{(i\omega_m^{\mathrm{F}} - i\omega_n^{\mathrm{F}})\delta}. \tag{D.1}$$

Now, the singularity is removed from Eq. (D.1) at a finite momentum, but we need to calculate the particle-particle scattering matrix $\tilde{\Gamma}_{\mathrm{BF}}(\boldsymbol{k}+\boldsymbol{p}, i\omega_m^{\mathrm{F}})$ for given $(\boldsymbol{p}, i\omega_n^{\mathrm{F}})$ in order to evaluate $\tilde{\Sigma}_{\mathrm{F}}(\boldsymbol{p}, i\omega_n^{\mathrm{F}})$ from Eq. (D.1). This is done using spline interpolation technique, wherein we interpolate the function within a certain range using the discrete known data points of the function in that range. In our case, the function is the particle-particle scattering matrix $\tilde{\Gamma}_{\mathrm{BF}}(\boldsymbol{k}+\boldsymbol{p}, i\omega_m^{\mathrm{F}})$, required to interpolate for all possible values of momentum $\boldsymbol{k}+\boldsymbol{p}$.

Spline is a "piecewise-defined function", and the cubic spline is particularly popular due to easy implementation and only high derivative (third) is discontinuous.

Let us consider a function $y = f(t)$ with $(N+1)$ data points defined as (t_j, y_j) for $j = 0, 1, \cdots, N$. The cubic spline for the interval $[t_j, t_{j+1}]$ is defined as,

$$S_j(t) = A_j(t-t_j)^3 + B_j(t_{j+1}-t)^3 + C_j(t-t_j) + D_j(t_{j+1}-t). \tag{D.2}$$

Since there are N interval in the known data set and four coefficients A_j, B_j, C_j, and D_j per interval, so that a total of $4N$ constraints are required to be solved, in order to determine them. First, we have two conditions defined in the interval $[t_j, t_{j+1}]$ as,

$$\begin{cases} S_j(t_j) = y_j, \\ S_j(t_{j+1}) = y_{j+1}, \end{cases} \tag{D.3}$$

which makes $2N$ conditions. Second, the derivatives

$$\begin{cases} S'_j(t_j) = S'_{j-1}(t_j), \\ S''_j(t_j) = S''_{j-1}(t_j), \end{cases} \tag{D.4}$$

give $2 \times (N-1)$ conditions more, and finally we consider "natural" cubic spline (with fixed end-points), given as

$$\begin{cases} S''_0(t_0) = 0, \\ S''_N(t_N) = 0. \end{cases} \tag{D.5}$$

Thus one can work with $4N$ constraint equations given in Eqs. (D.3), (D.4), and (D.5), to determine $4N$ coefficients of cubic spline in Eq. (D.2).

Taking Eq. (D.2) as,

$$S_j(t) = \frac{z_{j+1}}{6h_j}(t-t_j)^3 + \frac{z_j}{6h_j}(t_{j+1}-t)^3 + C_j(t-t_j) + D_j(t_{j+1}-t), \tag{D.6}$$

where, z_j is second derivative of y_j, and one takes z_j, C_j, and D_j such that,

$$\begin{cases} z'_j = 0, \\ C'_j = D'_j = 0. \end{cases} \tag{D.7}$$

After some manipulation (For details, see Ref. [95].), one obtains a set of tridiagonal equations of the form,

$$u_j = z_j v_j + h_{j-i} z_{j-1} + h_j z_{j+1}. \tag{D.8}$$

Solving these tridiagonal equations in (D.8), one evaluates z_j's. Using them, one an easily calculate the interpolating function $S_j(t)$ for any arbitrary t within $[t_0, t_N]$ from Eq. (D.6).

Strictly speaking, the Fermi self-energy $\tilde{\Sigma}_{\rm F}(\boldsymbol{p}, i\omega_n^{\rm F})$ in Eq. (D.1) is calculated as,

$$\begin{aligned} \tilde{\Sigma}_{\rm F}(\boldsymbol{p}, i\omega_n^{\rm F}) = & -T \sum_{\boldsymbol{k},\omega_m^{\rm F}} \left[\tilde{\Gamma}_{\rm BF}(\boldsymbol{k}+\boldsymbol{p}, i\omega_m^{\rm F}) + U_{\rm BF}\right] \tilde{G}_{\rm B}^0(\boldsymbol{k}, i\omega_m^{\rm F} - i\omega_n^{\rm F}) e^{(i\omega_m^{\rm F} - i\omega_n^{\rm F})\delta} \\ & + T U_{\rm BF} \sum_{\boldsymbol{k},\omega_m^{\rm F}} \tilde{G}_{\rm B}^0(\boldsymbol{k}, i\omega_m^{\rm F} - i\omega_n^{\rm F}) e^{(i\omega_m^{\rm F} - i\omega_n^{\rm F})\delta} \\ = & -T \sum_{\boldsymbol{k},\omega_m^{\rm F}} \left[\tilde{\Gamma}_{\rm BF}(\boldsymbol{k}+\boldsymbol{p}, i\omega_m^{\rm F}) + U_{\rm BF}\right] \tilde{G}_{\rm B}^0(\boldsymbol{k}, i\omega_m^{\rm F} - i\omega_n^{\rm F}) \\ & - U_{\rm BF} \sum_{\boldsymbol{k}} n_{\rm B}(\tilde{\xi}_{\boldsymbol{p}}^{\rm B}). \end{aligned} \tag{D.9}$$

The leading order in the third line in Eq. (D.9) is $|i\omega_m^{\rm F}|^{-2}$ due to which the convergence factor $e^{(i\omega_m^{\rm F} - i\omega_n^{\rm F})\delta}$ is eliminated.

Appendix E

Calculation of Virial Expansion Coefficients B_{ij} of a Bose-Fermi Mixture

In this appendix, we will derive the virial coefficients B_{ij} in Eq. (4.21). B_{10} and B_{20} are the co-efficients which only depend on Fermi fugacity $z_{\rm F}$ as given in Eq.(4.17). Taking the case of a free Fermi gas [110], one obtains

$$\Omega_{\rm F} = -T\sum_{\boldsymbol{p}}\left[1+e^{-\xi^{\rm F}_{\boldsymbol{p}}/T}\right] = -\frac{TV}{\lambda_T^3}\sum_{n=1}^{\infty}\frac{(-1)^{n+1}}{n^{5/2}}z_{\rm F}^n. \tag{E.1}$$

Now comparing Eq. (E.1) with the free Fermi part of Bose-Fermi thermodynamic potential Ω in Eq. (4.17), one immediately finds

$$B_{i0} = (-1)^{i+1}i^{-5/2}. \tag{E.2}$$

Proceeding similarly, B_{01} and B_{02} are obtained from the virial expansion in the case of a free Bose gas [110],

$$\Omega_{\rm B} = T\sum_{\boldsymbol{p}}\left[1-e^{-\xi^{\rm B}_{\boldsymbol{p}}/T}\right] = -\frac{TV}{\lambda_T^3}\sum_{n=1}^{\infty}\frac{1}{n^{5/2}}z_{\rm B}^n, \tag{E.3}$$

where one obtains

$$B_{0j} = j^{-5/2}. \tag{E.4}$$

To determine B_{11}, it is convenient to substitute the expression for the second-order virial expansion of the grand partition function,

$$\Xi = 1 + Q_{10}z_{\rm F} + Q_{20}z_{\rm F}^2 + Q_{01}z_{\rm B} + Q_{02}z_{\rm B}^2 + Q_{11}z_{\rm F}z_{\rm B}, \tag{E.5}$$

into thermodynamic potential

$$\Omega = -T\ln\Xi, \tag{E.6}$$

which gives

$$B_{11} = \frac{\lambda_T^3}{V}[Q_{11} - Q_{10}Q_{01}]. \tag{E.7}$$

Here,

$$Q_{nn'} = \mathrm{Tr}_{nn'}[e^{-\bar{H}/T}] \tag{E.8}$$

is a canonical partition function with n fermions and n' bosons, where $\bar{H}$ is given by Eq. (2.1) with $\xi^{\mathrm{s}}_{\boldsymbol{p}}$ being replaced by $\varepsilon_{\boldsymbol{p}} = \boldsymbol{p}^2/(2m)$. Equation (E.7) indicates that B_{11} is just the difference of the two-particle canonical partition function between the interacting case (Q_{11}) and the non-interacting case ($Q_{10}Q_{01}$). Now, changing the variables of two particles from the relative one to the center of mass coordinate, and taking into account the contribution from the s-wave scattering component of the latter. We can rewrite Eq. (E.7) as

$$\begin{aligned} B_{11} = \frac{\lambda_T^3}{V} \sum_{\boldsymbol{K}} e^{-\boldsymbol{K}^2/(4mT)} \Biggl[\Biggl[\sum_k e^{-k^2/(mT)} - \sum_q e^{-q^2/(mT)} \Biggr] \\ + e^{\varepsilon_b/T} \theta(a_{\mathrm{BF}}) \Biggr], \end{aligned} \tag{E.9}$$

where $\varepsilon_b = -1/(ma_{\mathrm{BF}}^2) < 0$ is the s-wave bound state energy which exists only when $a_{\mathrm{BF}}^{-1} \geq 0$. Eq. (E.9) can again be written as,

$$B_{11} = 2^{3/2} \left[\int_0^\infty dp \, [\rho(p) - \rho_0(p)] \, e^{-p^2/(mT)} + e^{\varepsilon_b/T} \theta(a_{\mathrm{BF}}) \right], \tag{E.10}$$

where $\rho(p)$ and $\rho_0(p)$ are the momentum-space density of states in the interacting and non-interacting case, respectively. Since the wave-function in the interacting case behaves as,

$$\Psi(r) \sim \frac{1}{r} \sin(pr + \delta_s(p)), \tag{E.11}$$

(where δ_s is the phase shift associated with the inter-species interaction in Eq. (2.1)), the interval Δp of the quantum states in momentum space is given by

$$\Delta p = \frac{\pi}{R + \dfrac{\partial \delta_s(p)}{\partial p}}, \tag{E.12}$$

as a result of the wave-function boundary condition (where, R is the system size). The density of states $\rho(p)$ is then obtained as $\rho(p) = \Delta p^{-1}$. The density of states $\rho_0(p)$ in the non-interacting case is also obtained from $\Delta p^{(0)^{-1}}$ such that,

$$\Delta p^{(0)} = \frac{\pi}{R}. \tag{E.13}$$

Substituting Eqs. (E.12) and (E.13) into Eq. (E.10), one has [110]

$$B_{11} = 2^{3/2} \left[\frac{1}{\pi} \int_0^\infty dp \frac{\partial \delta_s(p)}{\partial p} e^{-p^2/(mT)} + e^{\varepsilon_b/T} \theta(a_{\mathrm{BF}}) \right]. \tag{E.14}$$

Noting the relation $\tan(\delta_s(p)) = -pa_{\mathrm{BF}}$ between the phase shift $\delta_s(p)$ and the scattering length a_{BF} in Eq. (4.1), we can further rewrite Eq. (E.14) as

$$B_{11} = 2^{3/2} \left[\frac{1}{\pi} \int_0^\infty dp \frac{-a_{\mathrm{BF}}}{1 + (pa_{\mathrm{BF}})^2} e^{-p^2/(mT)} + e^{\varepsilon_b/T} \theta(a_{\mathrm{BF}}) \right]. \tag{E.15}$$

Taking the limit from the weak coupling side in Eq. (E.15), we obtain B_{11} for any arbitrary interaction strength $a_{\rm BF}^{-1}$ as

$$\begin{aligned} B_{11} = 2^{3/2} \Bigg[& \frac{-\mathrm{sgn}(a_{\rm BF})}{\pi} \int_0^\infty dx \frac{1}{1+x^2} e^{-x^2/(mT|a_{\rm BF}|^2)} \\ & + e^{\varepsilon_b/T}\theta(a_{\rm BF}) \Bigg] \\ = 2^{3/2} & \left[\frac{-\mathrm{sgn}(a_{\rm BF})}{2} [1-\mathrm{erf}(y)] e^{y^2} + e^{\varepsilon_b/T}\theta(a_{\rm BF}) \right]. \end{aligned} \tag{E.16}$$

Here, $\mathrm{erf}(y)$ is the error function and $y = 1/\sqrt{(mT|a_{\rm BF}|^2)}$. Taking the unitarity limit ($a_{\rm BF}^{-1} = \pm 0$) in Eq. (E.16), we obtain B_{11} as

$$B_{11} = 2^{3/2}\left(-\frac{1}{2}+1\right) = \sqrt{2}, \tag{E.17}$$

where we have used $\varepsilon_b = 0$, $\mathrm{erf}(y) = 0$, and $e^{y^2} = 1$, at the unitarity.

Bibliography

[1] A. G. Truscott, K. E. Strecker, W. I. McAlexander, G.B. Partridge, and R. G. Hulet, Science **291**, 2570, (2001).

[2] F. Schreck, I. Khaykovich, K. L. Corwin, G. Ferrari, T. Bourdel, J. Cubizolles, and C. Salomon, Phys. Rev. Lett. **87**, 080403 (2001).

[3] G. Modugno, G. Ferrari, G. Roati, R. J. Brecha, A. Simoni, and M. Inguscio, Science **294**, 1320 (2001).

[4] Z. Hadzibabic, C. A. Stan, K. Dieckmann, S. Gupta, M. W. Zwierlein, A. Görlitz, and W. Ketterle, Phys. Rev. Lett. **88**, 160401 (2002).

[5] G. Roati, F. Riboli, G. Modugno, and M. Inguscio, Phys. Rev. Lett. **89**, 150403 (2002).

[6] G. Modugno, G. Roati, F. Roboli, F. Ferlaino, R. J. Brecha, and M. Inguscio, Science **297**, 2240 (2002).

[7] C. A. Stan, M. W. Zwierlein, C. H. Schunck, S. M. F. Raupach, and W. Ketterle. Phys. Rev. Lett. **93**, 143001 (2004).

[8] S. Inouye, J. Goldwin, M. L. Olsen, C. Ticknor, J. L. Bohn, and D. S. Jin, Phys. Rev. Lett. **93**, 183201 (2004).

[9] F. Ferlaino, C. D'Errico, G. Roati, M. Zaccanti, M. Inguscio, G. Modugno, and A. Simoni, Phys. Rev. A **73**, 040702 (2006), *ibid.*, **74**, 039903 (2006).

[10] M. Zaccanti, C. D'Errico, F. Ferlaino, G. Roati, M. Inguscio, and G. Modugno, Phys. Rev. A **74**, 041605 (2006).

[11] C. Ospelkaus, S. Ospelkaus, L. Humbert, P. Ernst, K. Sengstock, and K. Bongs, Phys. Rev. Lett. **97**, 120402 (2006).

[12] S. Ospelkaus, C. Ospelkaus, L. Humbert, K. Sengstock, and K. Bongs, Phys. Rev. Lett. **97**, 120403 (2006).

[13] B. Deh, C. Marzok, C. Zimmermann, and Ph. W. Courteille, Phys. Rev. A **77**, 010701 (2008).

[14] T. Schuster, R. Scelle, A. Trautmann, S. Knoop, M. K. Oberthaler, M. M. Haverhals, M. R. Goosen, S. J. J. M. F. Kokkelmans, and E. Tiemann, Phys. Rev. A **85**, 042721 (2012).

[15] M. Repp, R. Pires, J. Ulmanis, R. Heck, E. D. Kuhnle, and M. Weidemüller, Phys. Rev. A **87**, 010701 (2013).

[16] C. A. Regal, M. Greiner, and D. S. Jin, Phys. Rev. Lett. **92**, 040403 (2004).

[17] M. W. Zwierlein, C. A. Stan, C. H. Schunck, S. M. F. Raupach, A. J. Kerman, and W. Ketterle, Phys. Rev. Lett. **92**, 120403 (2004).

[18] M. Bartenstein, A. Altmeyer, S. Riedl, S. Jochim, C. Chin, J. H. Denschlag, and R. Grimm, Phys. Rev. Lett. **92**, 203201 (2004).

[19] J. Kinast, S. L. Hemmer, M. E. Gehm, A. Turlapov, and J. E. Thomas, Phys. Rev. Lett. **92**, 150402 (2004).

[20] Q. Chen, J. Stajic, S. Tan, and K. Levin, Phys. Rep. **412**, 1 (2005).

[21] I. Bloch, J. Dalibard, and W. Zwerger, Rev. Mod. Phys. **80**, 885 (2008).

[22] S. Giorgini, L. P. Pitaevskii, and S. Stringari, Rev. Mod. Phys. **80**, 1215 (2008).

[23] C. Chin, R. Grimm, P. Julienne, and E. Tiesinga, Rev. Mod. Phys. **82**, 1225 (2010).

[24] J. Zhang, E.G.M. Van Kempen, T. Bourdel, L. Khaykovich, J. Cubizolles, F. Chevy, M. Teichmann, L. Tarruell, S.J.J.M.F. Kokkelmans, C. Salomon, arXiv:cond-mat/0410167.

[25] C. J. Pethick and H. Smith, *Bose-Einstein Condensation in Dilute Gases*, (Cambridge University Press, New York, 2002).

[26] W. Ketterle and M. W. Zwierlein, in *Proceedings of the International School of Physics "Enrico Fermi", Course CLXIV*, edited by M. Inguscio, W. Ketterle, and C. Salomon (IOP Press, Amsterdam, 2008).

[27] B. DeMarco, and D. S. Jin, Science **285**, 1703 (1999).

[28] M. H. Anderson, J. R. Ensher, M. R. Matthews, C. E. Wieman, and E. A. Cornell, Science **269**, 198 (1995).

[29] C. C. Bradley, C. A. Sackett, J. J. Tollett, and R. G. Hulet, Phys. Rev. Lett. **75**, 1687 (1995).

[30] K. B. Davis, M.-O. Mewes, M. R. Andrews, N. J. van Druten, D. S. Durfee, D. M. Kurn, and W. Ketterle, Phys. Rev. Lett. **75**, 3969, (1995).

[31] K. Mϕlmer, Phys. Rev. Lett. **80**, 1804 (1998).

[32] T. Miyakawa, T. Suzuki, H. Yabu, Phys. Rev. A **64**, 033611 (2001).

[33] R. Roth, Phys. Rev. A **66**, 013614 (2002).

[34] M. Modugno, F. Ferlaino, F. Roboli, G. Roati, G. Modugno, and M. Ingscio, Phys. Rev. A **68**, 043626 (2003).

[35] M. J. Bijlsma, B. A. Heringa, and H. T. C. Stoof, Phys. Rev. A **61**, 053601 (2000).

[36] H. Heiselberg, C. J. Pethick, H. Smith, and L. Viverit, Phys. Rev. Lett. **85**, 2418 (2000).

[37] H. Yabu, Y. Takayama, and T. Suzuki, Physica B **329-333**, 25 (2003).

[38] H. Yabu, Y. Takayama, T. Suzuki, and P. Schuck, Nuc. Phys. A **738**, 273 (2004).

[39] I. Ferrier-Barbut, M. Delehaye, S. Laurent, A. T. Grier, M. Pierce, B. S. Rem, F. Chevy, and S. Salomon, Science **345**, 1035 (2014).

[40] M. Delehaye, S. Laurent, I. Ferrier-Barbut, S. Jin, F. Chevy, and C. Salomon, Phys. Rev. Lett. **115**, 265303 (2015).

[41] T. Ikemachi, A. Ito, Y. Aratake, Y. Chen, M. Koashi, M. Kuwata-Gonokami, M. Horikoshi, arXiv:cond-mat/1606.09404.

[42] A. Storozhenko, P. Schuck, T. Suzuki, H. Yabu, and J. Dukelsky, Phys. Rev. A **71**, 063617 (2005).

[43] T. Watanabe, T. Suzuki, and P. Schuck, Phys. Rev. A **78**, 033601 (2008).

[44] E. Fratini and P. Pieri, Phys. Rev. A **81**, 051605(R) (2010).

[45] E. Fratini and P. Pieri, Phys. Rev. A **85**, 063618 (2012).

[46] E. Fratini and P. Pieri, Phys. Rev. A **88**, 013627 (2013).

[47] T. Loftus, C. A. Regal, C. Ticknor, J. L. Bohn, and D. S. Jin, Phys. Rev. Lett. **88**, 173201 (2002).

[48] D. M. Eagles, Phys. Rev. **186**, 456 (1969).

[49] P. Nozières, and S. Schmitt-Rink, J. Low Temp. Phys. **59**, 195 (1985).

[50] C. A. R. Sá de Melo, M. Randeria, and J. R. Engelbrecht, Phys. Rev. Lett. **71**, 3202 (1993).

[51] J. R. Engelbrecht, M. Randeria, and C. A. R. Sá de Melo, Phys. Rev. B **55**, 15153 (1997).

[52] P. Pieri and G. C. Strinati, Phys. Rev. B **61**, 15370 (2000).

[53] Y. Ohashi, and A. Griffin, Phys. Rev. Lett. **89**, 130402, (2002).

[54] A. Perali, P. Pieri, G.C. Strinati, and C. Castellani, Phys. Rev. B **66**, 024510 (2002).

[55] A. J. Leggett, in *Modern Trends in the Theory of Condensed Matter* edited by Pekalski and Przystawa (Springer, Berlin, 1980).

[56] M. Randeria, in *Bose-Einstein Condensation*, edited by A. Griffin, D. W. Snoke, and S. Stringari (Cambridge University Press, New York, 1995), p.355.

[57] J. R. Schrieffer, *Theory of Superconductivity* (Westview Press, Colorado, 1999).

[58] S. Tsuchiya, R. Watanabe, and Y. Ohashi, Phys. Rev. A **80**, 033613 (2009).

[59] S. Tsuchiya, R. Watanabe, and Y. Ohashi, Phys. Rev. A **82**, 033629 (2010).

[60] R. Watanabe, S. Tsuchiya, and Y. Ohashi, Phys. Rev. A **82**, 043630 (2010).

[61] H. Hu, X.-J. Liu, P. D. Drummond, and H. Dong, Phys. Rev. Lett. **104**, 240407 (2010).

[62] C.-C. Chien, H. Guo, Y. He, and K. Levin, Phys. Rev. A **81**, 023622 (2010).

[63] A. Perali, F. Palestini, P. Pieri, G. C. Strinati, J. T. Stewart, J. P. Gaebler, T. E. Drake, and D. S. Jin, Phys. Rev. Lett. **106**, 060402 (2011).

[64] Q. Chen, and J. Wang, Front. Phys. **9**, 539 (2014).

[65] M. Ota, H. Tajima, R. Hanai, D. Inotani, and Yoji Ohashi, arXiv:1703.01197.

[66] S. Tsuchiya, R. Watanabe, and Y. Ohashi, Phys. Rev. A **84**, 043647 (2011).

[67] J. T. Stewart, J. P. Gaebler, and D. S. Jin, Nature **454**, 744 (2008).

[68] J. P. Gaebler, J. T. Stewart, T. E. Drake, D. S. Jin, A. Perali, P. Pieri, and G. C. Strinati, Nature Phys. **6**, 569 (2010).

[69] Y. Sagi, T. E. Drake, R. Paudel, R. Chapurin, and D. S. Jin, Phys. Rev. Lett. **114**, 075301 (2015).

[70] Ch. Renner, B. Revaz, J.-Y. Genoud, K Kadowaki, and Ø. Fisher, Phys. Rev. Lett. **80**, 149 (1998).

[71] P. A. Lee, N. Nagaosa, and X.-G. Wen, Rev. Mod. Phys. **78**, 17 (2006).

[72] Ø. Fisher, M. Kugler, I. Maggio-Aprile, and C. Berthod, Rev. Mod. Phys. **79**, 353 (2007).

[73] S. Nascimbène, N. Navon, K. J. Jiang, F. Chevy and C. Salomon, Nature **463**, 1057 (2010).

[74] M. Horikoshi, S. Nakajima, M. Ueda,and T. Mukaiyama, Science **327**, 442 (2010).

[75] C. Sanner, E. J. Su, A. Keshet, W. Huang, J. Gillen, R. Gommers, and W. Ketterle, Phys. Rev. Lett. **106**, 010402 (2011).

[76] A. Sommer, M. Ku, G. Roati, and M. W. Zwierlein, Nature (London) **472**, 201 (2011).

[77] J. Meineke, J.-P. Brantut, D. Stadler,T. Müller, H. Moritz, and T. Esslinger, Nat. Phys. **8**, 454 (2012).

[78] M. J. H. Ku, A. T. Sommer, L. W. Cheuk, and M. W. Zwierlein, Science **335**, 563 (2012).

[79] Y.-R. Lee, T. T. Wang, T. M. Rvachov, J.-H. Choi, W. Ketterle, M.-S. Heo, Phys. Rev. A **87**, 043629 (2013).

[80] M. Horikoshi, M. Koashi, H. Tajima, Y. Ohashi, and M. Kuwata-Gonokami, arXiv:1612.04026.

[81] T.-L. Ho, Phys. Rev. Lett. **92**, 090402 (2004).

[82] H. Tajima, P. van Wyk, R. Hanai, D. Kagamihara, D. Inotani, M. Horikoshi, and Y. Ohashi, Phys. Rev. A **95**, 043625 (2017).

[83] S. Tan, Ann. Phys. **323**, 2952 (2008).

[84] S. Tan, Ann. Phys. **323**, 2971 (2008).

[85] S. Tan, Ann. Phys. **323**, 2987 (2008).

[86] D. Kharga, D. Inotani, R. Hanai, and Y. Ohashi, J. Low Temp. Phys. **187**, 661 (2017).

[87] A. L. Fetter and J. D. Walecka, *Quantum Theory of Many-Particle Systems*, (Dover Publications, New York, 2003).

[88] G. Rickayzen, *Green's Functions and Condensed Matter* (Academic Press, London, 1980).

[89] A. A. Abrikosov, L. P. Gorkov, and I. E. Dzyaloshiski, *Methods of Quantum Field Theory in Statistical Mechanics* (Dover, New York 1963).

[90] G. D. Mahan, *Many Particle Physics*, (Kluwer Academic, Plenum Publishers, New York, 2000).

[91] N. M. Hugenholtz and D. Pines, Phys. Rev. **116**, 489 (1959).

[92] D. J. Thouless, Ann. Phys. **10**, 553 (1960).

[93] The number $N_{\rm F}^{\rm unpair}$ of unpaired Fermi atoms is evaluated from $N_{\rm F}^{\rm unpair} = \sum_{\boldsymbol{p}} n_{\rm F}(\varepsilon_{\boldsymbol{p}} - \mu_{\rm F})$ using the Fermi chemical potential $\mu_{\rm F} = 0.62\varepsilon_{\rm F}$ at the critical interaction strength ($(k_{\rm F}a_{\rm BF})^{-1} = 1.62$) at $T = 0.01T_{\rm F}$.

[94] D. Kharga, D. Inotani, R. Hanai, and Y. Ohashi, arXiv:cond-mat/1705.02591.

[95] W. H. Press, S. A. Teukolsky, W. T. Vetterling and B. P. Flannery, *Numerical Recipes in Fortran 77: The Art of Scientifif Computing*, (Cambridge University Press, 1992) Chap. 3.

[96] G. A. Baker, Jr. and P. G.-Morris, *Padé Approximants*, (Cambridge University Press, New York, 1996) Chap. 1.

[97] Strictly speaking, Fermi atomic, Bose atomic, and Fermi molecular excitations are all coupled to one another, and the coupled dispersions are determined from poles of the Green's functions $G^{\rm R}_{\rm s=B,F}(\boldsymbol{p},\omega)$ in Eqs. (3.15) and (3.16). However, in order to simply show the Fermi molecular contribution, we draw $\omega = \xi^{\rm CF}_{\boldsymbol{p}}$ in Fig. 3.3(a6) and (b6), for eye-guide.

[98] D. Inotani, R. Watanabe, M. Sigrist, and Y. Ohashi, Phys. Rev. A **85**, 053628 (2012).

[99] T. Kashimura, R. Watanabe, and Y. Ohashi, Phys. Rev. A **86**, 043622 (2012).

[100] R. Hanai, T. Kashimura, R. Watanabe, D. Inotani, and Y. Ohashi, Phys. Rev. A **88**, 053621 (2013).

[101] R. Hanai, and Y. Ohashi, Phys. Rev. A **90**, 043622 (2014).

[102] E. Beth, and G. E. Uhlenbeck, Physica **IV**, 915 1937.

[103] R. Dashen, S.-K. Ma, and H. J. Bernstein, Phys. Rev. **187**, 345 (1969).

[104] L. S. Brown, and L. G. Yaffe, Phys. Rep. **340**, 1 (2001).

[105] T.-L. Ho, and E. J. Mueller, Phys. Rev. Lett. **92**, 160404 (2004).

[106] X.-J. Liu, H. Hu, and P. D. Drummond, Phys. Rev. Lett. **102**, 160401 (2009).

[107] D. B. Kaplan, and S. Sun, Phys. Rev. Lett. **107**, 030601 (2011).

[108] X.-J. Liu, Phys. Rep. **524**, 37 (2013).

[109] V. Ngampruetikorn, M. M. Parish, and J. Levinsen, Phys. Rev. A **91**, 013606 (2015).

[110] K. Huang, *Statistical Mechanics* (John Wiley & Sons, Canada, 1987).

[111] G. A. Baker, Jr., Phys. Rev. C **60**, 054311 (1999).

[112] T. -L. Ho, and Q. Zhou, Nat. Phys. **6**, 131 (2010).